Metastable Light-Induced Superconductivity in K_3C_{60}

Dissertation

zur Erlangung des Doktorgrades

an der Fakultät für Mathematik, Informatik und Naturwissenschaften

Fachbereich Physik

der Universität Hamburg

vorgelegt von

Matthias Johannes Budden

Hamburg

2020

Gutachter der Dissertation:

Prof. Dr. Andrea Cavalleri
Prof. Dr. Henning Moritz

Zusammensetzung der Prüfungskommission:

Prof. Dr. Andrea Cavalleri
Prof. Dr. Henning Moritz
Prof. Dr. Ludwig Mathey
PD Dr. Guido Meier
Prof. Dr. Michael Rübhausen

Vorsitzender der Prüfungskommission:

Prof. Dr. Michael Rübhausen

Datum der Disputation:

08.12.2020

Vorsitzender Fach-Promotionsausschuss PHYSIK:

Prof. Dr. Günter H. W. Sigl

Leiter des Fachbereichs PHYSIK:

Prof. Dr. Wolfgang Hansen

Dekan der Fakultät MIN:

Prof. Dr. Heinrich Graener

EIDESSTATTLICHE VERSICHERUNG

Hiermit versichere ich an Eides statt, die vorliegende Dissertationsschrift selbst verfasst und keine anderen als die angegebenen Hilfsmittel und Quellen benutzt zu haben. Die eingereichte schriftliche Fassung entspricht der auf dem elektronischen Speichermedium. Die Dissertation wurde in der vorgelegten oder einer ähnlichen Form nicht schon einmal in einem früheren Promotionsverfahren angenommen oder als ungenügend beurteilt.

Hamburg, 24. September 2020

_____

M. Budden

Translation

I hereby affirm in lieu of oath that I have written the present dissertation myself and have not used any aids or sources other than those indicated. The submitted written version corresponds to the version on the electronic storage medium. The dissertation in the submitted or a similar form has not been accepted before in a previous doctoral procedure or assessed as insufficient.

Abstract

The on-demand control of material properties is of fundamental importance for both scientific and technological applications. Quantum materials are particularly relevant in this context, since mutual interactions between their numerous degrees of freedom makes their properties extremely sensitive to external perturbations. Slight parameter changes can tip the equilibrium between these different degrees of freedom and lead to phase transitions accompanied by dramatic modifications of physical characteristics.
Short and intense pulses of light provide a means of ultrafast, contactless manipulation including the capability of phase switching in a material. Such optical excitation in complex materials has proven to be a powerful tool for coherent and selective control of specific degrees of freedom. In view of the typical energy scales of collective phenomena in solids, laser pulses with terahertz and mid-infrared frequencies are particularly useful. Advances in laser technology have enabled extremely intense light fields in this frequency range that can drive a system into highly nonlinear regimes while dissipation is reduced by the direct low energy excitation. This has been shown to induce non-equilibrium order, including photo-induced ferroelectricity, magnetic polarization in antiferromagnets, and transient superconductivity in the normal state of cuprates and organic conductors. In particular, driving local vibrations in the alkali doped fulleride K_3C_{60} induced a state with superconducting-like optical properties up to at least 100 K, which corresponds to five times the equilibrium critical temperature. Generally, photo-induced non-equilibrium superconducting properties that were realized by femtosecond drives, decayed within a few picoseconds after excitation, evidencing states that lack intrinsic rigidity.
Aiming at a stabilization of this transient response on a longer timescale, we developed a new optical device based on a combination of a seeded gas laser with semiconductor optical switches that is capable of producing high intensity mid-infrared pump pulses with tunable duration from about one picosecond to one nanosecond.
The same superconducting-like optical properties observed over short time windows for femtosecond excitation are shown here to become metastable under sustained optical driving, with lifetimes in excess of ten nanoseconds. Direct electrical probing, which becomes possible at these timescales, yields a vanishingly small resistance with the same relaxation time as that estimated by terahertz conductivity. Such substantial positive photoconductivity is highly unusual for a metal and in combination with the transient optical conductivities, it is suggestive of metastable out-of-equilibrium superconductivity.
Our experimental results represent a benchmark for current theories on light-

induced superconductivity and allow an assessment of the most promising approaches in literature. Furthermore, we provide a phenomenological description of the dynamics after excitation. This justifies the observed slow relaxation by considering randomization of the order-parameter phase as the rate-limiting process that determines the decay of the light-induced superconductor.
By pushing the lifetime from the terahertz far into the gigahertz range, we thus leverage ultrafast experiments to provide a more profound understanding of the physics at hand. Beyond that, the discovery of a metastable light-induced state with clear signatures of superconductivity holds significant promise for future investigations. It paves the way for pressing experiments on a photo-induced Meissner effect and inspires thoughts about applications in integrated devices based on state-of-the-art high-speed electronics.

Zusammenfassung

Die Kontrolle von Materialeigenschaften "auf Knopfdruck" ist sowohl aus wissenschaftlicher Sicht als auch für technologische Anwendungen von gleichermaßen grundlegender Bedeutung. Quantenmaterialien sind in diesem Kontext ganz besonders relevant, da die gegenseitige Wechselwirkung zwischen zahlreichen Freiheitsgraden ihre Eigenschaften extrem empfindlich gegenüber äußeren Störungen macht. Schon geringste Parameteränderungen können das Gleichgewicht zwischen diesen verschiedenen Freiheitsgraden zum Kippen bringen und zu Phasenübergängen führen, die mit dramatischen Veränderungen der physikalischen Eigenschaften einhergehen.
Kurze und intensive Lichtpulse ermöglichen die ultraschnelle, kontaktlose Manipulation eines Materials einschließlich der Einleitung eines Phasenübergangs. Eine solche optische Anregung hat sich in komplexen Materialien als ein leistungsfähiges Werkzeug zur kohärenten und selektiven Steuerung bestimmter Freiheitsgrade erwiesen. Im Hinblick auf die typischen Energieskalen kollektiver Phänomene in Festkörpern sind Laserpulse mit Terahertz- und Mittelinfrarot-Frequenzen besonders nützlich. Lasertechnologische Fortschritte ermöglichten zudem extrem intensive Lichtfelder in diesem Frequenzbereich, die ein System in hochgradig nichtlineare Bereiche treiben können, wobei gleichzeitig die thermische Dissipation aufgrund der direkten, niederenergetischen Anregung reduziert wird. Experimentell können mit diesem Ansatz vielfältige Nicht-Gleichgewichtsordnungen erzeugt werden. Dazu gehören die photoinduzierte Ferroelektrizität, magnetisch polarisierte Zustände in Antiferromagneten sowie transiente, supraleitende Zustände im Normalzustand von Kupraten und organischen Leitern. Insbesondere induzierte die Anregung lokaler Schwingungen in dem alkali-dotierten Fullerid K_3C_{60} einen Zustand mit den optischen Eigenschaften eines Supraleiters bis mindestens 100 K, was dem Fünffachen der kritischen Gleichgewichtstemperatur entspricht. Im Allgemeinen zerfallen diese mittels Femtosekundenlaserpulsen erzeugten supraleitenden Nichtgleichgewichtszustände innerhalb weniger Pikosekunden nach der Anregung, was auf Zustände hindeutet, denen es an intrinsischer Stabilität mangelt.
Mit dem Ziel, diese transienten Zustände auf einer längeren Zeitskala zu stabilisieren, haben wir eine neue Laserquelle entwickelt, die auf einer Kombination eines geseedeten Gaslasers mit optischen Halbleiterschaltern basiert. Sie ist in der Lage hochintensive Lichtpulse im mittleren Infrarot mit einstellbarer Pulslänge von etwa einer Pikosekunde bis zu einer Nanosekunde zu erzeugen.

In dieser Arbeit zeigen wir, dass dieselben, supraleitertypischen optischen Eigenschaften, die auf kurzen Zeitskalen nach Femtosekunden-Anregungen beobachtet werden, unter anhaltender optischer Stimulation metastabil werden und Lebensdauern von mehr als zehn Nanosekunden ausbilden. Diese langen Zeitskalen ermöglichten erstmals direkte elektrische Transportmessungen, die auf einen verschwindend kleinen Widerstand der angeregten Probe hindeuten, der die gleichen Relaxationszeit aufweist, die mittels Terahertz-Leitfähigkeit bestimmt wurde. Eine solch substantielle positive Photoleitfähigkeit ist für ein Metall höchst ungewöhnlich und deutet in Kombination mit der transienten optischen Leitfähigkeit auf einen metastabilen lichtinduzierten supraleitenden Zustand hin.
Unsere experimentellen Ergebnisse bieten Vergleichswerte für aktuelle Theorien zur lichtinduzierten Supraleitung und ermöglichen eine Bewertung der vielversprechendsten Ansätze in der Literatur. Darüber hinaus liefern wir eine phänomenologische Beschreibung der Dynamik nach der Anregung. Diese betrachtet die Randomisierung des Phasen-Ordnungsparameters als ratenbegrenzenden Prozess für den Zerfall des supraleitenden Zustands und erklärt auf diese Weise die beobachtete langsame Relaxation. Indem wir die Lebensdauer aus dem Terahertz-Bereich weit in den Gigahertz-Bereich verschieben, erhalten wir mit den ultraschnellen Experimenten ein tieferes Verständnis der zugrunde liegenden Physik. Darüber hinaus birgt die Entdeckung eines metastabilen lichtinduzierten Zustandes mit klaren Signaturen von Supraleitung vielversprechendes Potenzial für zukünftige Untersuchungen. Sie ebnet den Weg für dringliche Experimente zu einem photoinduzierten Meissner-Effekt und inspiriert Gedanken zu Anwendungen in integrierten Schaltkreisen, die auf moderner Hochgeschwindigkeitselektronik basieren.

Contents

Eidesstattliche Versicherung / Declaration on Oath III

Abstract V

Zusammenfassung VII

1 Controlling Complex Materials with Light 1
- 1.1 Emergent Phenomena in Strongly Correlated Solids 5
- 1.2 Light Control of Superconductivity 9

2 The Organic Superconductor K_3C_{60} 15
- 2.1 Crystal Structure and Phase Diagram 15
- 2.2 Phonons and Molecular Vibrations 17
- 2.3 Electronic Properties 19
- 2.4 Strongly Correlated Superconductivity in K_3C_{60} 21
  - 2.4.1 Properties of the Superconducting State in K_3C_{60} . . . 21
  - 2.4.2 Mechanisms for Pairing 24

3 Light Induced Superconductivity in K_3C_{60} 29
- 3.1 Equilibrium Optical Properties 29
- 3.2 Excitation with Mid-Infrared Light 33
  - 3.2.1 Dependence on Pump Wavelength and Fluence 36
  - 3.2.2 Dependence on Temperature 37
  - 3.2.3 Dependence on Hydrostatic Pressure 37
- 3.3 Summary 40

4 Generation of High Power, Tunable, Mid-Infrared Light Pulses 43
- 4.1 Light Sources in the Mid-Infrared 43
- 4.2 Stabilization and Synchronization of CO_2 Gas Lasers 47
- 4.3 Generation of Ultrafast Pulses from Gas Lasers 51
  - 4.3.1 Pressure Broadening 51
  - 4.3.2 Field Broadening 52
  - 4.3.3 Optical Free Induction Decay 52
  - 4.3.4 Semiconductor Switching 53
- 4.4 Overview of the Experimental Setup 60

5 Extending the Lifetime of the Superconducting State 63
- 5.1 Excitation with Higher Fluence 63

5.1.1 Transient Optical Properties . . . 64
5.1.2 Temperature Dependence . . . 66
5.2 Excitation with Tunable Pulse Length . . . 68
5.2.1 Transient Optical Properties . . . 68
5.2.2 Relaxation Dynamics . . . 68
5.2.3 Pulse Length Dependence . . . 70
5.3 Electronic Transport on K_3C_{60} . . . 71
5.3.1 Equilibrium Four-Probe Transport Measurements . . . 72
5.3.2 Transient Time Resolved Transport Measurements . . . 73
5.3.3 Pulse Length and Fluence Dependence . . . 76
5.3.4 Temperature dependence . . . 78
5.4 Summary . . . 80

6 Mechanisms for Light-Induced Superconductivity in K_3C_{60} 83
6.1 Microscopic models . . . 83
6.1.1 Response via phonon-phonon coupling . . . 84
6.1.2 Response via phonon-electron coupling . . . 87
6.1.3 Pure electronic response . . . 90
6.2 Phenomenological models . . . 93

7 Conclusions and Outlook 97

Appendices 101

A K_3C_{60} sample growth and characterization 103

B Optical techniques 107
B.1 Hybrid solid-state gas laser pump-probe setup . . . 107
B.2 Generation of mid-infrared pulses by optical parametric amplification . . . 110
B.3 Time resolved THz pump-probe spectroscopy . . . 111
B.3.1 Generation of THz probe-pulses . . . 112
B.3.2 Detection of THz radiation by electro-optic sampling . 113
B.3.3 THz beam characterization . . . 115

C Data aquisition 121
C.1 Lock-in amplifier vs. DAQ-Card . . . 121
C.2 PulseSearchPlus data acquisition and analysis software . . . 125

D Data analysis for time resolved THz spectroscopy 129
D.1 Determination of the out-of-equilibrium optical response . . . 129
D.2 Drude-Lorentz fits of the out-of-equilibrium optical response . 130
D.3 Influence of uncertainties in the equilibrium optical properties 132

E Time-resolved electrical transport measurements 135

E.1 Sample preparation 135
E.2 Calibration of two-terminal measurements 136
E.3 Modeling time-resolved electrical transport measurements . . 139

F Simulations of the superconducting order parameter relaxation 143

Frequently Used Acronyms 149

List of Publications 153

Acknowledgement 155

Bibliography 161

1 Controlling Complex Materials with Light

Active manipulation of materials properties has always been of great interest, both for a variety of technological applications and for research on fundamental processes such as phase transitions. Many scientific breakthroughs followed by technological advances such as the transistor, the laser, the solar cell and the hard-disk-drive are making use of well known base materials that were pushed into a regime of novel physical phenomena by changing external parameters.

Variables such as temperature, pressure, magnetic field or the degree of doping by another compound can be used to influence thermal fluctuations, lattice spacing, spin order and band filling, respectively. Tuning those parameters is a common approach to induce phase transitions within a material, which in turn supports the formation of new ground states with distinctly changed physical properties.

Examples of familiar phase transitions are temperature or pressure induced melting of ice into water, as well as the transition from a para- to a ferromagnetic phase upon cooling or application of an external magnetic field. Regardless of the exact nature of a phase transition, formation or loss of order in a material is one of its universal characteristics. Particularly intriguing are phase transitions that are accompanied by a change in symmetry of the system. Such a spontaneous symmetry breaking is apparent when a system in its ground state has less symmetries than its equations of motion would allow and is always accompanied by a phase transition[1]. When a crystalline structure is melted, the structural order is lost, but the symmetry of the system *increases*. This is because now it does not matter from which direction the system is viewed, it always looks the same and more symmetry operations are compatible with this isotropic state as compared to the crystalline one.[2] Accordingly, the alignment of magnetic moments in a ferromagnet

1 The opposite of this is not necessarily true: not all phase transitions feature spontaneous symmetry breaking. For example, this applies to the liquid-gas phase transition above the critical point.

2 It is important to note, that in the framework of statistical physics we are not talking about a "frozen snapshot" but a time average of the system. Only in this sense the random motions of atoms in a liquid average to an isotropic system with translation and rotation invariance while this is not the case for the slight vibrational movements of atoms in a crystal lattice. The lattice might still be symmetric, but only a subgroup of translations (along the lattice vectors) are allowed, that lead to the same spatial particle distribution.

corresponds to a state with higher order at the expense of its loss of time-reversal symmetry. Typically, the degree of order in a system is quantified by an *order parameter*, which is zero in the disordered phase and one in the perfectly ordered phase.

Self-organized formation of well-ordered patterns is a common phenomenon in nature and typically happens in situations far from equilibrium where small fluctuations and noise can be amplified through feedback loops that stabilize a new order. Examples for this can be found in the flow-induced formation of regular ripples of sand in deserts or shallow tidal waters as well as in the generation of convection cells in a heated pot of water under the influence of gravity. In all cases, a long range order is established due to perturbations of the original state. Lasers represent another nice example for such self-organization. Below the lasing threshold, atoms emit light largely independent of each other, while above the threshold a collective behavior develops in the form of emission of a giant coherent wave [1].
Prerequisite for such interesting dynamics is a system that is in between a static, fully ordered and highly stable equilibrium state, which can be described by simple symmetries, and a state of extreme disorder that is solely modeled by statistics. These so called complex systems feature intrinsic nonlinear behavior and are typically based on local interactions that result in globally emergent properties.

Ultrashort lasers capable of generating sub-picosecond pulses present a novel tool for the dynamic manipulation of matter. These pulses can be used to perturb materials and drive them into new states with properties deviating from equilibrium while measuring at the same time their relaxation rates. Figure 1.1 shows a schematic illustration of the reshaping of a potential energy surface revealing such a hidden state. In reality, potential energy surfaces can be much more complex featuring more than one local minimum separated by potential barriers. These minima correspond to metastable states with lifetimes that depend on the barrier height. It is important to note, that the excitation with light is not only capable to excite the equilibrium system so that already existing metastable states can be reached, but rather new, fundamentally different states can be created. The lifetime of such a photo-induced state is therefore not necessarily limited by the duration of the excitation but rather by the transient response of the excited subsystem.
From the perspective of technological applications, the precise control of phase transitions on ultrashort timescales is important for high speed computing as well as for fast data storage and access. More generally, the ability to switch on a desired materials property at the push of a button

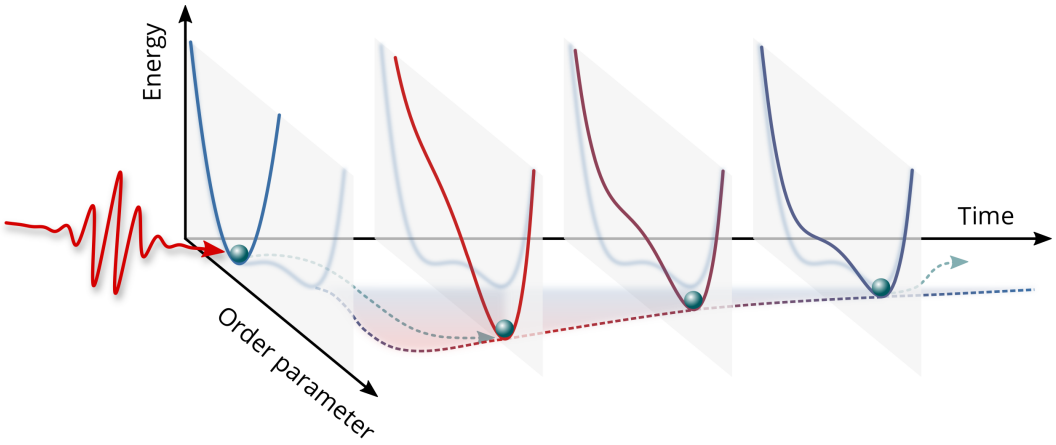

Figure 1.1: Schematic illustration of a photo-induced phase transition.
Upon excitation with a light pulse, a stable ground state (global minimum of the potential energy surface in the first time snapshot) is distorted and a new, previously hidden double-well potential with a different global minimum is formed. Therefore the order parameter of the system changes. Over the course of time, this photo-induced state relaxes back until the original state is energetically favorable and the original lower value of the order parameter is restored.

without changing its chemical composition and to stabilize it for as long as necessary opens up a wide field of applications not only limited to information technology.
This approach gains additional relevance if it is possible to create exotic states such as superconductivity at high temperatures in materials that would normally not exhibit this behavior.

A major advantage of the approach of controlling matter by electromagnetic waves is the ability to tune their energy, phase and polarization state, which makes it a highly selective tool. Figure 1.2 summarizes the fundamental excitations of a solid indicating the wide range of phenomena that can be induced by frequency tuning. While femtosecond pulsed excitation in the visible is commonly used to drive electronic transitions, it is accompanied by significant heating of the electronic subsystem. This is because charges that were excited to higher energy levels normally establish incoherent dynamics and an increase in entropy [3].
In contrast, long range collective behavior, which is of interest in many correlated materials and especially in the context of superconductivity, corresponds to energy scales below 100 meV. To prevent melting of any light-induced state on this energy scale, it is required to mitigate any excess heat introduced by the pump light. Excitation at mid-infrared to terahertz frequencies can directly couple to these low energy modes, while dissipation is reduced compared to higher frequency radiation. This makes it possible to

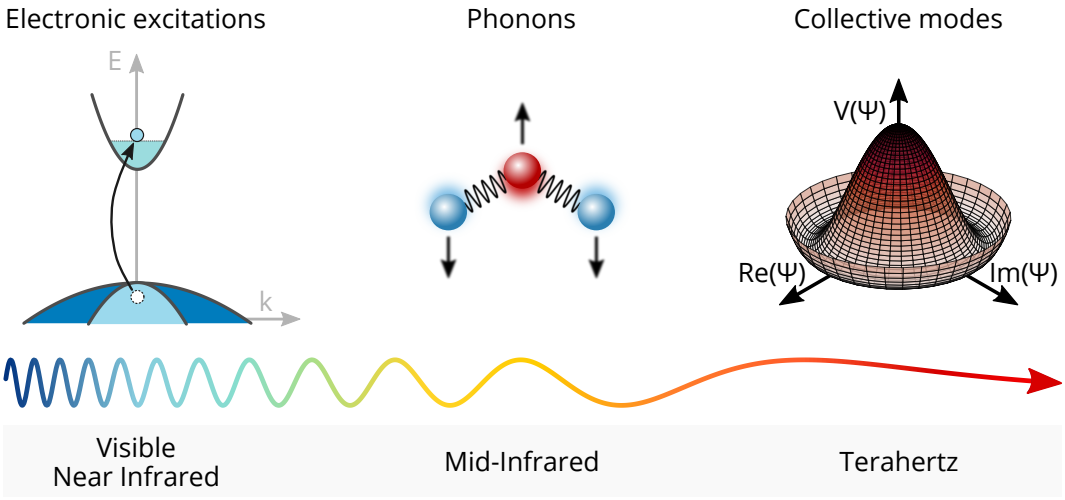

Figure 1.2: Fundamental excitations of solids and their energy scales. Excitation with visible and near infrared radiation (100 – 1000 THz, 0.5 – 4 eV) results in excitation of the electronic system. Examples of this are interband transitions, excitons and high energy surface plasmons. At lower mid-infrared frequencies (10 – 50 THz, 50 – 200 meV) local molecular vibrations and polarons can be excited. Larger collective modes that arise from broken symmetries posses even lower frequencies of ~1 THz. Graphic adapted from [2]

establish an order parameter > 0, that is based on broken symmetries, when applying light at these low energy scales.

This work focuses on how low energy electromagnetic radiation can be used to control collective properties of strongly correlated materials, in particular a long lived superconducting state far above its equilibrium critical temperature in the molecular solid K_3C_{60}. In the remaining part of this first chapter we will introduce strongly correlated solids as ideal model systems for light-induced emergent phenomena before we will focus more specifically on light induced superconductivity.
Chapter 2 presents relevant properties of a particular group of strongly correlated solids, the doped fullerides, with a focus on superconductivity before we will summarize previous experiments on light-induced superconductivity in this compounds in Chapter 3. Based on these findings we will motivate, that a new coherent source of mid-infrared light was needed to extend the life time of the remarkable new state for further investigations. The technological implementation of such an optical device is described in Chapter 4 before experimental results are presented in Chapter 5.
The last chapter of this thesis aims to compare the overall experimental evidence for light-induced superconductivity in the doped fullerides with possible theoretical descriptions based on both microscopic correlations and phenomonological arguments.

1.1 Emergent Phenomena in Strongly Correlated Solids

Many properties of solids can be well described under the assumption of electrons moving independently in an effective potential of periodically arranged positive ionic nuclei. This description leads to the formation of energy bands, which for instance explains the varying conductivity of many metals, insulators and semiconductors [4–6].
In strongly correlated electron systems, that is, in situations where the interactions between two electrons can no longer be described by an average field across the solid, this simplification is no longer applicable. One of the first problems studied in this context in 1949 by Mott was a hypothetical metal-insulator transition that would occur as a function of the lattice spacing [7, 8]: For large separations a single valence electron is bound to a specific atomic site by the respective lattice potential. Since this electron is localized, the material is rendered insulating. In contrast, for smaller ionic separation, the large overlap of the atomic wave functions would allow a delocalized electronic state and thus metallic electrical properties. Already small structural changes could drive this transition.
In practice such systems are realized in the group of transition-metal-oxides, where the electronic and magnetic properties depend on the occupation of d-orbitals and a competition between electron delocalization and onsite Coulomb repulsion [9]. An enhanced Coulomb interaction due to a spatial restriction of electrons has strong implications on all microscopic degrees of freedom. Due to significant interactions of the lattice, charge, spin and orbital systems, strongly correlated materials typically feature a multitude of competing ground states [10]. In these systems, therefore, even small changes in external parameters such as temperature, pressure, magnetic field or doping can lead to strong effects.
Experimentally, not only huge changes in electrical resistance either during a metal to insulator transition [11, 12] or as a result of colossal magnetoresistance (CMR) [13] but also exotic phenomena such as charge density waves (CDW) [14] could be observed. Moreover, abrupt changes of the crystal volume in the rare earth metals are also attributed to strong correlations [15]. One of the most famous phenomenon, however, where the combination of local correlations and long range interactions is known to be of great importance is high temperature superconductivity in the cuprates [16]. Further details on the fascinating physics of correlated materials at equilibrium can be found in [17, 18].

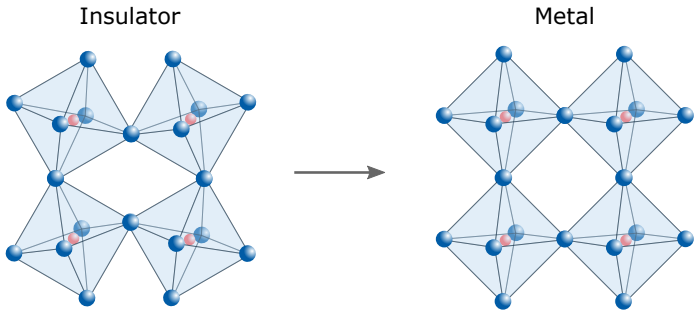

Figure 1.3: Structural change of a rare-earth metal oxide during the insulator-to-metal transition.
Blue and red spheres indicate the oxygen and transition metal ions, respectively. With decreasing structural distortion electronic localization is lowered until a metallic state is reached. Maximum electron hopping is achieved for a bond angle of 180° [27].

The extraordinary sensitivity of quantum materials to external stimuli results in compelling opportunities for material engineering already at equilibrium conditions. These compounds play an important role for the construction of novel sensors, switches and in general for the development of new types of electronic components.
It is therefore a promising approach to drive dynamic and static structural changes or to redistribute charges within the orbitals by optical excitation, with the goal of selectively controlling the balance between competing orders.
Photoinduced control over insulator-to-metal transitions [19–22], as well as over orbital [23] and magnetic order [24] has been demonstrated before. However, as discussed in the last section, low energy excitations provide a much more gentle tool to influence long range cooperative effects as compared to eV-energy photons that would involve significant heating via the scattered hot electron distribution.

The development of new laser sources with transient field strengths of several MV/cm in the mid-infrared (MIR) and terahertz (THz) region of the electromagnetic spectrum made it possible to reach a nonlinear excitation regime with ionic displacements of several percent of the interatomic distances [25]. In 2007 Rini et al. selectively excited a 17 THz phonon mode in a rare-earth manganite ($Pr_{0.7}Ca_{0.3}MnO_3$) and reported a five order of magnitude drop in resistivity [26]. This remarkable change can be associated with a transition from the stable insulating phase to a metastable metallic state that is accompanied by a structural distortion (cf. Fig. 1.3).
Later work on manganites provided evidence of a nonlinear response of the crystal lattice upon resonant excitation [28, 29]. This represented an experimental milestone because until then only two pathways for a cou-

pling between electromagnetic radiation and the crystal lattice were demonstrated:

1. Direct coupling of light to infrared-active vibrations with an electric dipole

2. Indirect coupling of light to the electronic and phononic subsytems (e.g. via impulsive stimulated Raman scattering (ISRS), displacive excitation of coherent phonons (DECP) or in semiconductors via transient depletion field screening (TDFS))

The experiment on manganites mentioned above suggested a third path, ionic Raman scattering, that was postulated already 40 years earlier.

3. Strong *nonlinear* excitation of an infrared active phonon can excite coherent oscillations of the Raman mode and can also rectify the phonon field which results in a static displacement of atoms along the phonon modes.

This anharmonic phonon coupling can explain the observed phase transitions since the nonlinear contributions can transform oscillating atoms on average into net spatial shifts of the crystal structure. Regarding the manganites, femtosecond hard x-ray diffraction experiments revealed that excitation of the infrared active Mn-O stretching mode to high amplitudes results in a nonlinear coupling to the Raman mode coordinate, which is responsible for an effective stationary rotation of the oxygen octahedra (see [30] and Fig. 1.3).

More generally, the lattice dynamics in response to an IR-active phonon can be described by the equation of motion of a damped harmonic oscillator

$$\ddot{Q}_{IR} + 2\gamma\dot{Q}_{IR} + \omega_{IR}^2 Q_{IR} = G(t)\sin(\omega_{IR}t)\,, \tag{1.1}$$

where Q_{IR} is the normal mode coordinate, ω_{IR} its eigenfrequency and γ the damping constant. $G(t)\sin(\omega_{IR}t)$ denotes the pulsed driving field with Gaussian envelope. For high driving field strengths, nonlinear coupling to other modes Q_R sets in and the lowest order lattice Hamiltonian is composed as

$$H = \frac{1}{2}\omega_R^2 Q_R^2 - a_{12}Q_{IR}Q_R^2 - a_{21}Q_{IR}^2 Q_R. \tag{1.2}$$

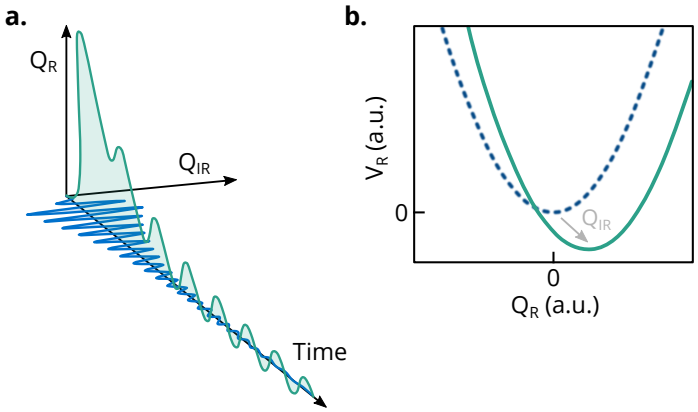

Figure 1.4: Nonlinear phononics.
a. Simulated dynamics of two nonlinearly coupled modes. The light-induced IR-mode oscillates around zero (blue curve) while the anharmonically coupled Raman mode shows a finite displacement that decays over time (green curve). **b.** Harmonic energy potential V_R of the Raman mode. The unperturbed case (dashed curve) is shifted for finite amplitudes of the infrared phonon so that an equilibrium is formed for static displacements of the Raman mode coordinate. Figure adapted from [31].

Here, a_{12} and a_{21} are the nonlinear coupling constants. For centrosymmetric crystals only the second term is relevant if Q_R is a Raman mode[3]. For a finite amplitude of the infrared mode, the potential of the Raman mode is displaced statically and gains a non-zero equilibrium position (cf. Fig. 1.4). The example of the manganites shows that nonlinear phononics more generally can be applied to generate new transient crystal geometries, which are not stable at equilibrium and which in turn can trigger new collective phenomena.

Comprehensive reviews about various forms of nonlinear light matter interactions that were established experimentally can be found in [27, 31] while a microscopic theoretical description of nonlinear phononics and the necessary reconstruction of the electronic structure by dynamical mean-field theory (DMFT) is given in [32]. Furthermore, linear phononics experiments reported the ability to map the interatomic potential of solids [33] and to tune magnetic fields [34, 35].
In the next section we will review important implications for the control of superconductivity.

3 In centrosymmetric crystals any symmetry allowed Hamiltonian needs to be fully symmetric. Since IR-active phonons are of odd and Raman-active of even parity in centrosymmetric crystals, the first coupling term needs to vanish in order to meet this requirement.

1.2 Light Control of Superconductivity

When a small percentage of excess charge is introduced into single-layer cuprates (e.g. by hole-doping La_2CuO_4 with Sr or Ba), high-temperature superconductivity is formed with a T_c in the range of about 30 – 200 K. Prototypical for strongly correlated electron systems the generic phase diagram of the doped cuprates features a multi-faceted composition of different states (see Fig. 1.5). For low hole doping concentrations, a strongly correlated Mott insulator with antiferromagnetic spin disposition is formed. Within a Mott insulator, as mentioned in the previous section, charge carrier transport is only prevented by electron-electron Coulomb repulsion (and not by the Pauli principle as in a band-insulator). This prevents the generation of doubly occupied sites even if the conduction band is half filled and according to band theory would indicate a metallic state. Doping can recover the conductivity through creation of additional sites available for electron transport.
The phase diagram in Fig. 1.5 presents cuprates as unconventional Mott insulators which, at low enough temperatures, by doping change to the superconducting rather than the metallic state. Simultaneously, doping reduces magnetic order until maximum T_c is reached.
For higher temperatures the superconducting state changes to a non-Fermi liquid phase that is characterized by non-negligible electronic interactions. This phase is sometimes called "strange metal" since electronic conduction

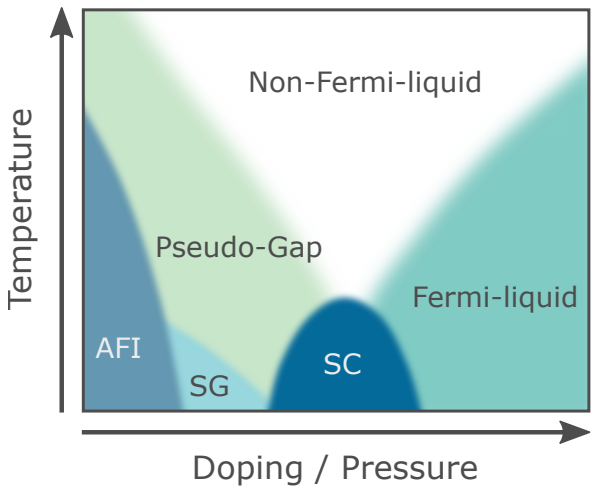

Figure 1.5: Generic phase diagram of a high-T_c superconductor.
Characteristic for strongly correlated electron systems, many competing phase states can be set by changing temperature and doping. Abbreviations: SC = superconductivity, SG = spin glass, AFI = antiferromagnetic insulator. Figure adapted from [18].

can be influenced by phenomena like spin or charge order. Accordingly, the physics of single layer cuprates in this region is determined by a periodic modulation of charge and spin density. This stripe order is suspected to compete with superconductivity leading to a reduction in T_c. The confinement of this order to individual planes of the lattice emphasizes the materials two-dimensional electronic character with weak coupling between different planes.
Various experimental evidence suggests the formation of a pair density wave (PDW), a state where the in plane stripe order modulates the superconducting order parameter so that tunneling between the CuO_2 layers is suppressed. [36, 37]. Recent nonlinear optical THz spectroscopy results support this thesis by suggesting that coherent interlayer transport is reduced once the PDW is formed [38].

Typical energy scales of superconductors are determined by the gap, which controls the Cooper pair binding strength and the phase stiffness, a prerequisite for conduction of supercurrents. In most conventional superconductors, at higher temperatures pairs are broken into quasiparticles until superconductivity is destroyed, since the gap is significantly smaller than the phase stiffness. In contrast, in cuprates the two energy scales are of similar order of magnitude so that an increase in temperature can induce phase fluctuations that weaken phase coherent superconductivity without pair breaking. This was supported by experimental evidence of Uemura et al., suggesting that the critical temperature is not proportional to the size of the gap but rather to the superconducting order parameter stiffness, which is represented by the zero-temperature superfluid density [39].
This finding paves the way towards an enhancement of T_c to values higher than the equilibrium value if it were possible to stiffen the order parameter phase. For example, the charge and spin orders competing with superconductivity can be removed, thus extending the superconducting response to higher temperatures.

It was shown experimentally that nonlinear phononics could be used as a tool to control this competition in Sr-doped La_2CuO_4 [40].
When cooling this high-T_c superconductor at optimal doping ($x = 0.125$) below the critical temperature, a Josephson plasma resonance (JPR) appears in the THz optical properties (see Fig. 1.6 b). This feature is caused by coherent tunneling between the two-dimensional CuO_2-layers and thus signals superconductivity. In contrast, for the stripe ordered compound at lower doping even at low temperatures the optical properties in the same frequency range are flat (cf. Fig. 1.6 c). If, however, the material is driven with infrared light of 15 µm wavelength, which is resonant with an in-plane Cu-O stretching mode, a plasma resonance was found near 60 cm^{-1} similar to what was

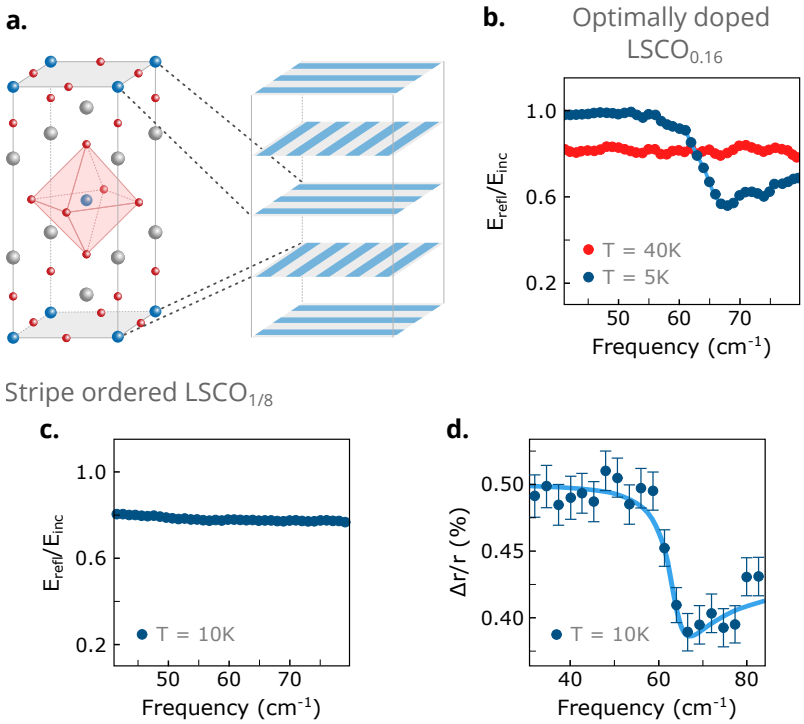

FIGURE 1.6: PHOTOINDUCED SUPERCONDUCTIVITY IN LSCO.

a. Crystal structure of La_2CuO_4, which is the basis of the Sr-doped $La_{2-x}Sr_xCuO_4$ family of high-T_c superconductors. The structure consists of single planes of copper oxide (blue spheres = Cu^{2+}, red spheres = O^{2-}) spaced by layers of lanthanum oxide (grey spheres = La^{3+}). For a certain range of doping around $x = 0.125$ a striped charge order develops where stripes are orthogonal in neighboring planes. **b.** Static c-axis electric field reflectivity of optimally doped $LSCO_{0.16}$ measured above (red dots) and below (blue dots) the critical temperature of $T_c = 38\,\mathrm{K}$. Below T_c a Josephson plasma edge is formed. **c.** Static c-axis reflectivity of stripe ordered $LSCO_{1/8}$ measured at 10 K. The response is flat. **d.** Transient c-axis reflectivity of stripe ordered $LSCO_{1/8}$ measured at 10 K and after excitation with 15 µm wavelength. The data was normalized to the static reflectivity. A plasma edge indicative of superconductivity developed. Figure adapted from [40] and [2].

observed statically at low temperatures in the optimally doped compound. Diffraction experiments on a similar high-T_c material ($La_{1.875}Ba_{0.125}CuO_4$) revealed, that MIR pulses tuned to this phonon are responsible to melt the stripe order which in turn restores the hidden superconducting phase [41].

Even more striking evidence of the capabilities of non-linear mid-infrared excitation was found in bilayer high-T_c cuprates. Upon resonant excitation of apical oxygen vibrations in YBa_2CuO_{6+x} (YBCO), signatures of superconductivity were found at much higher temperatures (up to room-temperature for $x = 0.45$) than the equilibrium T_c and in a wide doping range.
As measured by time-domain terahertz spectroscopy, below the transition temperature, equilibrium superconductivity is stiffened, while above T_c the incoherent conductivity becomes more coherent, a new reflectivity edge appears and the optical properties show an enhanced inductive response indicative of stronger inter-bilayer superconducting coupling [42, 43].

Figure 1.7 a schematically shows the crystal lattice structure of YBCO where the two copper-oxygen bilayers (green planes) are spaced by additional CuO_2 chains. Their distance to the bilayer planes adjusts the hole doping and thus is known to have a strong influence on T_c [44]. Therefore one can expect, that resonant excitation of these atoms to large phonon amplitudes (indicated as arrows) can also affect superconductivity.

Indeed, hard x-ray scattering experiments revealed that driving of the apical oxygen mode enhances inter-bilayer Josephson coupling at the expense of intra-bilayer tunneling strength while the number of Cooper pairs stays constant [45]. The atomic displacements lead to a decrease in inter-bilayer distance, and increase in intra-bilayer separation (see Fig. 1.7 b). A charge transfer from the CuO_2 planes to the inter-bilayer copper oxide, which is equivalent to self doping with holes was predicted by DFT calculations of the transient crystal structure and was also found experimentally at equilibrium (see [46]).
Further optical experiments measured a nonlinear coupling of the driven infrared active mode to the displacive Raman mode [47]. The periodic modulation of structural distances and associated periodic charge redistribution could be the cause for a dynamic stabilization of interlayer fluctuations [48–50].
The pseudogap phase shown in the generic phase diagram in Fig. 1.5 is a region with highly anomalous electronic properties where pre-formed Cooper pairs with lacking phase coherence might be available. It is conceivable that a nonlinear excitation could stabilize their phases and thus produce a transient superconducting state with a lifetime of few picoseconds.

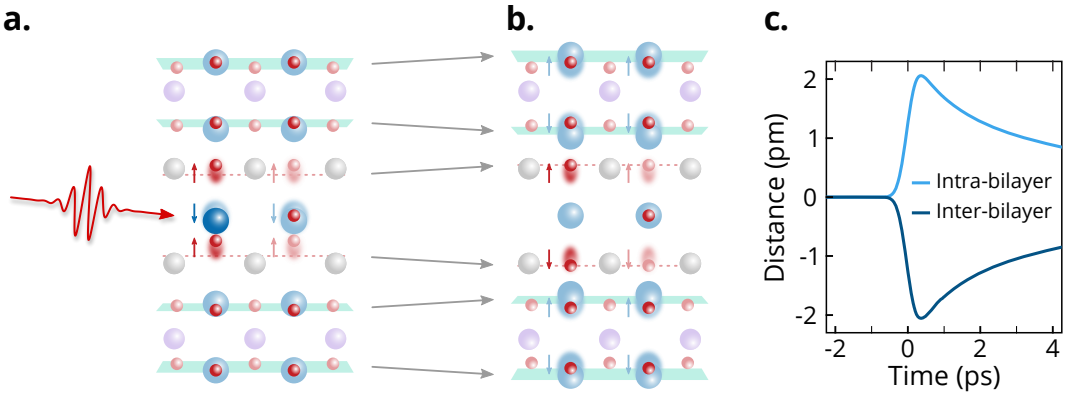

Figure 1.7: Photoinduced structural changes in YBCO supporting superconductivity.

a. Crystal structure of YBa_2CuO_{6+x}. It consists of two bilayer planes of copper oxide (blue spheres = Cu^{2+}, red spheres = O^{2-}). The intralayer space is filled by single atoms of yttrium (purple spheres) while the interlayer gap is composed of further copper oxide chains between barium atoms (grey spheres). MIR light can couple to this interlayer copper-oxygen mode. **b.** Reconstructed transient lattice structure after excitation. The distance of the apical Cu-O is decreased by 2.4 pm while the intra-bilayer distance increases. This is shown also for different time delays in **c.**. The transient distortion has a decay time on the order of few picoseconds. Results were obtained by hard x-ray scattering in combination with DFT simulations. Figure adapted from [45].

Although the low energy nonequilibrium control of broken-symmetry phases in correlated materials is still in its infancy and the physics at hand is not yet fully understood, the obtained results are undoubtedly spectacular.

The fact that intense THz pulses can create new transient crystal structures by direct excitation of infrared modes or indirect anharmonic coupling to other modes opens a wide playground for materials engineering.

One group of materials, which are of special interest in this context, are molecular solids. Here, electromagnetic waves have direct access to low energy molecular vibrational modes. These can not only influence the molecular structure via nonlinear couplings but also allow a direct interaction with electronic and orbital degrees of freedom. Organic molecular solids belong to the class of strongly correlated solids featuring a rich manifold of competing phases.

In the quasi-1D organic Mott insulator ETF_2TCNQ, excitation of an infrared active mode led to the coherent control of the onsite correlations [51]. Even more strikingly, a recent experiment reported in a similar charge transfer salt ($\kappa-(BEDT-TTF)_2Cu[N(CN)_2]Br$), a drastic increase in carrier mobility and the opening of a superconducting-like optical gap at a temperature far higher than the equilibrium critical temperature [52]. This type of photo-molecular superconductivity is the main focus of this thesis, however, in another molecular system, which we will review in depth in the next chapter.

2 The Organic Superconductor K_3C_{60}

In 1985 Kroto et al. discovered, that penta- and hexagons made of carbon atoms can form relatively large, hollow, spherical molecules (e.g. C_{60}, C_{70}) - the so called fullerides [53]. After Krätschmer et al. found a way to produce larger amounts of C_{60} by evaporation of graphite in a helium atmosphere [54], the chemistry and physics of this remarkable compound has been studied intensively.

In 1991, Haddon et al. showed, that metallic behaviour of solid C_{60} can be obtained by intercalation of alkali metal atoms [55]. Soon after, several groups discovered superconductivity in various intercalated compounds of type A_3C_{60}, where A equals potassium [56], rubidium [57, 58], or caesium [59]. Among organic molecular superconductors, these compounds have the highest superconducting transition temperatures of up to ~33 K at ambient pressure in case of $RbCs_2C_{60}$ [59].

This chapter summarizes the properties of alkali-doped fullerides with a focus on those important for superconductivity in K_3C_{60}.

2.1 Crystal Structure and Phase Diagram

In the C_{60} molecule, carbon atoms are covalently bound in 12 pentagons and 20 hexagons to form a sphere, similar to a soccer ball of about 7 Å in diameter (its shape is a truncated icosahedron). This structure belongs to the I_h point group, which has the highest symmetry possible. All hexagons are doubly bound with an average bond length of 1.391 Å while the pentagons consist of single bonds with an accordingly longer average length of 1.455 Å [60].

Not all C_{60} compounds crystallize in the same lattice structure. In case of A_3C_{60} where A = K or Rb, the C_{60} molecules form a f.c.c. lattice, while for Cs_3C_{60} besides this also an A15 structure that crystallizes in a b.c.c. lattice can be obtained. Figure 2.1 shows the cubic conventional cell of A_3C_{60} f.c.c.

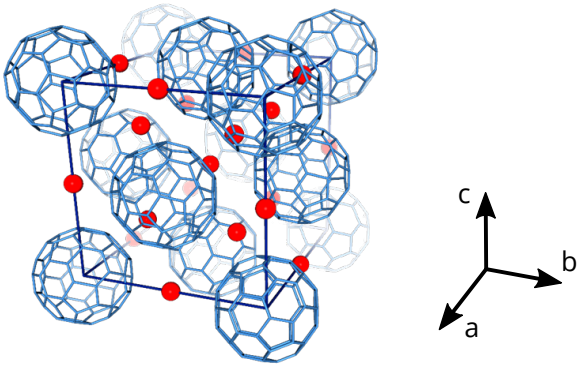

Figure 2.1: Molecular structure of K_3C_{60}.
The cubic unit cell is composed of C_{60} molecules (blue) arranged in an f.c.c. lattice with lattice constant of 14.24 Å at room temperature. The alkali atoms (red) are arranged in the interstitial spaces.

compounds where the alkali atoms shown in red arrange in the tetrahedral and octahedral interstitial spaces. Depending on the size of the alkali atoms, the lattice constant of the unit cell at room temperature changes from 14.24 Å for K_3C_{60} to 14.75 Å for Cs_3C_{60} [61, 62].

Figure 2.2 depicts a schematic of the phase diagram of the f.c.c. structure of A_3C_{60} compounds that was obtained from experimental data presented in [63]. The lattice constant of the unit cell is displayed on the upper axis, where arrows indicate the equilibrium values of the respective compounds. Thus, the lattice spacing can be tuned via this dopant dependent chemical pressure as well as by its hydrostatic equivalent (lower axis). With increasing unit cell size, electronic bands narrow due to a decreasing overlap of the molecular orbitals. This alters the balance between the Coulomb repulsion and the electronic kinetic energy and finally causes a metal-to-insulator transition. This Mott-insulating phase can be observed at larger lattice spacings, which occur in Cs_3C_{60} at ambient pressure due to the relatively large Cs ions.
The phase diagram features a wide, dome-shaped superconducting phase with relatively high critical temperature of ~ 35 K. In the superconducting phase, an increase of temperature across T_c leads to a metallic state. Different experiments have shown an isotropic (s-wave) symmetry of the superconducting order parameter as it is found in many conventional superconductors [64–66].
The proximity of superconducting and Mott-insulating phases resembles the phase diagram of the cuprates, although as we will see, superconductivity is mediated by very different mechanisms. At low temperatures around 2 K, a long range antiferromagnetic order is established in the insulating region of the phase diagram (not shown). This suppression of magnetic order in

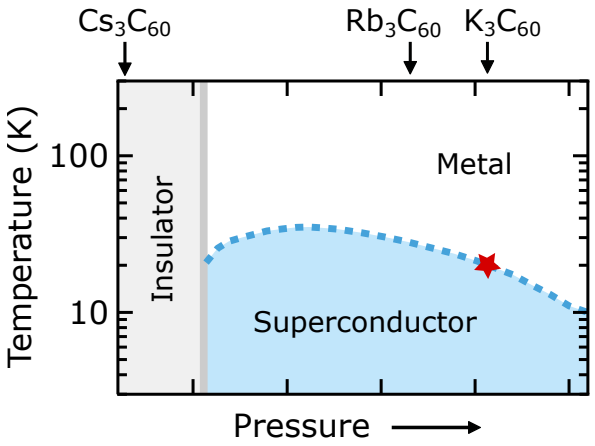

Figure 2.2: Phase diagram for f.c.c. A_3C_{60} (A = K, Rb, Cs) compounds.
This schematic was drawn according to experimental data presented in [63]. Increasing pressure (lower axis) is equivalent to a smaller lattice spacing (upper axis), that can be varied by exchanging the alkali atoms. The lattice spacing of the three molecular compounds Cs_3C_{60}, Rb_3C_{60} and K_3C_{60} at ambient pressure is marked with arrows. For large lattice spacing a Mott insulating phase is obtained while increasing temperature in the superconducting phase leads to a transition to a metallic state at T_c (dashed blue line). The red star indicates T_c of K_3C_{60} at ambient pressure.

contrast to the b.c.c. structure of Cs_3C_{60} is attributed to a large degree of spin frustration in the f.c.c. lattice that effectively lowers the materials Néel temperature [67].

2.2 Phonons and Molecular Vibrations

Phonons and their interaction with electrons are known to be of high importance for superconductivity in general. This also applies to the alkali-doped fullerides, for which we anticipate that a complex interplay of molecular vibrations with electronic degrees of freedom may be the origin of superconductivity.

Figure 2.3 depicts the different subgroups of possible phonons in the A_3C_{60} compounds. *Inter*molecular vibrations are situated in the low energy part of the spectrum. Here, the lowest frequency modes are librations of the C_{60} molecules (shown in red) with an energy in the range of $4-5\,\mathrm{meV}$. Intermolecular phonons are observable at slightly higher energy and can involve either only C_{60} molecules (acoustic modes, shown in green) or a relative motion of the C_{60} units and the alkali ions (optical modes, shown in blue). At

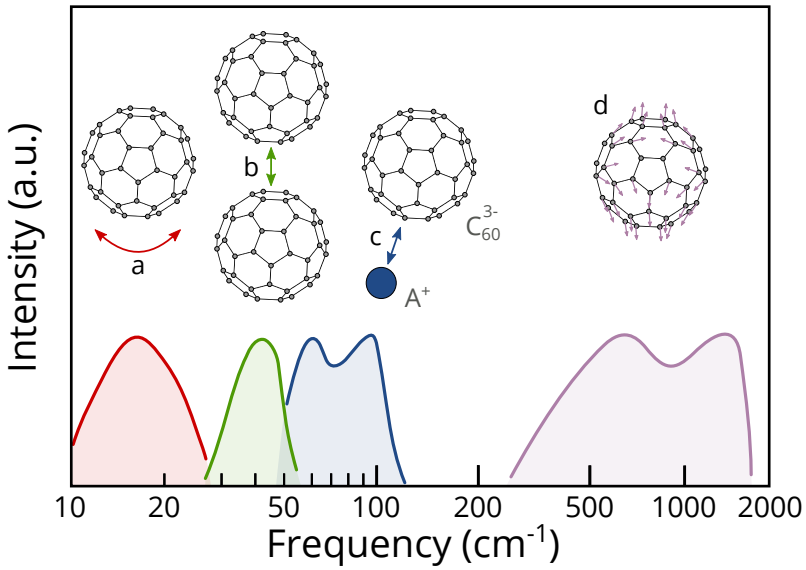

FIGURE 2.3: VIBRATIONS OF THE A_3C_{60} COMPOUNDS.
The vibrational spectrum is shown schematically in the lower part while the corresponding molecular dynamics is depicted above. At low frequencies librational modes of individual C_{60} molecules (a), intermolecular modes between two or more C_{60} units (b) as well as optical modes involving relative motion of a negatively charged C_{60} backbone and its positively charged alkali ion counterpart (c) dominate the spectrum. At higher frequencies various possible *intra*molecular modes dominate in a broad frequency range. Here, the $H_g(1)$ mode is depicted. Figure adapted from [69].

even higher energies of about 30 – 200 meV *intra*molecular vibrations on the C_{60} molecules develop. In principle $(3 \cdot 60) - 6 = 174$ intramolecular modes are possible within a single C_{60} molecule that due to the high molecular symmetry fall into 46 different vibrational levels. Out of these, 14 modes are optical (10 Raman active and 4 infrared active) and 32 are silent [68]. Due to the light mass of carbon atoms and high stiffness of the C-C bond, their energy is relatively high. Within the A_3C_{60} crystal structure its mode spectrum is softened compared to molecular C_{60} due to the charge transfer between A^+ ions and C_{60}^{3-} that weakens C-C bonds.

With respect to superconductivity, studying how superconducting properties are affected by the phonon energy scale may provide important insights on the pairing mechanism. In conventional superconductors, the substitution of atoms with isotopes of different mass leads to a change in $T_c \propto M^{-\alpha}$, where $\alpha = 0.5$ in BCS theory with a single type of ion of mass M [70].
In the case of A_3C_{60}, while the critical temperature is not changing when substituting alkali ions (cf. [71, 72]) a significant influence with $\alpha \sim 0.3$ was measured when ^{12}C is fully replaced by ^{13}C [73, 74]. This suggests that of all phonons only the pure C_{60} modes are likely to be involved in supercon-

ductivity whereas the A^+ ions only indirectly influence T_c by changing the unit cell size and therefore electronic interactions. This is due to efficient screening of the alkali ions which in turn reduces charge coupling to their modes [75].
The low energy librations of C_{60} have been measured by inelastic neutron scattering and no anomalous behavior was observed when cooling across T_c indicating a weak electron coupling to these modes [76]. By far the most significant contribution to superconductivity is attributed to the higher energy intramolecular modes [64, 70, 77–80]. There are several studies discussing a conventional phonon pairing mechanism within Migdal-Eliashberg theory that could reproduce the high transition temperature given the known phonon frequencies and measured electron-phonon coupling constant (λ ~0.5 – 1). A comprehensive summary of this can be found in Ref. [70].
Nevertheless, electronic correlations in the fullerides undoubtedly play an important role for superconductivity as we will see in the next section.

2.3 Electronic Properties

For the electrical conductivity of a crystalline solid, its electronic structure is fundamental. The C_{60} molecule contains 60 electrons occupying π-orbitals that protrude radially from the surface of the molecule (sometimes called "spherical porcupine"). The energy distribution of the respective orbitals is shown in Fig. 2.4 a.

Due to the high electron affinity of C_{60} in combination with the low ionization potential of alkali metals, intercalation of pure C_{60} with alkali atoms leads to ionic compounds where electrons are donated to the fullerene. In K_3C_{60} each C_{60}^{3-} molecule accepts three electrons from nearby alkali atoms which causes half filling in the triply degenerate t_{1u} lowest unoccupied molecular orbital (LUMO). Thus, the material changes from a semiconductor to a metal with half-filled conduction band t_{1u}, which is triply degenerate at the Γ point (cf. Fig. 2.4 b). The bandwidth is about 500 – 600 meV [81] and the density of states (DOS) at the Fermi level is ~13 states/eV per unit cell which was confirmed e.g. by photoemission and magnetic susceptibility measurements [82, 83].

Both the narrow bandwidth and low Fermi energy (~100 meV) are characteristic of molecular solids, where adjacent molecules have a large separation and thus a fairly small orbital overlap. This results in a relatively small car-

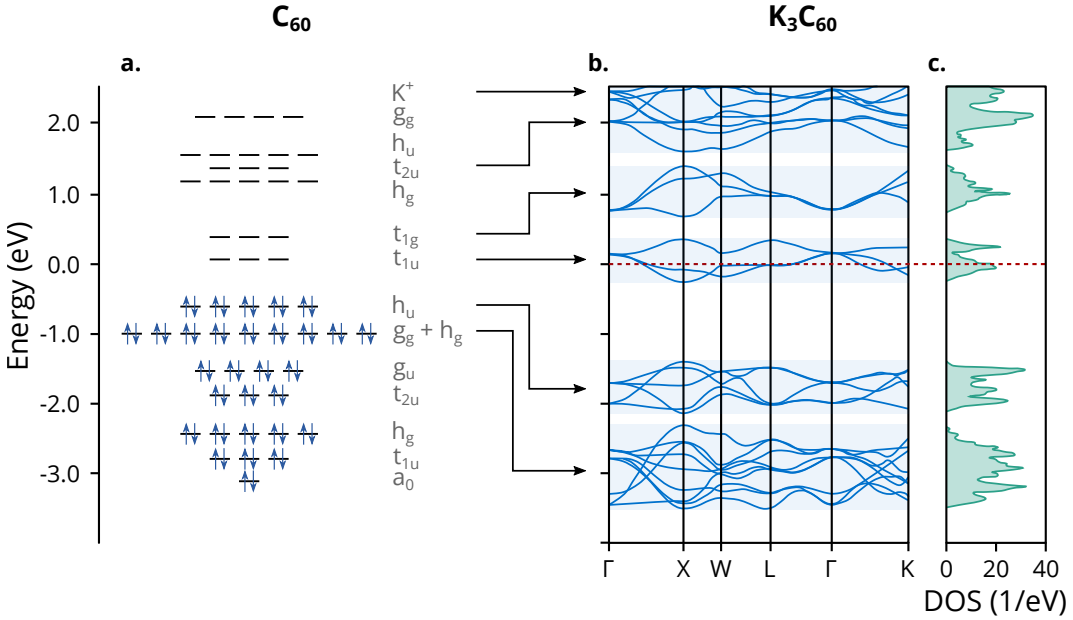

Figure 2.4: From molecular orbitals of C_{60} to the bandstructure of K_3C_{60}. **a.** shows Hückel calculations of the energy levels of a neutral C_{60} molecule. When a K_3C_{60} crystal is formed, multiple molecular orbitals are combined and form the electronic band structure shown in **b.** Each displayed band has its correspondence in the molecular orbitals in a. as indicated by the arrows. The Fermi level (red dashed line) crosses two of the t_{1u} bands. **c.** shows the combined density of states for both spins. Figure adapted from [69, 84, 85].

rier density and weaker hopping between molecules compared to ordinary metals. The Coulomb repulsion energy between two electrons on the same C_{60} molecule is on the order of $U \sim 1 - 2\,\text{eV}$ (Auger spectroscopy on undoped C_{60} retrieved $U \sim 1.6\,\text{eV}$ [86].) which is bigger than the bandwidth W of the low-energy bands. This results in an effective correlation strength $U/W \sim 1.5 - 3.0$ suggesting that electron correlations are not negligible in the alkali-doped fullerides. This was further confirmed by the discovery of the Mott insulating phase in Cs_3C_{60} (cf. Fig. 2.2).
Besides these Hubbard type Coulomb interactions, that depend on the total charge on a molecule and do not take the distribution on orbitals into account, multiplet effects have to be considered. Since a C_{60} molecule has three degenerate lowest unoccupied molecular orbitals that can be populated by dopant electrons, in case of A_3C_{60} the three unpaired electrons are subject to Hund's rule coupling favoring a high-spin state. As will be discussed in the next sections, however, electron-phonon interactions can counteract this force producing a singlet state that facilitates superconductivity. The multiplet splitting between the low spin (paired electrons on one of the t_{1u} orbitals) and high spin states was estimated to be ~110 meV by ab initio Hartree-Fock calculations [87].

2.4 Strongly Correlated Superconductivity in K_3C_{60}

This section is dedicated to superconductivity in K_3C_{60}. Characteristic parameters such as conductivity, magnetic susceptibility and superconducting gap are reviewed before possible mechanisms for Cooper pairing are discussed.

2.4.1 Properties of the Superconducting State in K_3C_{60}

Clear evidence of superconductivity in the A_3C_{60} family has been obtained through a variety of different experiments.
Necessary characteristic of this phase transition is a disappearing resistance accompanied by the formation of perfect diamagnetism. These properties have been measured and exemplary results are displayed in Fig. 2.5. Samples were prepared in the form of single crystals (cf. [88, 91, 92]) as well as

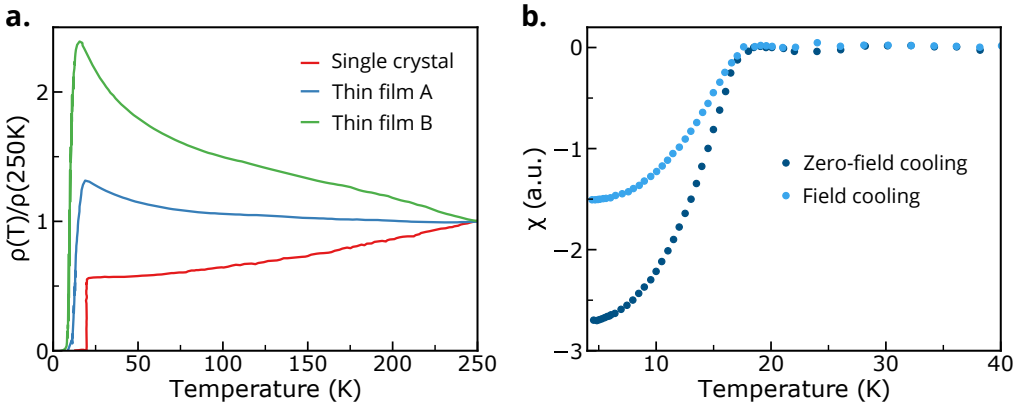

FIGURE 2.5: DC RESISTIVITY AND MAGNETIC SUSCEPTIBILITY OF K_3C_{60}

a. Temperature dependence of the DC resistivity for a K_3C_{60} single crystal (red, adapted from [88]) and for thin films (blue, green, adapted from [89]) where sample A has less disorder than sample B. Note that for comparison the resistivity of all samples was normalized to the value at 250 K. **b.** Magnetic susceptibility measurement on a K_3C_{60} powder sample. Dark blue dots indicate the susceptibility change upon application of a magnetic field when cooling was performed in absence of a magnetic field (ZFC) while light blue dots show the field cooling (FC) effect. Figure adapted from [90].

of pressed powder pellets and thin films (cf. [89, 90, 93–95]), all of which showed a superconducting transition around 20 K. However, as shown in Fig. 2.5 a, the behaviour of the resistivity during cooling in the normal state differs for monocrystalline and polycrystalline samples. In single crystals, the resistivity decreases continuously with decreasing temperature, while in thin films, depending on the degree of disorder, an opposite behavior near the transition temperature was found. This was interpreted as a weakly localized 3D metallic state in which electron-electron interactions are not negligible [89].

Above a temperature of ~ 300 K a metallic, linear dependence of the resistivity was found for K_3C_{60} and Rb_3C_{60} with no sign of saturation [96]. The electron mean-free path l was estimated of being shorter than the separation between the C_{60} molecules d suggesting strong interactions between the conduction electrons with intramolecular vibrational modes[1].

Susceptibility measurements of both single- and polycrystalline samples show a clear diamagnetic response below the critical temperature with superconducting volume fractions ranging from 40 – 90 % [98]. As depicted

1 For a normal metal the resistivity grows with increasing temperature due to increased scattering and when T becomes larger than typical phonon energies $\rho(T) \propto T$. With the semiclassical assumption that, at worst, an electron is scattered at every atom, the Ioffe-Regel criterion for the resistivity of metals predicts a resistivity saturation when $l = d$ resulting in $l \gtrsim d$ (cf. [97]). This criterion is violated for the alkali doped fullerides where measurements indicated $l \ll d$ at high temperatures.

in Fig. 2.5 b a significant difference was measured for zero-field cooling and field cooling experiments indicative of relevant flux pinning as in type-II superconductors. The A_3C_{60} compounds feature a relatively low critical magnetic field H_{c1} in the range of 10 mT, a large second critical field H_{c2} of ~15–80 T and correspondingly a very small coherence length ξ of ~30 Å [99]. This is comparable to ξ of other high-T_c superconductors but much smaller than the value for conventional superconductors (e.g. niobium: $\xi \approx 400$ Å). The penetration length λ_p, which is inversely proportional to the density of Cooper pairs, was measured to range between 240 – 480 nm [69].

Figure 2.6 a shows the T_c dependence on the lattice constant for various different compounds of the doped fullerides. Here, the lattice constant was adjusted by the choice of the dopant atom and by application of external pressure. For lattice constants smaller than 14.5 Å (i.e. under higher pressure) a linear relation can be observed, which is in good agreement with the predictions of BCS theory. As the lattice expands, electronic overlap of adjacent molecules decreases leading to a reduced bandwidth, larger density of states at the Fermi level and thus an increase in T_c (cf. Equation 2.2).
However, for Cs_3C_{60} a strong deviation from this linear trend was measured (cf. [100]) featuring a dome shape similar to other high-T_c superconductors.

Measurements of the size of the superconducting gap with respect to the lattice constant yielded similar results that fit very well to the BCS prediction as long as the lattice spacing is not increased above ~14.5 Å. For higher values, near the metal to insulator transition, deviations are significant (e.g. see NMR measurements in Cs_3C_{60} [103]).
For K_3C_{60} and Rb_3C_{60}, measurements of the superconducting gap via both optical- and tunneling spectroscopy are compatible with predictions from BCS theory [66, 102]. Figure 2.6 b shows the measured temperature dependent values of the superconducting gap (circles and triangles) along side with the corresponding mean field behavior from BCS theory (grey dashed line). Interestingly, while some reports (cf. [78, 102, 104, 105]) indicate that the ratio between the superconducting gap and the measured T_c is in agreement with BCS theory

$$2\Delta_0/k_B T_c = 3.52, \tag{2.1}$$

some other studies shows significantly higher ratios, indicative of a stronger coupling [64, 66].

In all alkali-doped fullerides, the symmetry of the superconducting order parameter was experimentally determined by different techniques to be s-

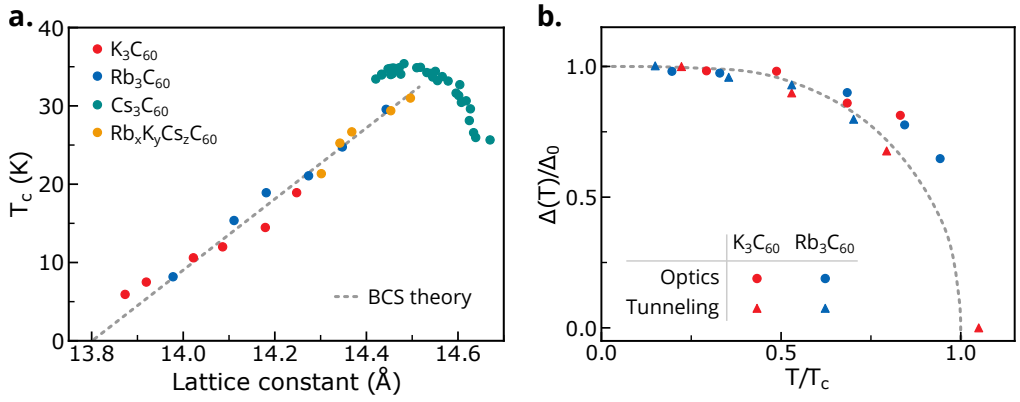

FIGURE 2.6: SCALING OF $T_c(p)$ AND $\Delta(T)$ FOR VARIOUS A_3C_{60} COMPOUNDS IN COMPARISON TO BCS PREDICTIONS.

a. Critical temperature vs. lattice constant for various doped fullerides. T_c was obtained via diamagnetic shielding measurements for K_3C_{60} (red), Rb_3C_{60} (blue) and compounds with mixed composition (orange) and via NMR for Cs_3C_{60} (green). The respective lattice constant was measured by x-ray diffraction. Data obtained from [62, 100, 101]. The linear relation expected by BCS theory is shown as grey dashed line. **b.** Normalized superconducting gap $\Delta(T)/\Delta(T = 0\,\mathrm{K})$ for K_3C_{60} (red) and Rb_3C_{60} (blue) vs. temperature (scaled by T_c) measured by optical- (circles) and tunneling spectroscopy (triangles). The grey dashed line depicts the temperature dependence predicted by BCS theory. Data obtained from [66, 102]

wave, i.e. it has an isotropic magnitude and a fixed phase in all directions [65, 106–109]. Furthermore, spin fluctuations were shown to be suppressed in the superconducting state indicating a singlet pairing (cf. NMR measurements in [110]). This might be a key ingredient for the formation of Cooper pairs in K_3C_{60}.

2.4.2 MECHANISMS FOR PAIRING

Early theories aimed at describing superconductivity in doped fullerides can be divided into two categories, with either electron-phonon coupling (e.g. [111, 112]) or sole electron-electron coupling (e.g. [113]) having the most important influence.
Both approaches could describe several experimental observations including the isotope-effect and the size of the superconducting gap but failed to describe the full phase diagram [69, 70, 114].

In metals, the typical ratio between its phononic energy scale ($\omega_{ph} \sim 10 - 100\,\text{meV}$[2]) and electronic bandwidth ($W \sim 10\,\text{eV}$) is about $\omega_{ph}/W \sim 0.1\,\% - 1\,\%$, which is small due to the big difference between the electronic and nuclear masses [79]. In conventional superconductors, the weak attractive interaction between electrons that is necessary for pairing is attributed to their interaction with phonons. A small value of ω_{ph}/W is often considered important for superconductivity since retardation effects can reduce the repulsive Coulomb interactions so that these can be treated as a weak Coulomb pseudopotential μ^* [115]. In the BCS-equation this is used to calculate the critical temperature T_c:

$$T_c = \omega_c e^{-1/(\lambda - \mu^*)} \tag{2.2}$$

where $\lambda = N(E_F)V_0$ denotes the electron-phonon coupling strength with the density of states at the Fermi-level $N(E_F)$. V_0 is the interaction potential between electrons and (phononic) excitations with characteristic frequency ω_c.

In contrast, as described in Section 2.2, in the fullerides the intramolecular phonon energies of up to 200 meV are significantly higher, while the electronic bandwidth of about 500 meV is much smaller resulting in comparable energy scales. This suggests that retardation effects are rather small. For an efficient reduction of μ^* electrons must be able to move quickly between molecules. In A_3C_{60}, however, the electrons cannot efficiently avoid each other if they are sitting on the same C_{60} molecule while hopping is weak (e.g. within BCS theory, the weak-coupling approximation $\omega_0 << E_F$ is no longer valid).
Furthermore, the Coulomb repulsion of electrons on the same molecule is much larger ($U \sim 1.6\,\text{eV}$, cf. Section 2.3) than the phonon mediated attraction so that explanations similar to those put forward for pairing in conventional superconductors are not sufficient to explain the observations for doped fullerides.

Strikingly, in A_3C_{60} the coupling energies according to Hund's rule and Jahn-Teller phonons[3] are also of comparable magnitude (~100 meV). In the fullerides, by symmetry, only A_g and H_g modes can couple to t_{1u} electrons whereas only H_g modes provide notable coupling strength [79]. While Hund's rule always favors a high-spin state, interaction with Jahn-Teller phonons has shown to promote a low-spin state [114]. When writing the total exchange interaction as $J = J_{Hund} + J_{ph}$ it turns out that for the

2 cf. Debye temperature Θ_D for conventional superconductors
3 The Jahn-Teller effect describes a distortion of certain molecules with a degenerate electronic ground state which lifts this degeneracy and lowers the overall energy. Jahn-Teller phonons support such a distortion.

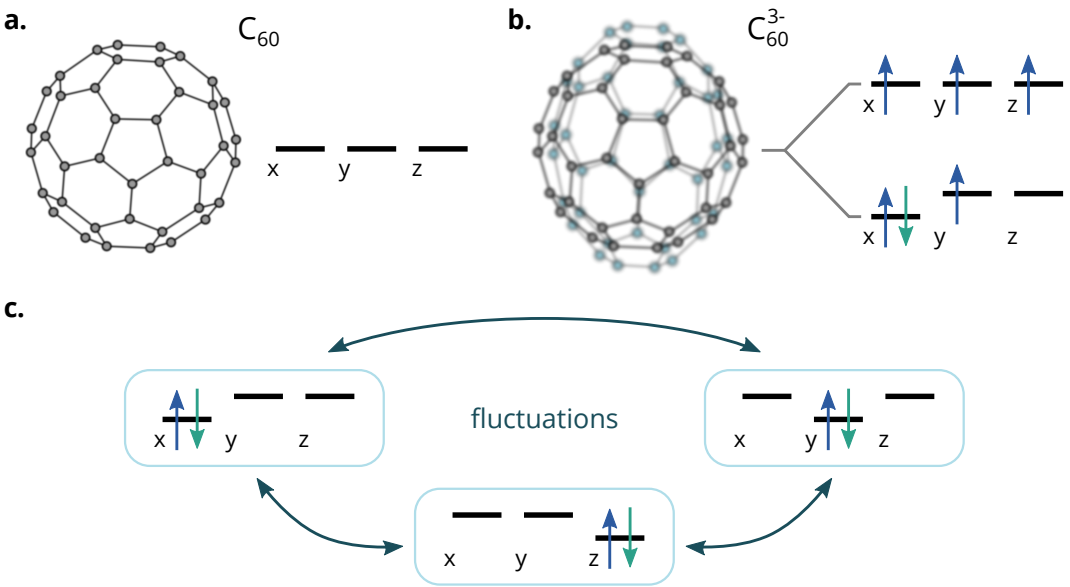

FIGURE 2.7: MECHANISM FOR LOCAL PAIRING IN A_3C_{60}

a. Molecular C_{60} has three degenerate lowest unoccupied t_{1u} orbitals **b.** In A_3C_{60} these get filled with three electrons. According to Hund's rule a high-spin state is favored while Jahn-Teller active H_g phonons renormalize the effective exchange energy and thus promote a low-spin state in the dynamically distorted molecule. **c.** The singlet state is subject to orbital fluctuations that allow coherent interorbital pair delocalization, which promotes superconductivity. For clarity the third electron has been omitted.

fullerides the negative phonon-mediated exchange interaction prevails over the positive Hund's coupling resulting in a lift of the degeneracy of the electronic conduction band and an inverted Hund's rule (see Fig. 2.7). Several studies developed a model for local intraorbital pairing based on this interaction [87, 116–118] and it was even possible to reproduce the experimental phase diagram with *ab initio* calculations [114].
More details on the dynamical Jahn-Teller coupling in A_3C_{60} compounds can be found in [119, 120]. Furthermore, Kim et al. have shown that the Jahn-Teller stabilized intramolecular singlet pair is subject to orbital fluctuations which provide coherent interorbital delocalization of the pair and thus are supporting superconductivity [121].

In summary, the interesting physics and exotic behavior of alkali doped fullerides is arising from many competing effects and unusual ratios between electronic and phononic energy scales and can only be described if electron-phonon interactions as well as electronic correlations and orbital degeneracy are taken into account.

3 Light Induced Superconductivity in K_3C_{60}

In this chapter a summary of earlier work is presented (cf. [122, 123]), which showed that excitation of K_3C_{60} with femtosecond laser pulses in the mid-infrared range leads to superconducting-like optical properties far above the equilibrium critical temperature.
We begin by discussing the equilibrium optical properties of K_3C_{60}. We will then describe how mid-infrared pulses can be used to induce an out-of-equilibrium superconducting response and discuss how this nonequilibrium state behaves in high pressure settings. Finally, we will discuss how the accessibility of this state can be improved and how additional measurements can clarify the nature of the photo-induced state.

3.1 Equilibrium Optical Properties

The optical properties of a material represent an ideal messenger for electronic excitations and collective modes as well as phononic processes in solids. An electromagnetic wave $\mathbf{E}(\mathbf{q},\omega)$ with wavevector $\mathbf{q}$ and frequency ω incident on a medium will interact with its electric charges inducing a polarization $\mathbf{P}(\mathbf{q},\omega)$ and thus creating a displacement field in the form of:

$$\mathbf{D}(\mathbf{q},\omega) = \epsilon_0\mathbf{E}(\mathbf{q},\omega) + \mathbf{P}(\mathbf{q},\omega) = \epsilon(\mathbf{q},\omega)\epsilon_0\mathbf{E}(\mathbf{q},\omega) \tag{3.1}$$

Here, the complex dielectric constant $\epsilon(\mathbf{q},\omega) = \epsilon_1(\mathbf{q},\omega) + i\epsilon_2(\mathbf{q},\omega)$ is the response function describing electric polarization effects microscopically[1][124]. All other optical properties including macroscopic observables such as the complex refractive index $N = n + ik$ with real part n and extinction coefficient k can be recalculated from this quantity.

1 Accordingly, the polarization can be described by $\mathbf{P}(\mathbf{q},\omega) = (\epsilon(\mathbf{q},\omega) - 1)\epsilon_0\mathbf{E}(\mathbf{q},\omega) = \chi(\mathbf{q},\omega)\epsilon_0\mathbf{E}(\mathbf{q},\omega)$ with $\chi(\mathbf{q},\omega)$ and ϵ_0 being the susceptibility of the medium and the electric permittivity of the vacuum, respectively.

In optical spectroscopy apart from obvious quantities such as the frequency dependent optical reflectivity $R(\omega)$ as well as transmittance $T(\omega)$ and absorbance $A(\omega)$, often the relationship between electric field and induced current density $\mathbf{J}(\mathbf{q},\omega)$ is analyzed. The corresponding response function σ relates the electric field to the induced current from Ohm's law according to

$$\mathbf{J}(\mathbf{q},\omega) = \sigma(\mathbf{q},\omega)\mathbf{E}(\mathbf{q},\omega) \tag{3.2}$$

with the complex optical conductivity $\sigma(\mathbf{q},\omega) = \sigma_1(\mathbf{q},\omega) + i\sigma_2(\mathbf{q},\omega)$ [124]. This optical conductivity is an extension of the DC electrical conductivity and a fundamental parameter often used to describe the electromagnetic response of a system - especially in the frame of low-energy spectroscopic investigations.

The optical properties of a metal and a superconductor feature distinct spectroscopic signatures in $R(\omega)$ and $\sigma(\omega)$ that distinguish the two ground states, which we will discuss in detail later in this chapter. All measurements in this work were conducted with compacted K_3C_{60} powder samples having an average grain size of 100 – 400 nm. To prevent oxidation of the sensitive material, all sample handling was performed in an inert atmosphere with oxygen level < 1 ppm and for optical experiments it was sealed in a dedicated sample holder and pressed against a diamond window. This guaranteed an optically flat interface. For details on the sample preparation see Appendix A.
Figure 3.1 shows the static reflectivity as well as $\sigma_1(\omega)$ and $\sigma_2(\omega)$ of such a sample as measured at the SISSI beamline[2] using a commercial Fourier transform infrared spectrometer equipped with a microscope [123]. Different temperatures between 25 K and 300 K could be reached by means of a helium cooled cryostat. After referencing and extrapolation of the spectra[3], the complex valued optical conductivity was retrieved through a Kramers-Kronig transformation for samples in contact with a transparent window [126]. The exact procedure for obtaining the optical conductivity is also published in [127, 128].

The equilibrium optical properties of K_3C_{60} show a metallic behavior above T_c which is characterized by a wide Drude peak in $\sigma_1(\omega)$ centered at zero frequency and a relatively high low frequency reflectivity of about 90 %. At higher frequencies this response of free carriers is accompanied by an additional polaronic absorption visible in $\sigma_1(\omega)$ between 50 meV and 100 meV.

2 Elettra Synchrotron Facility, Trieste, Italy

3 The K_3C_{60} reflectivity spectra were referenced against a gold mirror placed at the sample position. The low energy part of the spectrum (< 5 meV) was extrapolated using a Drude-Lorentz fitting while for the high energy side (> 500 meV) data on K_3C_{60} single crystals was used [102, 125].

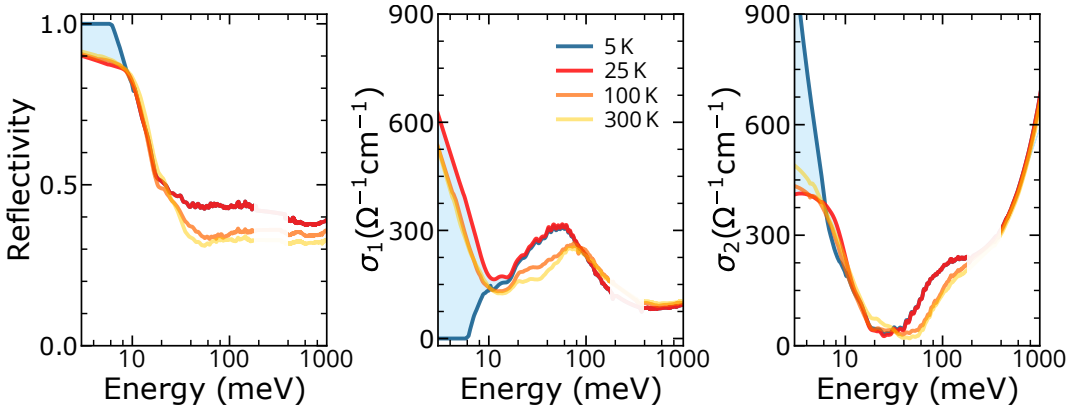

Figure 3.1: Temperature dependence of the static optical properties of K_3C_{60}. The graphs show frequency dependent values of the sample reflectivity (left panel) as well as real (middle panel) and imaginary part (right panel) of the optical conductivity for four different temperatures. Red colors indicate temperatures above T_c while the blue trace was recorded below. The blue shaded region highlights the difference between the optical properties just above as compared to below T_c. The paled region in the plot indicates the diamond absorption window.

At even higher energies interband electronic transitions determine the shape of the optical conductivity [125].

Figure 3.1 shows the frequency dependent optical properties for various temperatures up to room temperature. In the temperature range above T_c (red, orange and yellow curve), the optical properties of the K_3C_{60} pellet samples do not show a strong temperature dependence. Only the polaronic peak ($\sim 50-100$ meV) changes its shape from a clean Lorentzian peak to a more deformed one.
Cooling below the superconducting transition temperature (blue curve), in contrast, results in significant changes in the low-frequency optical properties. The low frequency reflectivity saturates to one, a gap forms in $\sigma_1(\omega)$ up to ~ 6 meV and $\sigma_2(\omega)$ diverges in the same frequency range. These changes are typical signatures of a phase transition to a superconducting state. In contrast to a metal, the density of states of a superconductor features a 2Δ wide gap that corresponds to the energy necessary to break Cooper pairs. This superconducting gap is visible in the real part of the optical conductivity. Since the area under the curve must be conserved, the spectral weight of $\sigma_1(\omega)$ above T_c is partly shifted towards zero frequency, where one would expect a δ function for an ideal superconductor. This is the signature of a superconductor capable of carrying a DC current without any dissipation. In the same frequency band, $\sigma_2(\omega)$ diverges towards lower energies. This divergence has a $1/\omega$ dependence which is the Kramers-Kronig equivalent of a pole in the real part of $\sigma(\omega)$ at $\omega = 0$.

Intuitively, this can be understood when assuming that carriers can move freely without scattering in a superconductor and get accelerated more and more with an external electric field. In this case the following relation applies to the effective force F, applied by the external field $E(\omega)$ on the charge q with mass m acceleration a and velocity v:

$$F \propto qE \propto ma \propto m\dot{v} \text{ with } E \propto cos(\omega t) \tag{3.3}$$

Since we know that the complex conductivity σ is proportional to the current density (cf. Equation 3.2), which directly depends on the velocity v of the carriers, the $1/(\omega)$ dependence is obvious from:

$$\sigma_{sc} \propto j \propto v \propto \int adt \propto \frac{1}{\omega} sin(\omega t) \tag{3.4}$$

The measured conductivity spectra were fitted by a combination of a Drude term centered at $\omega = 0$ denoting the free-carriers and a Lorentz oscillator reproducing the mid-infrared absorption at higher frequencies ($\omega_0 \sim 50 - 100$ meV):

$$\sigma_1(\omega) + i\sigma_2(\omega) = \frac{\omega_p^2}{4\pi} \frac{1}{\gamma_D - i\omega} + \frac{\omega_{p,osc}^2}{4\pi} \frac{\omega}{i(\omega_{0,osc}^2 - \omega^2) + \gamma_{osc}\omega} \tag{3.5}$$

Here, ω_p and γ_D are the plasma frequency and scattering rate of the Drude term, while $\omega_{p,osc}$, γ_{osc} and $\omega_{0,osc}$ are the oscillator strength, the linewidth, and the resonance frequency of the additional Lorentz term. The result of the fit is shown as red curve in Fig. 3.2. The equilibrium data reported here were used to normalize the transient optical spectra of K_3C_{60} measured upon photoexcitation, as discussed in detail in Appendix D.1.

These properties have been measured on K_3C_{60} single crystals [125] and on compacted powder samples [123] giving qualitatively similar results. The strongest changes of the optical properties, when comparing above and below T_c data, were found at low photon energies up to about $3\Delta(T)$ [104], which is in good agreement with our results. However, the data on single crystals features a higher far-infrared spectral weight compared to the data on pellet samples as both Drude and Lorentz terms of Equation 3.5 have a higher plasma frequency. From their relative peak ratio we can deduce that most carriers are localized in the polaronic peak which does not contribute to metallic transport. The extrapolated DC conductivity value of $\sigma_1(\omega)$ is smaller in the powder samples ($\sim 1000\,\Omega^{-1}\text{cm}^{-1}$) than in single crystals ($\sim 1500\,\Omega^{-1}\text{cm}^{-1}$). Here, the granularity of the powder samples might result in a non-negligible reduction of the overall carrier density and pro-

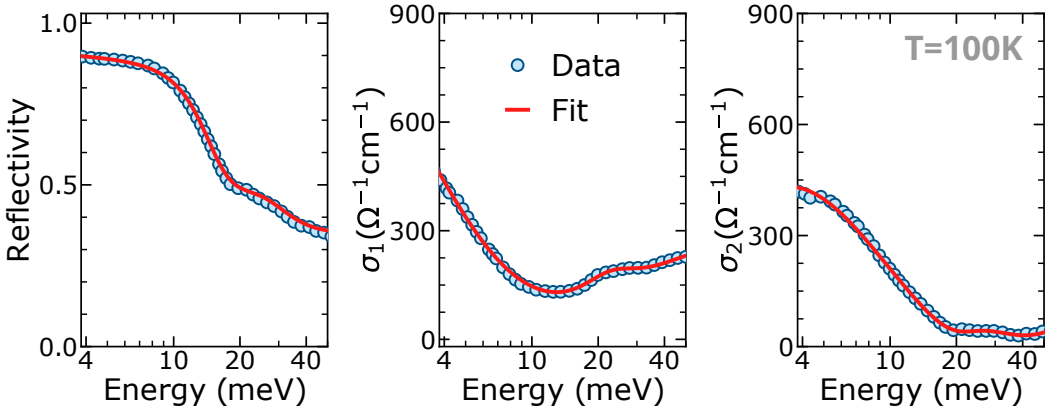

Figure 3.2: Drude-Lorentz fit to the equilibrium optical properties of K_3C_{60}. Reflectivity, real and imaginary part of the optical conductivity were measured at a temperature of 100 K (blue dots). The red curve is the Drude-Lorentz fit as described by Equation 3.5 and in the text.

mote a higher degree of charge localization. This is further supported by the reduced scattering rate of the Drude carriers in the polycrystalline sample (~ 4 meV as compared to 17 meV in single crystals [125]). This effect can be caused by both lower electron density (and thus fewer scattering events) and stronger charge localization at grain boundaries.

3.2 Excitation with Mid-Infrared Light

Superconductivity in potassium doped fullerides is strongly associated with electronic correlations and electron-phonon interactions - especially with the intramolecular modes of the buckyballs (cf. Section 2.4). A selective excitation of these Jahn-Teller active modes, leading to dynamic lattice distortions, could therefore be expected to influence the electronic order (cf. [51, 129]) and possibly the superconducting state and in particular its onset.

Since these dynamical Jahn-Teller distortions in C_{60} are Raman active H_g modes, they cannot be driven by light directly. As described in Section 2.2, out of the 46 different vibrational modes only 4 T_{1u} modes are infrared active. However, in the I_h symmetry group of C_{60} a nonlinear phononic coupling (cf. Section 1.1) of the T_{1u} modes to the three Raman modes with A_g, T_{1g} and H_g representation is allowed by symmetry (these modes preserve the total symmetry of the system) [130, 131].

Thus a strong excitation of T_{1u} optical phonons (which have energies

in the mid-infrared frequency range at $E < 200\,\text{meV}$) can induce an effective displacement along the Raman mode coordinate by means of a nonlinear phononic coupling. This allows the indirect excitation of H_g breathing modes of the buckyballs, which are known to have a significant influence on superconductivity. Because of this relationship, excitation with mid-infrared light was considered as a potential tool to coherently control the superconducting properties of alkali doped fullerides.

With this guiding idea in mind, in an earlier work (cf. [123]) ultrashort mid-infrared laser pulses have been used to resonantly excite powder samples of K_3C_{60} both above and below its critical transition temperature. The response of the system to this stimulus was measured by means of THz time-domain spectroscopy covering the spectral region with most prominent changes between metallic and equilibrium superconducting phase (cf. Fig. 3.1, in particular the region of the Drude peak in $\sigma_1(\omega)$ and respectively the superconducting gap Δ_{sc} of ~ 6 meV). The pump pulses were tuned to be in resonance with the $T_{1u}(4)$ vibrational mode at 170 meV ($\lambda = 7.4\,\mu\text{m}$) with a fluence of few mJ/cm² and a pulselength of ~ 300 fs.

Figure 3.3 shows a comparison of the equilibrium optical properties above and below T_c (panel a., $T = 100\,\text{K}$ in red and $T = 5\,\text{K}$ in blue) with photoexcited optical properties measured at 100 K (blue curves in panel b.). The data shown here were recorded under the same excitation conditions as in [123] but measured with a broader spectral window from $5-31\,\text{meV}$. Strikingly, all features that characterized the equilibrium superconducting state, can be revived upon photoexcitation. At a pump-probe time delay of 1 ps, the reflectivity saturates at $R = 1$ for all frequencies below 10 meV, a gap opens in $\sigma_1(\omega)$ and a corresponding $1/\omega$ divergence appears in $\sigma_2(\omega)$.The clear similarity of the transient optical properties with the equilibrium superconducting phase suggests an interpretation of the MIR light-induced state as a transient superconductor. $\sigma_1(\omega)$ stays depleted up to even higher frequencies of ~ 10 meV compared to the equilibrium superconducting gap value of ~ 6 meV and resembles the gap of a superconductor at finite temperatures with residual in-gap spectral content. This can be due to both the high temperature of the sample and the finite lifetime of the state.
For longer pump-probe delays the effect gradually disappeared and about 5 ps after the excitation the optical properties almost fully relaxed back to their equilibrium values. Figure 3.4 a displays the average value of $\sigma_1(\omega)$ in the region up to 10 meV for different time delays with respect to the excitation. From this, the depletion of spectral weight caused by the laser pulse is evident and a life time of this state of less than two picoseconds can be extracted.

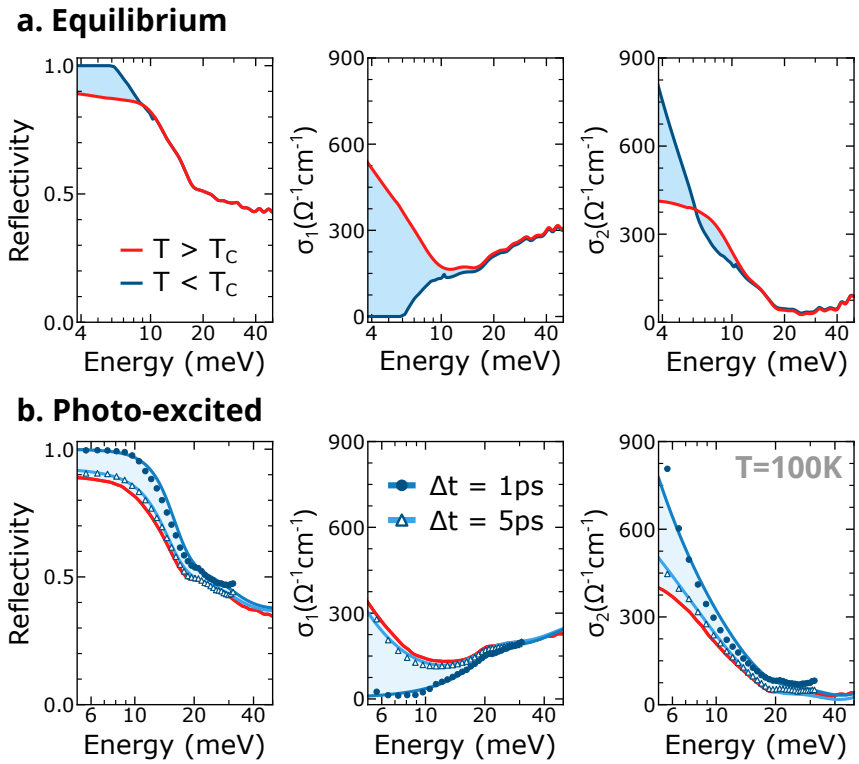

Figure 3.3: Equilibrium and light-induced optical properties in K_3C_{60}.
a. Equilibrium reflectivity (sample-diamond interface), real, and imaginary part of the optical conductivity of K_3C_{60} measured upon cooling across the equilibrium superconducting transition. **b.** Same quantities measured at equilibrium (red lines), 1 ps (blue filled dots), and 5 ps (light blue triangles) after photoexcitation. The light and dark blue lines are Drude-Lorentz fit to the transient optical data (see Section 3.1 and Appendix D.2 for more details). These data were acquired at a base temperature $T = 100\,\mathrm{K}$ with a fluence of $3\,\mathrm{mJ/cm^2}$.

3.2.1 Dependence on Pump Wavelength and Fluence

A wavelength dependence of the pump was measured in the region of 80 – 700 meV excluding the absorption of the diamond window (~ 250 – 500 meV) and is shown in Fig. 3.4 b. Within this range a rather broad spectral response was measured, which showed no distinct characteristics of a resonance. The effect seemed to be strongest around 120 – 180 meV, where two of the four T_{1u}-modes reside ($T_{1u}(3) \approx 140$ meV and $T_{1u}(4) \approx 170$ meV, indicated as red dashed lines) but a weaker effect is still observed for lower photon energies towards $T_{1u}(1,2)$. In contrast, at much higher pump energies around 600 meV, no light-induced depletion could be measured. This is in line with the interpretation that low energy vibrations might be involved in the stimulated and possibly superconducting response.
A fluence dependence with values ranging from zero to 3 mJ/cm² showed a continuous enhancement of the effect with increasing fluence. There was no sharp threshold observable and neither could a clear saturation be determined (cf. Fig. 4 in [123]).

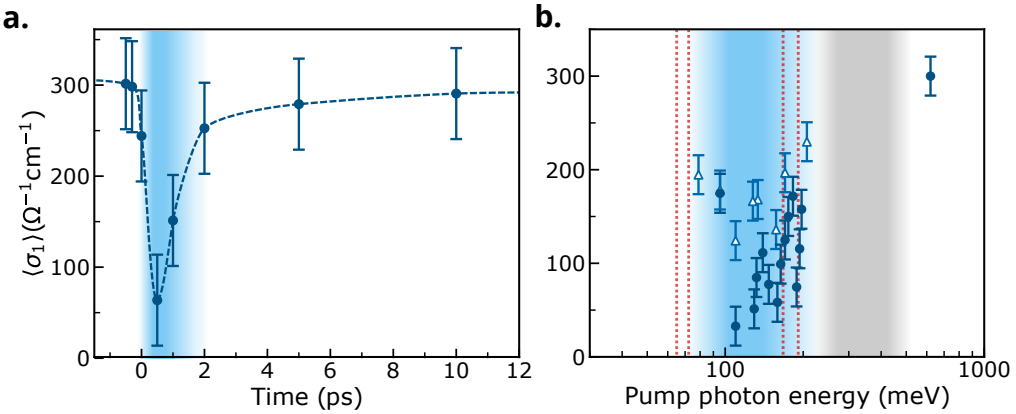

Figure 3.4: Lifetime and wavelength dependence of the light-induced optical properties.
a. Time dependence of the average real part of the optical conductivity in the region of the superconducting gap. The opening of the gap only lasts for few picoseconds after the excitation pulse. **b.** Same average value of $\sigma_1(\omega)$ as in a. but plotted for different pump wavelengths. The dashed red vertical lines correspond to frequencies of the four $T_{1u}(1,2,3,4)$ vibrational modes. In the blue shaded regions the response could be fitted with a model for a superconductor while the gray shaded region shows where absorption of the diamond window did not allow pump-probe experiments. Triangles with white filling correspond to measurements with a fluence of 0.4 mJcm^{-2} while solid blue dots represent a higher fluence of 1.1 mJcm^{-2}. Both graphs were adapted from data in [123].

3.2.2 Dependence on Temperature

With respect to temperature, a gradually decreasing light-induced effect could be observed for increasing temperatures. As shown in Fig. 3.3 at 100 K, the optical response resembles the equilibrium properties below T_c. However, at 200 K and even more at 300 K the characteristic features in the optical conductivity are reduced resulting in only partial enhancement of reflectivity, incomplete gapping in $\sigma_1(\omega)$ and less pronounced divergence in $\sigma_2(\omega)$. Further details of this effect will be discussed in Section 5.1.2.
Interestingly, for temperatures below the equilibrium superconducting phase transition of K_3C_{60}, irradiation with the same laser pulses that led to an enhancement of the characteristic features above T_c now weakens superconductivity. At these low temperatures mid-infrared irradiation can wipe out the thermally induced superconducting features: the reflectivity is reduced and the gap in $\sigma_1(\omega)$ is filled while at the same time a lower divergence in $\sigma_2(\omega)$ indicates a reduced number of superconducting carriers. After excitation it takes about 100 ps until the superconducting state is restored [127] which is compatible with typical recombination times of Cooper pairs [132, 133]. Unlike for excitation above T_c, here the gap size is not influenced by the mid-infrared stimulus. Thus the pump-induced effects observed at temperatures below equilibrium T_c of K_3C_{60} are likely caused by light-induced breaking of Cooper pairs.

3.2.3 Dependence on Hydrostatic Pressure

Despite the substantial similarity of the optical properties obtained after cooling of K_3C_{60} into its superconducting state with the optical properties measured directly after photo-excitation, further evidence is needed to justify the interpretation of light-induced superconductivity.
One tuning parameter that is compatible with ultrashort optical experiments and that influences metallic and superconducting properties in a distinguishable way is external pressure. As described already in Chapter 2.4.1, adjustment of the lattice constant in the alkali doped fullerides directly translates into a change of T_c. Figure 2.6 a shows a linear variation of the critical temperature over more than 25 K when the lattice constant is changed by less than 1 Å. Since organic compounds have a reasonably low bulk modulus (~ 28 GPa for K_3C_{60}, cf.[134]) due to the weak Van der Waals interactions that retain the molecules, the size of their unit cell is highly sensitive to application of external pressure [62]. Accordingly,

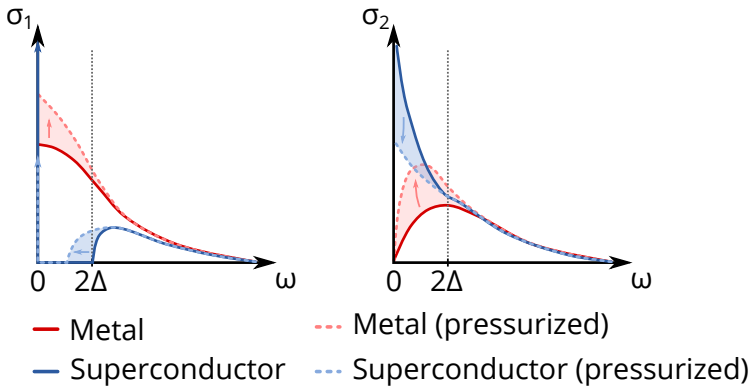

Figure 3.5: Schematic representation of the influence of pressure on the optical properties of a metal and a superconductor.
The response of the metallic state upon application of pressure is depicted in red, while the reaction of the superconducting state is shown in blue. The reason for this opposing behavior is explained in the text.

a linear dependence of T_c on pressure was simulated and confirmed by magnetization experiments [134–136].
When external pressure is applied, the unit cell is scaled down leading to a bigger overlap of molecular orbitals which results in an effective broadening of the electronic bands. This is supported by first-principles local-density band structure calculations [137, 138].
In the equilibrium metallic state a larger electronic bandwidth results in a stronger band curvature at the Fermi-level which is equivalent to a decrease of the effective electron mass m_e^*, resulting in a higher DC conductivity.
In contrast, the effect of external pressure is very different for a BCS-superconductor since the condensation of Cooper pairs is typically favored for slow electrons with high effective mass so that the Coulomb repulsion of electrons can be compensated by strong electron-phonon interactions. In other words, a larger bandwidth effectively decreases the density of states at the Fermi-level which for most superconductors according to BCS-theory decreases the size of its gap and therefore the critical temperature T_c (cf. Equation 2.2).

Figure 3.5 displays the suspected influence of pressure on real and imaginary part of the optical conductivity schematically. For a metallic state the overall conductivity is enhanced, which is characterized by an increased value of the Drude peak in $\sigma_1(\omega)$ and also a higher average imaginary part of the conductivity. Due to finite scattering, for low frequencies $\sigma_2(\omega)$ still runs towards zero. In comparison, the superconducting state, characterized by a δ-function in $\sigma_1(\omega)$ at zero frequency and $1/\omega$-divergence in $\sigma_2(\omega)$, is weakened. This is indicated by a reduced spectral weight of the condensate at zero frequency forming a smaller gap in $\sigma_1(\omega)$ and a less pronounced di-

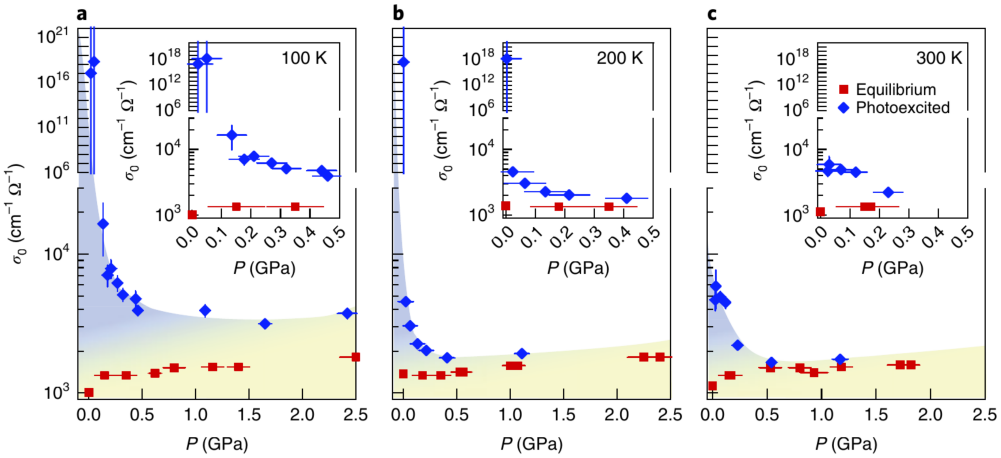

Figure 3.6: Pressure dependence of the extrapolated optical conductivity. Drude-Lorentz fits to the complex optical conductivity were extrapolated to zero-frequency to obtain a value σ_0 corresponding to the DC conductivity. This value was obtained from equilibrium data (red squares) as well as from transient optical spectra after photo-excitation (blue diamonds) and for three different temperatures **a.** at 100 K, **b.** at 200 K and **c.** at 300 K. In the blue shaded areas σ_0 is suppressed by pressure ($d\sigma_0/dP < 0$) while in the yellow shaded regions $d\sigma_0/dP > 0$. The insets zoom in the low-pressure region. The data was measured at pump fluence of 3 mJ/cm². Reprinted by permission from Springer Nature: [122].

vergence in $\sigma_2(\omega)$. Thus, pressure presents itself as a meaningful marker for the distinction between a metallic and a superconducting state.

Cantaluppi et al. encapsulated powder samples of K_3C_{60} in a diamond anvil cell, which allowed to apply the hydrostatic pressure from zero up to 2.5 GPa while performing equilibrium optical- and transient THz time-domain spectroscopy (THz-TDS).
Remarkably, the measured complex optical conductivity of K_3C_{60} in the equilibrium state showed the expected metallic pressure dependence (cf. red curves in Fig. 3.5) while the light induced state at five times T_c ($T = 100$ K) featured the pressure dependence of a superconductor [122]. This behavior was further analyzed by performing Drude-Lorentz fits to the optical conductivity (cf. Appendix D.2) and extrapolation to low frequencies to obtain a pressure dependent value for the DC optical conductivity $\sigma_0 = \lim_{\omega \to 0} \sigma_1(\omega)$. This value is plotted in Fig. 3.6 vs. external pressure for the equilibrium case (red squares) and the photo-excited case (blue diamonds). The three panels **a** - **c** show measurements at different temperatures above T_c at 100 K, 200 K and at room temperature. This data shows, that the equilibrium metallic conductivity increases with applied pressure ($d\sigma_0/dP > 0$) as is expected for a metal.

In contrast, the perfect conductivity of the light induced state is strongly reduced already for small applied pressures ($d\sigma_0/dP < 0$). This observation is in line with what is expected for a superconducting state. At higher pressures, once the photo-excited state ceases to show superconducting-like optical properties, σ_0 becomes finite and features a $d\sigma_0/dP > 0$ behavior similar to the equilibrium metal.
Surprisingly, for all temperatures up to 300 K the photo-excited state shows a low pressure regime where $d\sigma_0/dP < 0$, indicating that some features of transient superconductivity may already be present at room temperature.

3.3 Summary

This chapter presented an overview of the experimental evidence of a light-induced state with superconducting-like properties in K_3C_{60} far above the equilibrium critical temperature. Due to the fast decay of this transient state within few picoseconds, all measurements were limited to ultrafast optical time-domain spectroscopy. Although the observed signatures in the complex optical conductivity are reminiscent of a superconducting state, and the pressure dependence supports this interpretation, the concept and implications of a superconductor with such a short lifetime are unclear.
Superconductivity intrinsically is a property defined at DC-frequency. In an ideal superconductor there is no dissipation of the paired carriers resulting in an infinite scattering time. If, in contrast, the superconducting state decays back into a metallic one within a time constant τ, this has to be reflected in the low frequency properties of the material. Figure 3.7 shows the resulting implications on the complex optical conductivity. For frequencies smaller than $1/\tau$, the superconducting optical properties show a transition to the metallic behavior (indicated by the blue curve blending into red).
On the other hand, in a metal with high mobility its low scattering rate is reflected in a narrow drude peak and a corresponding incipient increase in $\sigma_2(\omega)$, which finally ceases towards low frequencies. This can result in very similar optical properties as shown in the two-color curve in Fig. 3.7. Thus, it is difficult to distinguish between a finite-lifetime superconductor and a metal with high mobility when looking only at the optical properties.

A state-lifetime of $\tau \sim 2$ ps (cf. Fig. 3.4 a) corresponds to a characteristic frequency of ~0.5 THz, which was also the lowest frequency we could access with our terahertz probe sources (THz light was generated from a femtosecond laser beam by excitation of a photo-conductive antenna or

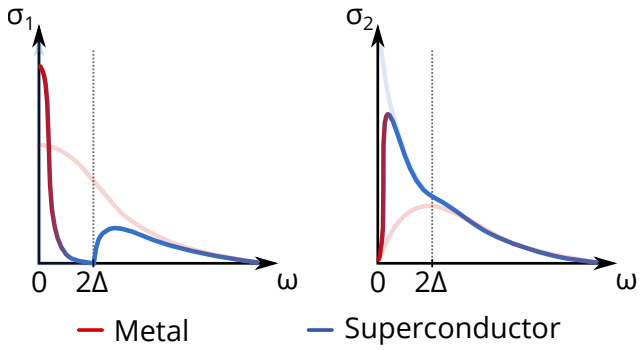

FIGURE 3.7: OPTICAL PROPERTIES OF A SUPERCONDUCTOR WITH FINITE LIFETIME.
Superconducting contributions to the graph are displayed in blue while metallic ones are shown in red. For frequencies smaller than the inverse of the decay time of the superconducting state, the optical properties must maintain a metallic behavior. Thus, for low frequencies in $\sigma(\omega)$ a narrow Drude peak is formed out of the gapped state and the divergence in $\sigma(\omega)$ turns into a convergence to zero.

optical rectification in nonlinear crystals such as ZnTe or GaP. More details on this can be found in Appendix B.3). In order to gain more insight into the nature of the light-induced state and in particular to better understand its low-frequency properties, an increase in its lifetime was essential. In addition, this would allow the use of non-optical measurement techniques such as electronic transport and magnetic susceptibility, which are of inherent interest in the context of superconductivity. A high mobility metal would not exhibit the characteristics of a vanishing electrical resistance at low-frequencies combined with perfect diamagnetism. Therefore, such measurements would provide clear evidence for or against the superconducting nature of the light-induced state.
The main focus of this work is to extend the lifetime of the light-induced state, which would render such experiments possible.

An intuitive approach to achieving a longer lifetime of the superconducting state is shown schematically in Fig. 3.8. All pump-probe experiments on K_3C_{60} described so far were using excitation pulse lengths of about 100 fs. Thus, one could think of using much longer excitation pulses that could coherently stabilize the system in its excited state - possibly even stabilizing it for longer than the time of the drive. This approach sounds simple, but an order of magnitude higher laser power is required to generate an order of magnitude longer laser pulses if the electric field is to be maintained.

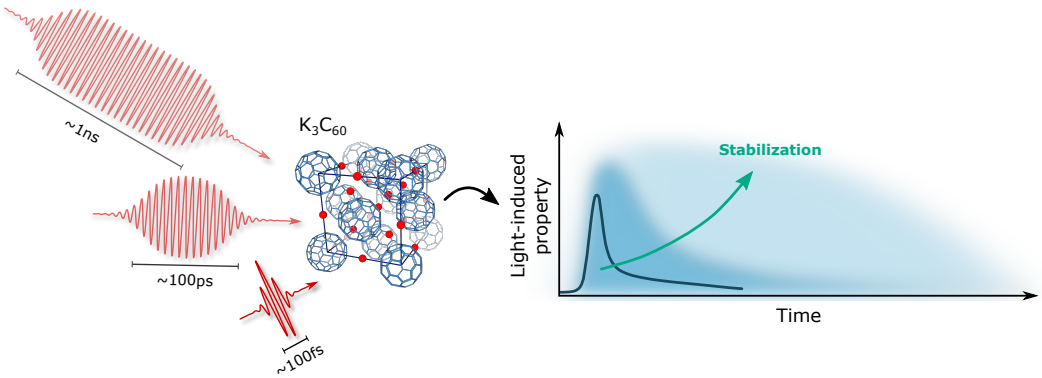

Figure 3.8: Vision on stabilization of light-induced properties via excitation with longer pulses.
The main focus of this work is based on the idea that an excitation with longer pulses of light might facilitate a longer lifetime of the resulting state.

4 Generation of High Power, Tunable, Mid-Infrared Light Pulses

In the last chapter we have shown that a longer lifetime of the light-induced state is essential to enable the use of non-optical measurement techniques, which can provide valuable information on the physics of superconducting states. In this work we want to investigate the influence of significantly longer excitation pulses on light-induced states and whether their lifetime can be extended.
For this reason, this chapter focuses on the development of a laser system capable of exciting samples with much longer yet intense pulses of mid-infrared radiation synchronized with a femtosecond probe laser.

4.1 Light Sources in the Mid-Infrared

Typically, the region of the electromagnetic spectrum called mid-infrared is denoted to a range of wavelengths from 2.5 µm to 30 µm. This spectral region is particularly interesting for spectroscopic applications, since the vibrational energies of most molecules fall in the mid-infrared, thus forming a "molecular fingerprint". Therefore, considerable efforts have been made to develop suitable light sources in this energy range for pulsed as well as cw-applications. Figure 4.1 shows an overview of the available laser sources in this range and their bandwidth.
Lasers with paramagnetic ions (e.g. the lanthanides Er^{3+}, Nd^{3+}, Tm^{3+}, Ho^{3+}, ...) embedded in crystals (such as YAG, YSGG, Sapphire), glasses or fibers, depending on their exact composition, can operate from the visible up to wavelengths of about 4 µm [139]. Similar wavelength regimes can be achieved by color center lasers with point defects in alkali halide and oxide crystals as the optically active medium.
In semiconductor lasers, electrons and holes recombine at the diode's junction resulting in emission of photons. Here, the materials (direct) bandgap determines the output wavelength. Thus, III-V compound lasers

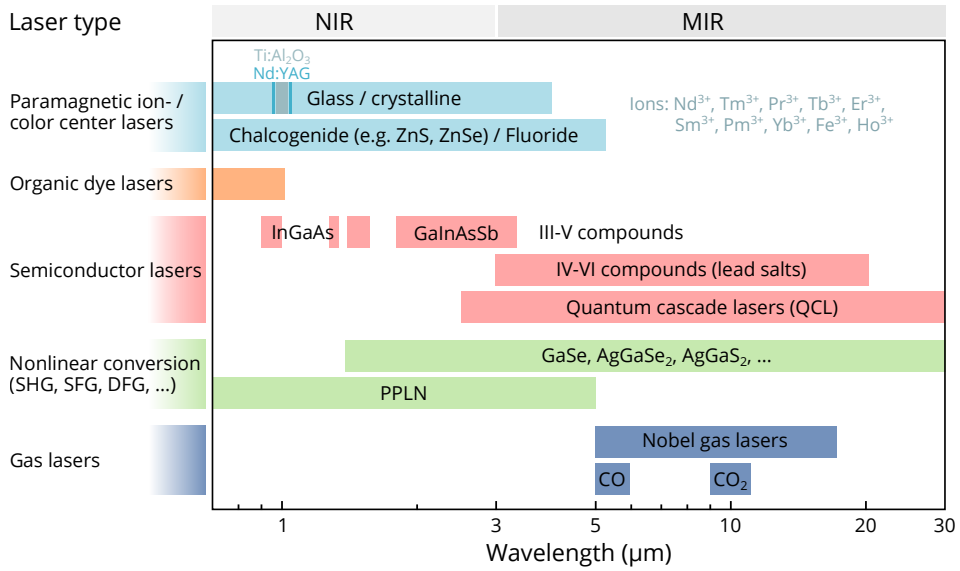

Figure 4.1: Lasers in the infrared
The type of laser is color-coded while the wavelength coverage is shown as horizontal bars. The named materials are exemplary and make no claim to completeness. Data for this figure was obtained from [139–143]

emit from visible to mid-infrared (e.g. InGaN: 405 nm, GaInP: 650 nm, InGaAs: 980 nm, GaInAsSb: 1.8 – 3.3 µm) while even longer wavelengths can be achieved with combinations of the IV-VI elements. These so called "lead salt" lasers cover a wavelength range from below 3 µm to more than 20 µm which would make them a potential candidate for excitation of K_3C_{60}, if their emission were not limited to several milliwatts per ampere of drive current [144] while careful cryogenic temperature control is necessary. This technology has therefore been replaced by the quantum cascade laser (QCL) after its first physical implementation in 1994 [145]. It is based on quantum well heterostructures that are formed by periodic layers of thin semiconducting films. The varying electric potential across the device results in a band splitting into discrete electronic subbands that can be designed to achieve the necessary population inversion. When applying a voltage, electrons follow the resulting potential staircase and emit photons at each step.

Unlike for diode lasers, the emission wavelength does not mainly depend on the materials band gap but rather on the geometry of the super-lattice, which can be adjusted in the manufacturing process. This allows a wide tunability from few to hundreds of micrometers in wavelength. Typical output powers of commercially available QCLs reach the regime of several watts, which is good enough for many spectroscopy applications but still too little for nonlinear optical processes. To reach the required field strengths on the order of several MV/cm for a beam diameter of 500 µm

that is compatible with THz spectroscopy, a continuous wave laser would need about three orders of magnitude more power (~ 1 kW). This would correspond to a peak intensity of about 5 GW/cm², but the continuous high power irradiation would certainly lead to a thermal destruction of any sample. Therefore only pulsed lasers with high peak intensity can reach this excitation regime while preventing excessive heat transfer.

A different approach for the generation of mid-infrared radiation with broad tunability and high power is frequency conversion in a nonlinear optical material. This takes advantage of the dielectric polarization P, induced by the electric field of the incident light. For high external fields, not only the linear term $P_{lin} = \epsilon_0 \chi^{(1)} E$ but also nonlinear terms in the form $P_{nl} = \epsilon_0 \sum_{n=2}^{\infty} \chi^{(n)} E^n$ have to be considered. Here ϵ_0 is the free space permittivity and $\chi^{(n)}$ is the n^{th} order susceptibility tensor. These nonlinear terms result in a multitude of conversion processes such as second harmonic generation (SHG), sum- and difference-frequency generation (SFG, DFG) as well as optical parametric amplification [146].
Femtosecond mid-infrared pulses with pulse energies of more than 50 µJ in 100 fs can be obtained via optical parametric amplification of two near infrared beams generated from optical parametric amplification of a white light continuum and their subsequent difference frequency generation. This approach was used in the earlier experiments on K_3C_{60} (cf. Section 3.2) and is particularly useful for the generation of sub-picosecond pulses. In the scope of this work, we could obtain a longer pulse length by introducing a frequency chirp by propagating these femtosecond pulses through a dispersive material. A schematic of the experimental setup is shown in Fig. 5.1, the related experiments are discussed in Section 5.1 and further details on optical parametric amplification can be found in Appendix B.2.
Although this stretching of femtosecond mid-infrared pulses is a valuable tool to extend the pulse length, it comes at the expense of peak intensity. Since our experiments rely on high electric field strengths, this effectively limits the pulse-width tunability to few picoseconds.

There is yet another laser technology operating in the mid-infrared not being discussed so far: Gas lasers. In the wavelength region of interest there are in particular nobel gas lasers ($\lambda = 5-17$ µm with pulse energy below 1 µJ) [147], the carbon monoxide laser ($\lambda = 5-6$ µm) as well as the CO_2 laser ($\lambda = 9-11$ µm with central wavelength at $\lambda = 10.6$ µm). The latter is a well established laser technology that is capable of producing very high output power ranging from several Watts up to Megawatts due to the good electrical to optical power efficiency from 5 % to more than 20 %. For this reason it is widely used in industry for cutting, engraving, welding and similar tasks.

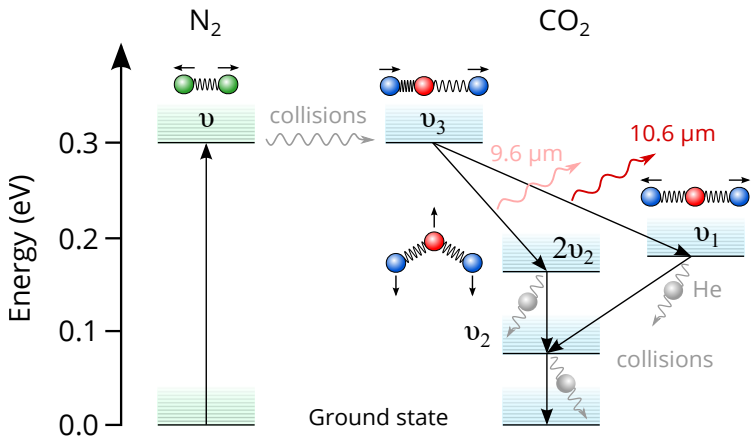

Figure 4.2: Energy levels of a CO_2 laser.
The laser medium is a mixture of CO_2, N_2 and He. Energy is at first transferred into vibrations of N_2 molecules. Since the vibrational energy level of N_2 is very similar to one of asymmetrical stretching of CO_2, energy can be transmitted via collisions. This mode radiatively decays into symmetric streching by emitting 10.6 µm light or into the bending mode by emitting 9.6 µm. Afterwards the carbon dioxide molecules transition in to their vibrational ground state by collision with cold helium atoms. Each of the discrete vibrational energy levels is composed of many vibration/rotation transitions with ~ 55 GHz spacing and line width of ~ 3.7 GHz [148] as indicated by the lines in light grey.

The CO_2 laser is using a 3-level system based on the vibrational energy states of the molecules. Usually, besides CO_2, other components such as N_2 and He are part of the laser gas to increase efficiency and reliability. Figure 4.2 displays the energy transition diagram of this laser.
N_2 molecules are excited e.g. by electrical discharge and collide with CO_2 molecules whose asymmetric stretching vibrational mode has a matching energy level. Stimulated emission at $\lambda = 10.6\,\mu m$ can now occur between the energy levels ν_3 and ν_1. The He atoms not only help in relaxing CO_2 into its ground state but also improve the thermal conductivity of the gas mixture thus counteracting the degradation of population inversion by heating.
Furthermore, besides the strongest emission line at 10.6 µm wavelength there is another weaker laser line around 9.6 µm and the discrete vibrational modes are extended by many more vibration/rotation transitions.

Since the CO_2 laser is a high-power laser operating in the MIR region, which is of interest for the excitation of K_3C_{60} and since it is a proven and widely commercially available technology, we have used this laser as the basis for

the development of a pulse length tunable pump source, which is described in the next sections.

4.2 Stabilization and Synchronization of CO_2 Gas Lasers

We used a commercial transversely excited atmospheric (TEA) CO_2 laser[1] with average output power of 60 W, tunable repetition rate up to 150 Hz and a specified pulse energy of 400 mJ. The laser cavity consisted of a semi-transparent focusing front optic (80 % reflectivity, focal length = 20 m) made of ZnSe and a grating reflector that allows the selection of a specific vibration/rotation transition around the central line at 10.6 µm by adjustment of its angle.
Since we wanted to use the output of this laser in a long pulse pump-probe type experiment the following requirements applied:

- the output fluence had to reach on the order of several µJ/ps to enable a field strength of several MV/cm for a beam diameter of 500 µm for pulse lengths beyond several picoseconds.
- the laser had to be stable in output peak intensity by few percent to allow efficient long term averaging of experiments.
- the timing jitter of successive pulses had to be better than 1 ps to connect to previous short pulse experiments
- the CO_2 laser had to be synchronized to a femtosecond laser used for probing and gating

A typical output profile of the CO_2 laser is shown in Fig. 4.3 a. It was measured with a fast photon drag detector[2] with a rise time of ~ 1 ns. It reveals the typical multi-mode operation of amplified spontaneous emission (ASE) being ejected through the semi-transparent front window of the laser. After plasma excitation of the laser gas, as soon as population inversion (gain)

1 Light Machinery IMPACT-4000
2 Hamamatsu B749; Input photons can not only promote electrons to a higher valence band but also transfer momentum to the carriers in a semiconductor (here: germanium). Thus, the absorption of many photons leads to a observable electric current which is the measured quantity of this detector [149, 150]

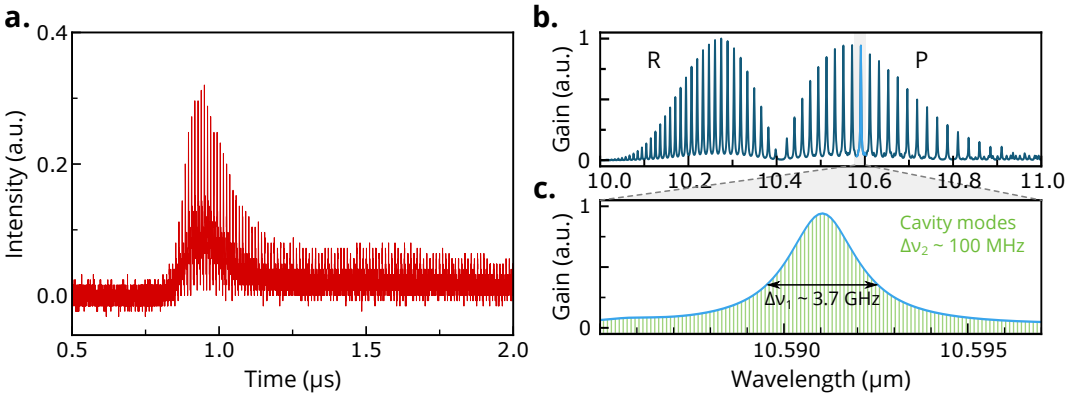

Figure 4.3: Amplified spontaneous emission of the CO_2 laser

a. Output intensity of our commercial CO_2 laser as measured with an electron drag detector displayed against time. The signal clearly shows the superposition of multiple excited longitudinal modes out of which the most intense displays distinct peaks of radiation with a repetition rate of ~ 10 ns which is corresponding to the length of the cavity of ~ 1.5 m. The pulse has an envelope of few microseconds. **b.** Calculated gain spectrum of molecular CO_2 at ambient pressure. Rotational transitions with a spacing of ~ 55 GHz form the R- and P-branches. The grating reflector within the cavity selects only one transition around 10.6 μm. **c.** The gain bandwidth of the selected rotational line is ~ 3.7 GHz which is much wider than the 100 MHz spacing of the longitudinal cavity modes. This results in arbitrary excitation of multiple modes when the laser is amplifying spontaneous emission.

is reached, the first photons that decay radiatively and stay in the resonator get amplified. Since spontaneous emission is a stochastic process, these photons have random phases and due to the small spacing of the longitudinal modes of ~ 100 MHz multiple of them can be excited within a single pulse (see Fig. 4.3 b, c). Moreover, the mode composition and their intensity can change from pulse to pulse leading to a fluctuating output in both intensity and time. This behavior does not match at all with the requirements formulated above and therefore significant improvements of the laser were needed.

One way to stabilize the output is to apply either passive or active mode-locking techniques. Passive mode-locking can be achieved by incorporating a saturable absorber such as SF_6 or Ge in the cavity, which is reducing the losses for the most intense pulse [151–153]. Thereby, single-longitudinal-mode or at least a mode-locked multi-mode operation can be obtained at the expense of some power loss in the absorber.
In contrast, for active mode-locking the resonator losses are typically periodically modulated by electro- or acousto-optic modulators [154, 155]. Both types of Q-switching facilitate the formation of reproducible high power out-

put pulses but the system is still lacking synchronization to the femtosecond probe beam.

Injection seeding is another technique commonly used to achieve a narrower optical bandwidth. In this case a light pulse with optical frequency close to resonance of a resonator mode is launched into the cavity just before the spontaneous emission would occur. As a result, this mode can oscillate at a much higher power than every competing mode and is dominating the output pulse avoiding mode-beating. Another significant advantage of this technique over other mode-locking options is the intrinsic synchronization of the output pulse to the seed pulse. Since for mid-infrared pump, THz probe experiments, the pump pulses generated by the CO_2 laser system had to be synchronized with the Ti:Al_2O_3 laser that generates the THz probe light, we decided to use this approach.

From a commercial Ti:Al_2O_3 regenerative amplifier, ~ 150 fs long, 10.6 µm wavelength pulses were generated by nonlinear conversion in a home build optical parametric amplifier (OPA) with subsequent difference frequency generation (DFG). A fraction of these femtosecond pulses (~ 60 pJ) were injected into the cavity of the CO_2 laser. These injected pulses with high bandwidth were spectrally filtered by the internal grating reflector, which is selecting only the desired frequency band around 10.6 µm. The injection of these seed pulses induces a temporal mode locking resulting in a train of output pulses, which are synchronized to the femtosecond seed laser [156]. A typical output trace is shown in Fig. 4.4 b (blue curve). The peak power of the pulse train is about an order of magnitude higher as compared to the non-seeded case (red curve) due to the phase locking of all longitudinal cavity modes induced by the seed. In addition, shot-to-shot reproducible mode coupling results in a reduction of the peak intensity fluctuations to less than 1 % being acceptable for our experiments. The remaining fluctuations are now due to small temporal variations of the electrically triggered plasma build-up, which translate into a jitter of the gain curve.

As depicted in Fig. 4.4 a, the seed injection has to be carefully tuned to about 550 ns after the plasma excitation is triggered. If the seed pulse is injected too early, there is no gain to amplify it and spontaneous emission will occur later. If the seed pulse is injected too late, it does not affect already amplified spontaneous emission anymore. Only when the seed is injected within the correct time-window of about 400 ns width with respect to the plasma discharge, a significant mode locking can be observed. At the optimal timing of seed injection, the pulse build-up time is reduced by ~ 150 ns as compared to ASE and the output intensity is highest. In this case the build-up time from injection to the maximum output pulse is about 1.35 µs.

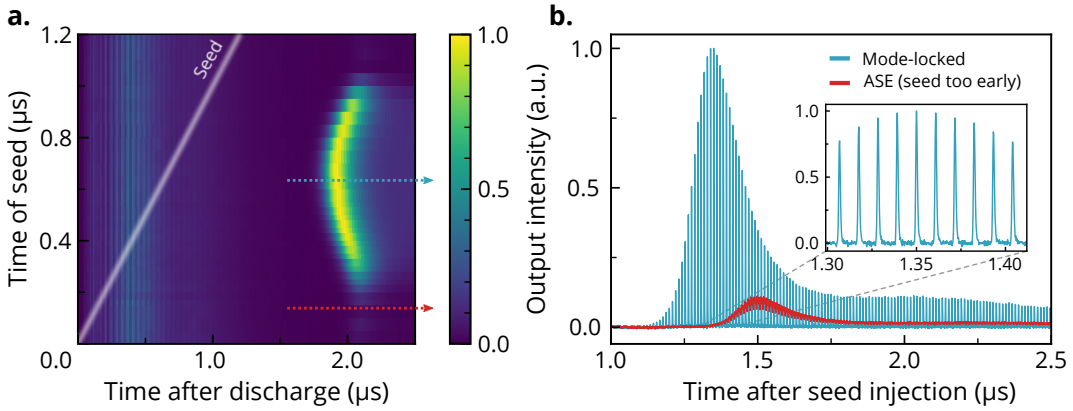

Figure 4.4: CO_2 laser injection seeding

a. Map of the CO_2 laser output traces vs. time of the injected seed pulse measured with an electron drag detector. The color indicates the output intensity. Both time axes are referenced to the trigger of the plasma discharge. The seed injection time is shown as a white line. The two dashed lines correspond to single time traces shown in b. **b.** Averaged output intensity time traces of the CO_2 laser are shown for the case of amplified spontaneous emission when the 100 fs long seed pulse is injected too early (red curve) as well as for optimal seeding (blue curve). The inset shows a section of a single-shot time trace of the seeded laser indicating perfect mode-locking.

The finesse of the CO_2 laser cavity in combination with the limited gain bandwidth does not support the high bandwidth of the femtosecond seed, which is resulting in pulses that are broadened to a width of ~ 1.3 ns. This is the upper pulse length limit of the source, which is four orders of magnitude longer than the pulses that were used in pump-probe experiments on K_3C_{60} before.

We used a custom-built CdTe pockels-cell to switch the single highest intensity pulse of the train from s-polarized to p-polarized. This allows a precise selection of the single highest peak by means of a wire grid polarizer.

So far the resulting mid-infrared pulses had a power of 13 mW at a repetition rate of 18 Hz (resulting in a fluence of about 730 µJ) and a pulse length of ~ 1.3 ns. They were stable in both intensity and time and were synchronized with a femtosecond laser. However, to extend the pulse length from the regime of previous pump-probe experiments, the pulses were now too long. The next section focuses on techniques for the generation of shorter laser pulses.

4.3 Generation of Ultrafast Pulses from Gas Lasers

To date, most pico- and femtosecond lasers work in the ultraviolet, visible or near infrared spectral region and they often take advantage of broadband gain materials. However, already in the 1970s strong efforts were made to shorten the pulse length of powerful gas lasers operating in the mid-infrared, which are suitable for a wide range of applications. Such pulses were of importance for the analysis of carrier dynamics in semiconductors, in photochemistry for the ultrafast spectroscopy of molecules and for research on nonlinear processes in general. Thus, there are various different approaches for the generation of sub-nanosecond CO_2 laser pulses.

4.3.1 Pressure Broadening

The amplification of short laser pulses requires a spectral gain with bandwidth broader than the Fourier-transform-limited spectrum of the pulse itself. For any molecular-gas laser the small-signal gain spectrum is composed of multiple periodic lines due to the allowed vibrational-rotational transitions of the CO_2 molecule (see Fig. 4.2). This periodic modulation of the gain reduces the overall gain bandwidth and thus hinders the amplification of picosecond pulses. Instead, a typical atmospheric CO_2 laser does not support the amplification of pulses shorter than ~ 1 ns.

By applying high pressure to the laser gas (typically 10 – 15 bar), collisional broadening of the spectrum by ~ 3.5 MHz/mbar [157] leads to a significant overlap of the individual lines facilitating the amplification of pulses with several picosecond duration [158, 159] (see Fig. 4.5).
Even shorter pulses can be achieved by enrichment of laser gas compounds with additional isotopes [160]. Polyanski et al. showed that a 50 % substitution of the naturally abundant ^{16}O with ^{18}O leads to a fourfold density increase of the rotational lines in the gain spectrum and thus 5 ps pulses could be amplified reaching 1 TW peak power.

Unfortunately, the application of high pressures would have not only required a complete re-design of the laser to facilitate the application of such high pressures but it is also changing the electrical discharge properties. Therefore tuning of voltage levels, electrode geometry and gas composition

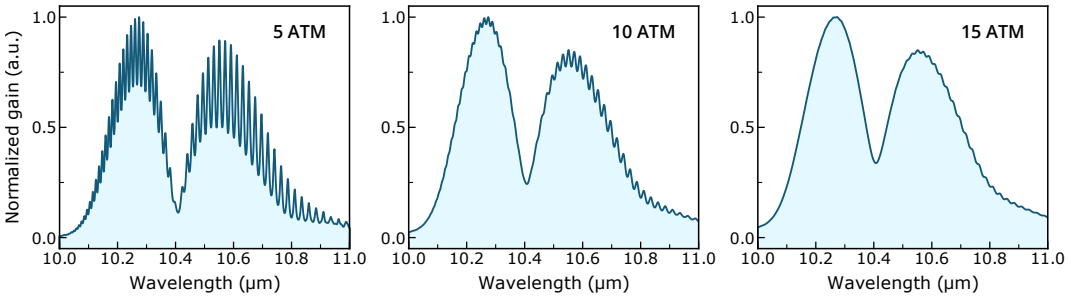

Figure 4.5: Gain spectra of pressurized molecular CO_2
The normalized gain of the rotational transitions was calculated for three different pressures. For ambient conditions refer to Fig. 4.3 b. The higher the pressure, the stronger is the line broadening which is resulting in a smoother gain curve. Calculations were performed using the HITRAN database [161].

would have been unavoidable to obtain a stable and homogeneous excitation [162]. The same argument and significantly higher costs for the laser gas applied to isotope substitution.

4.3.2 Field Broadening

To support the amplification of picosecond pulses, field broadening is an alternative approach to achieve higher bandwidth of the CO_2 molecular spectrum [148]. Due to the AC-Stark effect, the strong electric field of a laser pulse causes line broadening without the need for high pressures. Theoretically the only limitation of this broadening is the intensity of the laser pulse and the ionization threshold of the gas.
Apart from the fact that Stark broadening is a highly nonlinear effect, which might induce timing variations over the cross-section of the laser beam, extremely high field strengths are required. Haberberger et al. calculate that for an atmospheric amplifier peak intensities in excess of $5\,\mathrm{GW/cm^2}$ (corresponding to peak fields of $\sim 2\,\mathrm{MV/cm}$) are necessary to achieve a similar bandwidth as with a pressure broadened amplifier at 10 atm [148].

4.3.3 Optical Free Induction Decay

Another technique for the generation of short laser pulses is utilizing the fast growth of a plasma in a gas cell when high field strengths are applied. It has been shown that the breakdown spark can cause frequency shifts of $\sim 1\,\mathrm{cm^{-1}}$

of the transmitted beam and is able to cut the incident light in a time as short as 30 ps [163]. In combination with a spectral filter, which is able to reject the narrowband incident wavelength while the plasma induced side bands are transmitted, adjustable laser pulses in a range from 0.1 – 0.5 ns could be generated [164]. Here, hot CO_2 gas is used as a resonantly absorbing spectral filter attenuating the input beam heavily. Once the input wave is quenched by the plasma, the introduced molecular polarization of the gas will radiate until it is decayed. This optical free induction decay results in pulses with length on the order of the molecular collision time.
The output pulse length can be adjusted by changing the breakdown barrier with the pressure of the gas cell, which is a major advantage as compared to other techniques. However, the nonlinear process of plasma formation is strongly limiting its shot-to-shot stability which in turn is critical for the width of the generated spectrum. Moreover, in OFID experiments background suppression and post pulses are a relevant problem [165]. For this reason, we have looked at semiconductor switching as an alternative method with more controlled boundary conditions.

4.3.4 Semiconductor Switching

This approach is based on fast optical modulation of the free-carrier density in semiconductors with the aim of shaping their reflection and transmission properties for incident mid-infrared radiation. We decided to use this technique in our experiments because of many advantages over the other approaches discussed so far. Therefore, this section will go into more detail about the physics of semiconductor switching and our implementation in the experiment.

Figure 4.6 a shows a schematic of the applied switching geometry. Typically, a visible or NIR ultrafast laser pulse (the control pulse) is used to excite a plasma of electron-hole pairs within picoseconds in an optically flat semiconducting plate, which is normally transparent for MIR radiation. Thus, the induced high carrier density can drastically change the reflectivity of the semiconductor within the same time scale and was used in our experiments to slice CO_2 laser pulses.
A p-polarized mid-infrared laser pulse is transmitted through a semiconducting plate until an electron-hole plasma is excited in the material by the control pulse. The sudden high carrier concentration, which is confined within the laser absorption skin depth of several micrometers, turns the semiconductors surface metallic and acts like a switchable mirror. A com-

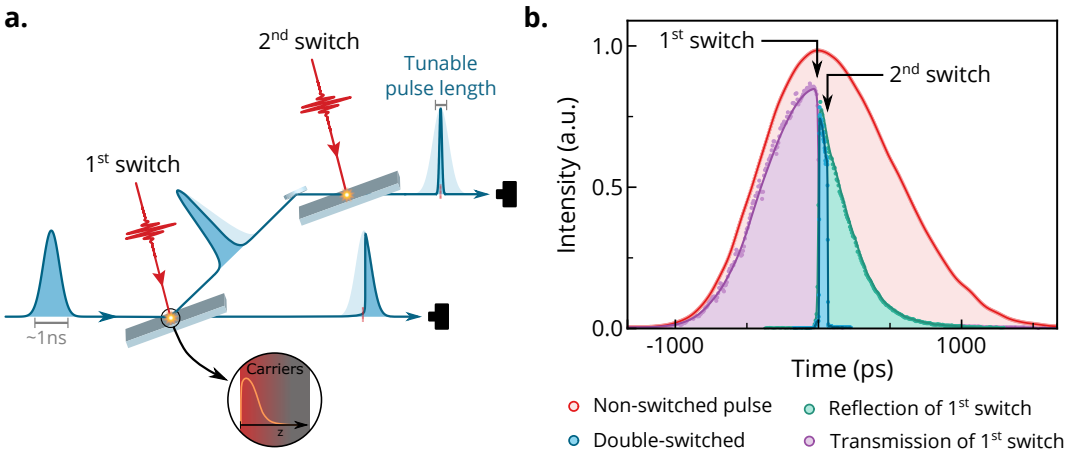

Figure 4.6: Principle of semiconductor switching

a. The schematic displays our setup for generation of continuously adjustable pulse lengths. The incoming MIR CO_2 laser pulse (blue) hits a semiconductor at Brewster's angle and its leading edge is fully transmitted. Now, a second short NIR pulse (800 nm wavelength, ~ 100 fs duration, red) excites an electron-hole plasma at spatio-temporal overlap with the MIR pulse. Within few picoseconds, the carrier density rises, which is turning the semiconductor highly reflective and slicing the MIR pulse. A subsequent switch can cut the trailing edge so that precise pulse length tunability is possible by adjusting the optical delay between the two NIR slicing pulses. **b.** Cross correlation curves of the unswitched (red) CO_2 laser beam and for single transmissive (violet), single reflective (green) and double switched (blue) cases. Upon switching, the semiconductor reflectivity changes within ~ 5 ps creating sharp edges in the pulse.

bination of a reflection and a transmission switch enables the generation of short pulses of variable length that can be adjusted by delaying the control pulses. The semiconducting plates are set at Brewster's angle to reduce reflections in the unswitched state and thus obtain a good signal to background ratio.
Figure 4.6 b displays time-traces of the resulting 10.6 μm pulses before and after switching. In this case the first switch was made from cadmium telluride and the second from silicon. These measurements were performed by cross-correlation of the mid-infrared pulse with an ultrafast NIR pulse (100 fs pulse length, $\lambda = 800$ nm) by means of sum-frequency generation in a 2 mm thick GaSe crystal.

Semiconductor plasma mirrors were first investigated by Alkock, Corkum and James in 1975 [166] and were afterwards applied in different laser systems both for external pulse shortening [159, 167] as well as for the reflection of a single pulse out of the laser cavity [168–170].
Due to the lack of other short pulse laser sources in the mid-infrared at that time, most research in the 70's in this field was focusing on the generation of sub-picosecond pulses. Pulse lengths as short as 130 fs could be generated by using multiple plasma shutters in combination with background suppression by narrowband filters [171]. Another approach for ultrafast pulse generation applies only one reflective switch while the semiconducting material is designed for a high intrinsic plasma decay rate. This causes the switch to be reflective only for a short time and to transmit again soon after the control pulse has ceased [172]. A comprehensive review of semiconductor switching is provided in [173].
For good mid-infrared transparency in the un-excited state, the semiconductors band gap energy E_g should be higher than the corresponding photon energy (117 meV for a CO_2 laser). However, to change the free-carrier density in the material by intense infrared control pulses, their photon energy (1.55 eV for wavelength of $\lambda = 800$ nm) is required to exceed the band-gap energy. Thus, photoexcitation from valence to conduction band can occur by interband absorption.
The critical carrier density for full reflection can be obtained from:

$$n_c^* = \frac{\epsilon_0 \epsilon_r m^* \omega^2}{e^2} \tag{4.1}$$

where ω is the infrared radiation frequency and ϵ_0, ϵ_r, m^* and e denote the vacuum and semiconductor dielectric constant, the effective carrier mass and the electron charge.
The stronger the excitation, the more the plasma frequency ω_p shifts to higher values until it exceeds the infrared (CO_2 laser) frequency. This

renders the refractive index imaginary so that the infrared beam can only exist inside the semiconductor as an evanescent wave, which corresponds to a high reflectivity in this frequency range. To switch CO_2 laser radiation at 10.6 µm, Equation 4.1 suggests that a critical carrier density of $10^{18} - 10^{19}\,\mathrm{cm}^{-3}$ is needed depending on the type of semiconductor.

For a description of semiconductor switching of infrared radiation by a photoinduced plasma one has to account for two processes:

1. The excitation and spatio-temporal development of an electron-hole plasma at the surface of a semiconductor

2. The reflection of an incident mid-infrared electric field pulse from this time- and space-dependent plasma density

The temporal and spatial distribution of the photoexcited electron-hole plasma in a semiconductor depends on various carrier dynamics and can be approximated by the one-dimensional continuity equation [174]:

$$\frac{\partial n_c(z,t)}{\partial t} - D\frac{\partial^2 n_c(z,t)}{\partial z^2} = G(z,t) - R(z,t) \tag{4.2}$$

Here, z is the spatial coordinate perpendicular to the semiconductor surface, D denotes the diffusion coefficient and $G(z,t)$ and $R(z,t)$ describe the rate of carrier generation and recombination, respectively. The temporal and spatial behavior of free carrier generation directly depends on the excitation pulse shape and its absorption. Because the excitation pulse and thus the plasma generation rate are on a very short timescale (~ 100 fs) for which diffusion and recombination can be ignored, we can consider this rate to be a delta function in time. According to Beer's law, a given excitation intensity at $t = 0$ results in a simplified plasma density profile of form

$$n_c(z, t = 0) = n_0 e^{-\gamma z} \tag{4.3}$$

where n_0 is the surface plasma density immediately after excitation and γ denotes the absorption length for radiation above the band gap. In semiconductors this penetration depth ranges between 10 nm and 10 µm for radiation above the band-gap and is therefore usually lower than the wavelength of the incident 10.6 µm light [175].
The recombination term in Equation 4.2 typically contains contributions from Auger recombination, radiative recombination, recombination via

phonons or impurities and surface recombination[3] and can be summarized by:

$$R(z,t) = -\Gamma_{aug} n_c^3 - \Gamma_{rad} n_c^2 - (\Gamma_{imp} + \Gamma_{surf}) n_c \tag{4.4}$$

Here, Γ denotes the respective recombination coefficients that determine the lifetime of the photo induced excess carriers.
It turns out that for early times after excitation $t < 1\,\text{ns}$ and plasma densities of several n_c^* both two- and three-body recombination processes are of minor influence due to their slower time scales. In contrast, diffusion is the most important mechanism dominating the decrease of plasma density already after few picoseconds [173, 175]. Note that D is the ambipolar diffusion coefficient describing a diffusion of electrons and holes at the same rate preventing charge separation.
Solving Equation 4.2 results in the temporal development of the free-carrier density spatial profile [174, 178, 179]. One example of such a solution for irradiation of silicon with an UV laser pulse is depicted in Fig. 4.7 a. As a result of carrier diffusion into the bulk, the surface plasma density is decaying. The timescale of this decay is usually in the range of picoseconds as shown in Fig. 4.7 b for a germanium sample irradiated with a 10 ps long pulse of 1.06 µm wavelength. With the surface plasma density also the mid-infrared reflectivity is changing - especially when n_c reaches values below the critical plasma density n_c^*.

To obtain the infrared reflectivity from a plasma density distribution one can model the dielectric function according to Drude's theory[4] and use a one-dimensional multilayer model for the propagation of a plane electromagnetic wave into this inhomogeneous medium[174].

The reflection and transmission properties of a large number of switching materials have been investigated, mostly with a focus on ultra-short carrier lifetime for ultrafast pulses, with Si, Ge, CdTe and GaAs being the most popular candidates. However, for experiments on K_3C_{60}, we were not interested in the generation of shortest possible pulses but rather in a good switching efficiency with wide tuning range from several to hundreds of picoseconds and a good background suppression. Since the temporal pulse profile as well as the slicing efficiency depend on the type of semiconductor and on the exact slicing geometry, we performed experiments to find the best material for our requirements.

3 Extensive information regarding all these recombination processes can be found in [176, 177].
4 The Drude theory is applicable if the band structure of the semiconductor is parabolic

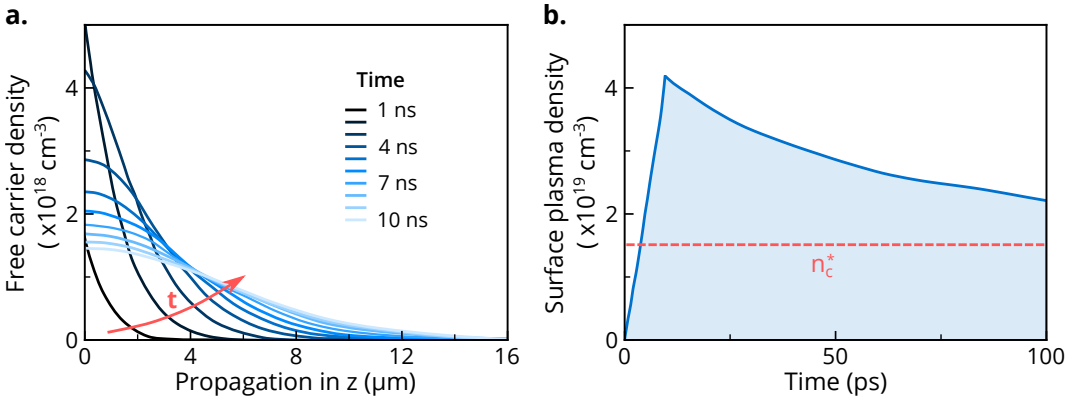

Figure 4.7: Spatial and temporal decay of the photo-excited plasma density
a. Time-dependent evolution of the carrier density profile upon irradiation of high resistivity silicon with a 1.7 ns long pulse of 337 nm wavelength and 470 µJ power. Figure adapted from [174]. **b.** Time trace of the surface density of free carriers in germanium after excitation with a 10 ps long pulse of 1.06 µm wavelength. The absorbed pulse energy was 1 mJ/cm². The dashed line indicates the critical carrier density for a reflection of 10.6 µm CO_2 laser radiation. Figure adapted from [175].

Figure 4.8 a shows a comparison of the time-dependent 10.6 µm reflectivity of a single semiconductor switch made of silicon, germanium and cadmium telluride, respectively. The curves were extracted from cross-correlations in a 2 mm thick GaSe crystal by calculating the ratio of the semiconductor reflection to the intensity of the unswitched beam, measured in the same cross-correlator. All switches reached a similar efficiency of about 50 %, which is in agreement with literature. Their damage thresholds were significantly different being just above 5 mJ/cm^2 for Si, 3.9 mJ/cm^2 for CdTe and only 1.7 mJ/cm^2 for Ge[5]. At these fluence levels maximum switching efficiency was achieved.
When comparing different materials, the decay rate of the reflectivity is very different and could be fitted with reasonable precision by a single exponential decay. This range of decay times results in varying applicability for each material. The short decay of 75 ps in CdTe is ideal for a reflection switch when only short pulses are needed. In this case it provides the best background suppression. However, for long pulses a Si reflection switch is optimal. Due to the long absorption depth, thick plasma layers are formed so that tunneling of radiation is negligible [171]. This makes silicon the best candidate for the second transmission switch for the generation of both short and long pulses. Since it is suppressing the trailing edge, this switch is most effective when radiation is blocked for as long as possible after photoexcita-

5 These values were achieved with a beam diameter of ~ 3 mm hitting the semiconductors at their respective Brewster's angle ($\Theta_{B,\mathrm{Si}} = 73.7°$, $\Theta_{B,\mathrm{CdTe}} = 69.5°$, $\Theta_{B,\mathrm{Ge}} = 76.0°$). This resulted in an elliptic spot size with half-axes of about 3 mm and 10 mm

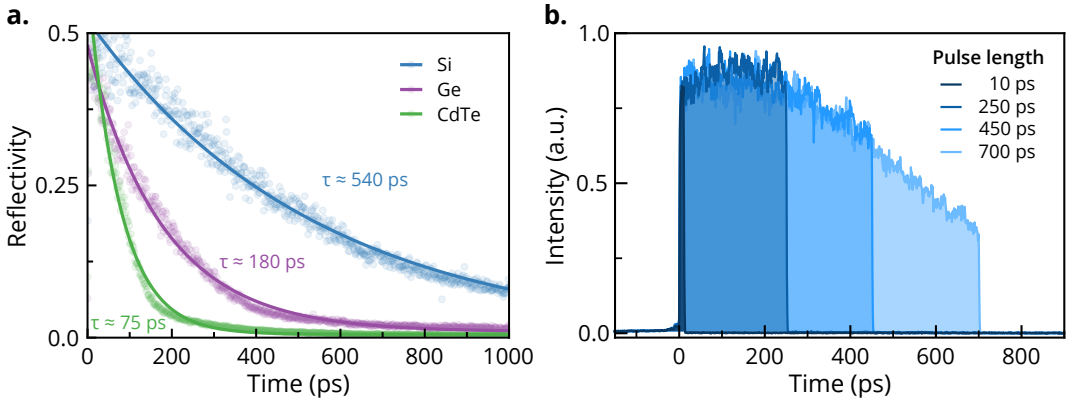

Figure 4.8: Time profile of semiconductor reflectivity and switched pulses
a. The temporal evolution of the reflected fraction of the incoming pulse is shown for three different slicing materials. Note that the power of the 800 nm control beam was adjusted before for every switch for maximum efficiency without damaging the material. **b.** Time profile of the 10.6 µm pulses after slicing on two silicon wafers in reflection and transmission. The traces are a result of a cross-correlation measurement following the procedure described in the text.

tion.
As described before, the rise time of the reflectivity depends on the carrier generation rate, which is mainly determined by the excitation pulse length. In our experiment, however, the flank rise time was the same for all tested switching materials and was on the order of 5 ps. This is not compatible with the much shorter 100 fs excitation pulses and is rather due to our specific measurement setup. Due to geometric constraints on the optical table, the mid-infrared and control-beam pulses arrive at the semiconductor at a slight angle. This results in an optical delay of few picoseconds across the illuminated area of the semiconductor which effectively broadens the slicing rise-time. Although a rise time of 5 ps was good enough for the planned experiments on K_3C_{60}, this effect could be adjusted with the spot size and the angle between the two beams. Further details on this can be found in Appendix B.1
Time profiles of double sliced pulses obtained with two silicon switches are depicted in Fig. 4.8 b. Here, the pulse length could be tuned over a wide range from ~ 5 ps to ~ 1 ns while over the first 300 ps almost flat-top pulses were achieved.

In summary, semiconductor slicing has the following advantages as compared to other short pulse generation techniques in the mid-infrared:

- The simple design requires only a semiconducting plate and a short laser pulse above its bandgap synchronized to the mid-infrared pulse.

- It has a high reflection efficiency ($> 40\,\%$) and signal to background ratio ($> 10^4 : 1$).

- Double switching enables the continuous adjustment of output pulses from ultra short ($< 1\,\mathrm{ps}$) up to $\sim 1\,\mathrm{ns}$ long pulses by means of an optical delay stage.

- Since the mid-infrared and the control pulse are synchronized in time, also the sliced output pulse is synchronized to it. This enables pump-probe type experiments.

4.4 Overview of the Experimental Setup

For the experiments on K_3C_{60} conducted within the scope of this thesis, we combined the techniques described in the last sections to form a unique laser source capable of producing high power, pulse length tunable pulses in the mid-infrared that are synchronized to a femtosecond laser. This way, the pump-induced changes of the sample could be monitored via time resolved THz spectroscopy. A schematic of the full setup is shown in Fig. 4.9.

Here, $\sim 150\,\mathrm{fs}$ long, $10.6\,\mu\mathrm{m}$ wavelength pulses were generated by difference frequency mixing of the signal and idler outputs of a home built OPA in a $1.5\,\mathrm{mm}$ thick GaSe crystal. The OPA was pumped with $\sim 100\,\mathrm{fs}$ long pulses from a commercial Ti:Al_2O_3 regenerative amplifier[6] ($800\,\mathrm{nm}$ wavelength).
A fraction of these femtosecond pulses ($\sim 60\,\mathrm{pJ}$) were injected through the semitransparent front window ($20\,\%$ transmission) into the cavity of a commercial transversely excited atmosphere (TEA) CO_2 laser. The injection of $10.6\,\mu\mathrm{m}$ wavelength seed pulses, induces a temporal mode locking resulting in a train of output pulses, which are synchronized to the femtosecond seed laser [156]. Because of the high finesse of the CO_2 laser oscillator cavity, the seed pulses were spectrally filtered and the oscillator produced pulses with nanosecond duration. The most intense pulse from the train was selected with a custom designed CdTe Pockels cell[7] and mid-infrared wire grid polarizers[8]. The resulting output consisted

6 Coherent Legend Elite, $5\,\mathrm{mJ}$ output power, $900\,\mathrm{Hz}$ repetition rate
7 The CdTe crystal and pockels cell driver were supplied by Bergman Messgeräte Entwicklung KG, This driver has the ability to switch from $0-10\,\mathrm{kV}$ within $3\,\mathrm{ns}$ with driver electronics synchronized to the Ti:Al_2O_3 seed oscillator
8 Thorlabs WP25M-IRC

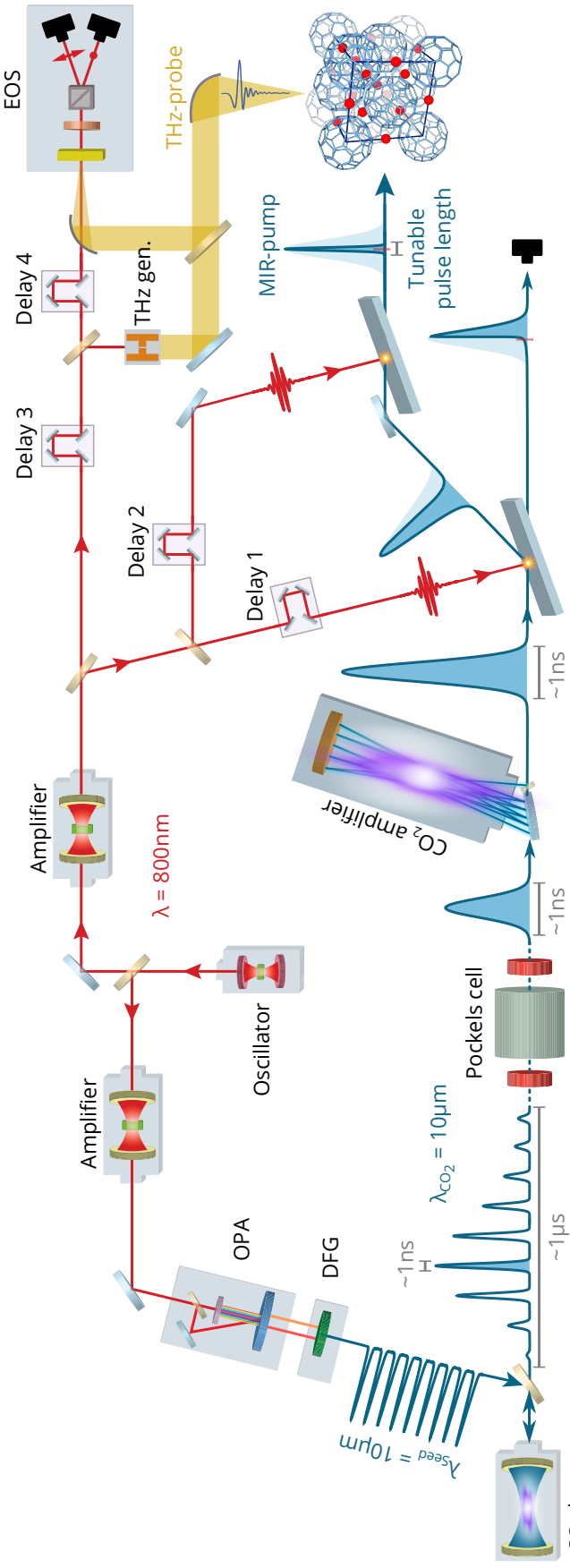

Figure 4.9: Experimental setup for THz-TDS with high power, tunable pulse length excitation

The source is capable of producing picosecond pulses of variable duration between 5 ps and 1.3 ns, centered at 10.6 µm wavelength, and with a pulse energy of up to 10 mJ. The pulses are generated by seeding a CO_2 gas laser with a femtosecond source. After amplification in a second CO_2 gas laser, their duration is tuned by semiconductor switching. The photoinduced changes in the optical response of K_3C_{60} upon irradiation are detected with transient THz time domain spectroscopy. Delay 1 and 2 can be used to adjust the timing of the control pulses and thus the CO_2 laser pulse length. Delay 3 can vary the excitation with respect to the THz probe and delay 4 is changed to scan the electric field of the reflected THz via electro-optic sampling. Further details of the setup are described in the text.

of a single pulse with a duration of ~ 1.3 ns and a pulse energy of ~ 730 μJ per pulse at 18 Hz repetition rate.

This pulse was then amplified further in a second ten-pass amplifier based on a modified commercial TEA CO_2 laser. The typical pulse energy achieved after the amplifier is ~ 11 mJ at 18 Hz repetition rate, with a pulse duration of ~ 1.3 ns.

The pulse duration of these 1.3 ns long pulses, was tuned using a combination of a plasma-mirror and -shutter, which allows slicing of the leading and trailing edge of the mid-infrared pulses. For both plasma slicers we utilized semiconductor wafers transparent to the 10.6 μm radiation (Si, Ge, or CdTe) set at the Brewster's angle to suppress the reflection of the p-polarized MIR beam. A pair of time-delayed, intense femtosecond pulses (λ = 800 nm, 100 fs duration) was used to photoexcite the semiconductors to create an electron hole plasma at the surface that acts as an ultra-fast switchable mirror [180, 181]. Varying the time delay between the two femtosecond pulses (via delay 1 and delay 2 in Fig. 4.9) enabled us to tune their pulse duration between 5 ps and 1.3 ns.

To compensate the path length in the cavities of the CO_2 laser and amplifier (~ 400 m), the slicing pulses were derived from a second Ti:Al_2O_3 amplifier. This was optically synchronized to the one used for generating the seed pulses for the CO_2 laser by seeding it with pulses from the same Ti:Al_2O_3 master oscillator. The envelope of the sliced mid-infrared pulses is affected by the decay time of the electron/hole plasma in the semiconductor. When using n-doped silicon, the long carrier recombination time yielded pulses that have an almost flat-top shape for different pulse lengths up to ~ 300 ps.

5 Extending the Lifetime of the Superconducting State

As described in Chapter 3, upon excitation with mid infrared light, K_3C_{60} shows superconducting-like optical properties far above the equilibrium critical temperature. However, due to the short lifetime of a few picoseconds, investigations of the transient light-induced state, have been limited to time resolved optical spectroscopies [122, 123]. Other methods, such as for example electronic transport measurements, simply lack the time resolution to observe these effects.

This chapter will discuss how excitation of K_3C_{60} with longer and more intense mid-infrared pulses induces a transient superconducting like state with a ~500 fold higher lifetime. Because of this, for the first time not only ultrafast THz spectroscopy was used to observe this state, but also electronic transport measurements with nanosecond electrical current pulses were perfomed. These experiments revealed a vanishingly small resistance of the photo-induced state which is compatible with superconductivity. Further experiments with different pump-pulse lengths and power levels reveal important implications on the nature of the mechanism that is supporting this state.

5.1 Excitation with Higher Fluence

As described earlier (cf. Section 4.1), nonlinear frequency conversion is a powerful technique to obtain ultrafast mid-infrared pulses. That's why as a first approach we modified the experimental setup based on optical parametric amplification and subsequent difference frequency generation that was used for previous photoexcitation experiments on K_3C_{60}.
We extended the pulse length of the resulting ~100 fs long and 7.3 μm wavelength pump pulses by applying a negative chirp via propagation in a transparent and highly dispersive CaF_2 rod. This resulted in a pulse duration of

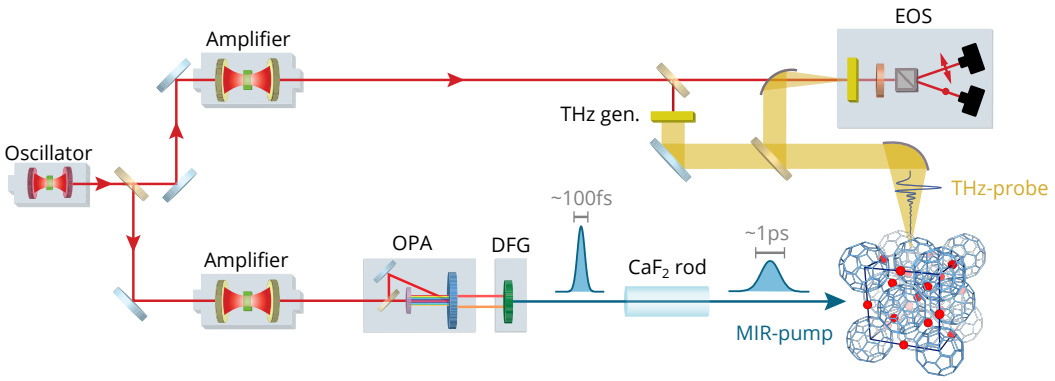

Figure 5.1: THz-TDS setup for high-power mid-infrared excitation with stretched pulses
The $\lambda = 800\,\text{nm}$ radiation of a Ti:Al_2O_3 regenerative amplifier is converted via OPA and subsequent DFG to obtain ~100 fs long, 7.3 µm wavelength pulses that were stretched in a highly dispersive 16 mm long CaF_2 rod to a pulse duration of ~1 ps. These pulses were used to photo-excite K_3C_{60}. Another Ti:Al_2O_3 amplifier seeded by the same oscillator was used for terahertz generation and detection (cf. Appendix B.3)

~1 ps, which enabled a sixfold increase in the pulse energy (up to 18 mJ/cm^2) before signs of sample damage could be observed. In contrast, earlier experiments with femtosecond pulses could not reach this new excitation regime at higher pulse power without damaging the sample. We measured the pump-induced changes in the complex optical conductivity of K_3C_{60} by means of THz-time-domain spectroscopy. Figure 5.1 displays the corresponding experimental setup. As in earlier experiments, THz-TDS measurements were performed on K_3C_{60} powders with average grain size of 100 – 500 nm that were compacted and sealed in a diamond anvil cell. Further details on sample preparation are given in Appendix A.

5.1.1 Transient Optical Properties

Representative spectra of the reflectivity $R(\omega)$ and complex optical conductivity $\sigma_1(\omega) + i\sigma_2(\omega)$ measured for K_3C_{60} at $T = 100\,\text{K}$ before (red), and after (blue) photoexcitation a three subsequent time delays of 10 ps, 300 ps and 12 ns are displayed in Fig. 5.2.

Remarkably, under these conditions all features that characterized the light-induced superconducting state namely a reflectivity saturated to $R = 1$, a gapped $\sigma_1(\omega)$, and divergent $\sigma_2(\omega)$ persisted up to at least 300 ps after excitation and relaxed nearly completely after 12 ns. Also in this case

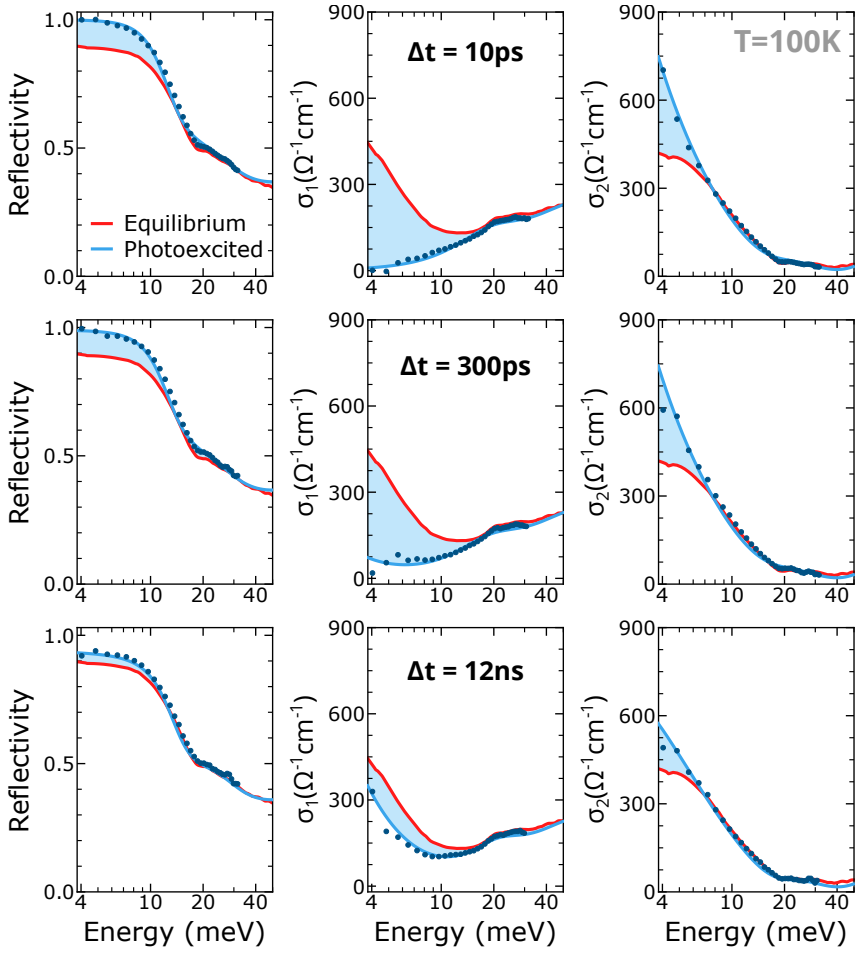

Figure 5.2: Long-lived light induced phase in K_3C_{60} after excitation with intense, 1 ps long pulses

Equilibrium reflectivity (sample-diamond interface), real, and imaginary part of the optical conductivity of K_3C_{60} measured at equilibrium (red lines), 10 ps, 300 ps and 12 ns (blue filled circles) after photoexcitation. The dark blue lines are Drude-Lorentz fits to the transient optical data (see Appendix D.2). These data were acquired at a base temperature $T = 100$ K with a fluence of 18 mJ/cm^2 and a pump-pulse duration of 1 ps.

the transient optical spectra could be fitted with a Drude-Lorentz model (blue lines) revealing a light-induced superconducting response up to 300 ps after photoexcitation.
Although this result is already a major increase of lifetime of the light-induced state, the experimental apparatus of Fig. 5.1 could not produce pulses longer than 1 ps with sufficient power to sustain this state. This was limiting the possibility to push the lifetime of the superconducting-like state even further. To overcome this limitation, we developed the CO_2-laser based mid-infrared source described in Section 4.4, that is capable of delivering high power pulses at 10.6 μm with an adjustable pulse length from 5 ps to 1 ns.

5.1.2 Temperature Dependence

The temperature dependence of the out-of-equilibrium optical response of the photo-induced superconducting state in K_3C_{60} is shown in Fig. 5.3. Therein, we report data measured at temperatures of 100 K, 200 K, and 300 K for increasing time delays of 10 ps, 100 ps, and 300 ps after photo-excitation with 1 ps long, 7.3 μm central wavelength pulses. The data acquired at 100 K is also shown in Fig. 5.2 of the last section.
At temperatures above 100 K, the light-induced gapping in $\sigma_1(\omega)$ is only partial and is significantly reduced as the temperature is increased. A similar behavior is also observed for the low-frequency divergence in $\sigma_2(\omega)$ that progressively vanishes upon heating. Interestingly, we note that for all measured temperatures the optical properties remained unchanged for 300 ps after excitation. This may suggest that precursors of the long-lived superconducting state discovered at 100 K are present all the way to room temperature.

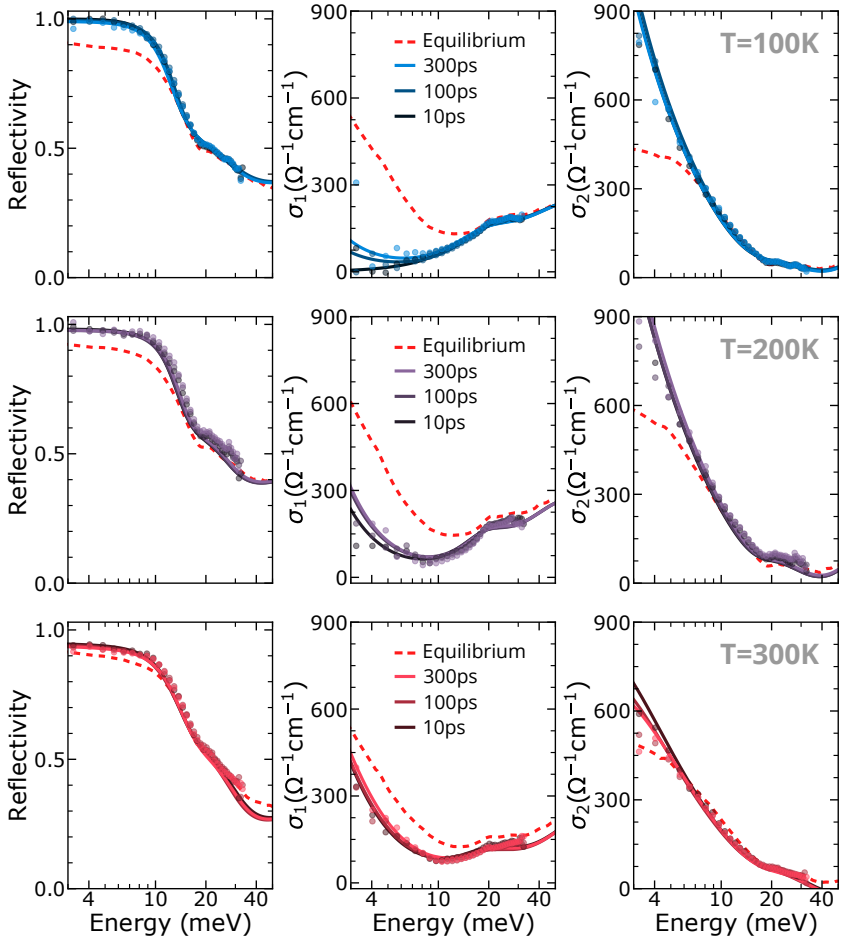

Figure 5.3: Temperature dependence of the light-induced optical properties. The measurements were performed at three different temperatures of 100 K, 200 K, and 300 K (upper middle and lower row, respectively). Each row displays reflectivity (sample-diamond interface), real, and imaginary part of the optical conductivity measured at equilibrium (dashed lines), and 10 ps, 100 ps, and 300 ps after photo-excitation (filled symbols). The solid lines are Drude-Lorentz fits to the transient optical data (cf. Appendix D.2). All measurements were performed using 1 ps long excitation pulses, centered at 7.3 µm wavelength, and with a fluence of 18 mJ/cm².

5.2 Excitation with Tunable Pulse Length

The following experiments were conducted by combining our pulse length tunable CO_2 laser source with a standard THz-TDS setup as it is shown in Fig. 4.9. The pump induced changes in the low frequency reflectivity and complex optical conductivity were reconstructed in the same way as before. The coupled Fresnel equations were solved for a material that was treated as a multi-layer of exponentially decreasing excitation and corresponding refractive index change (cf. Appendix D.1). All measurements were performed at 100 K, which is five times higher than the equilibrium critical temperature.

5.2.1 Transient Optical Properties

Figure 5.4 displays snapshots of the transient optical properties ($R(\omega)$, $\sigma_1(\omega)$, $\sigma_2(\omega)$) measured for K_3C_{60} at $T = 100$ K, before (red curves), 100 ps, and 1 ns after photoexcitation (blue symbols, top and bottom panels respectively) with a 300 ps long pulse centered at 10.6 µm wavelength. Strikingly, the transient optical spectra measured in these conditions show the same superconducting-like features as reported in Fig. 3.3 b and 5.2 for up to 1 ns after excitation. Here, the signal to noise ratio was reduced as compared to the short pulse experiments due to the low pump repetition rate of 18 Hz as compared to 500 Hz in the short pulse experiments.

5.2.2 Relaxation Dynamics

By changing the pump-probe delay, we also measured the time evolution of these features before, during and after photo-excitation. Figure 5.5 displays the resulting time traces of the average reflectivity in the region of the gap (cf. subfigure a) and of the average spectral weight in σ_1 (cf. subfigure b). Upon excitation, the average reflectivity is rising from its equilibrium value to one, while the real part of the optical conductivity is reaching zero, reflecting a full gapping. Both quantities remained unchanged within the measurement uncertainty for all time delays measured up to 1.2 ns.

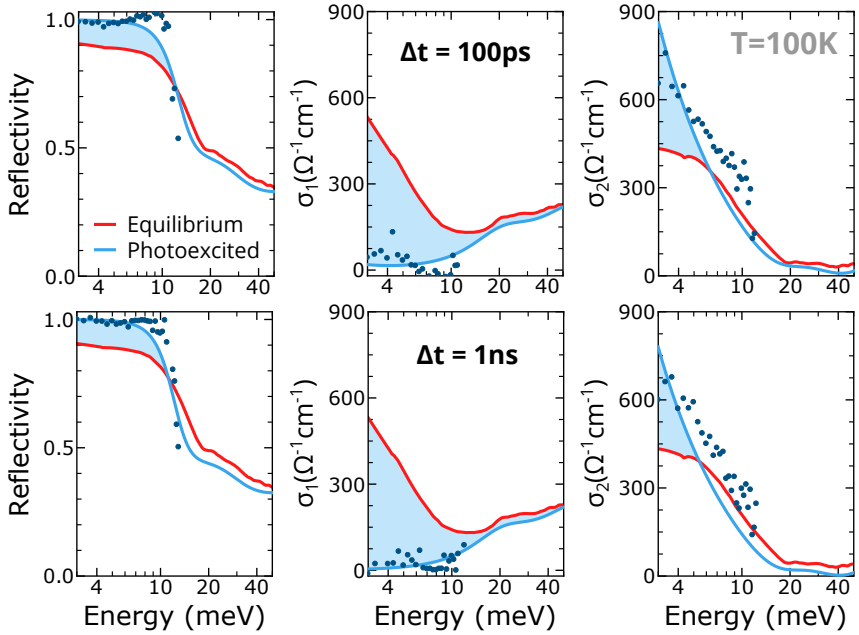

Figure 5.4: Long-lived light induced phase in K_3C_{60} after excitation with intense, 300 ps long pulses

Equilibrium reflectivity (sample-diamond interface), real, and imaginary part of the optical conductivity of K_3C_{60} measured at equilibrium (red lines), 100 ps and 1 ns (blue filled circles) after photoexcitation. The dark blue lines are Drude-Lorentz fits to the transient optical data (see Appendix D.2). These data were acquired at a base temperature $T = 100$ K with a fluence of 53 mJ/cm^2 and a pump-pulse duration of 300 ps.

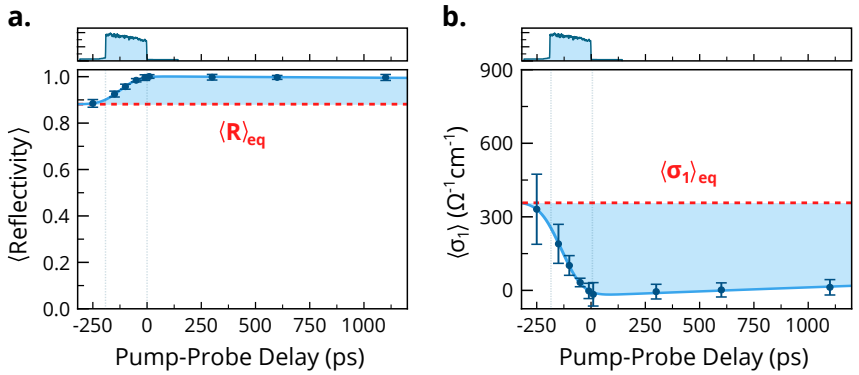

Figure 5.5: Time dependence of the light induced state in K_3C_{60}

a. Average reflectivity and **b.** spectral weight in the real part of the optical conductivity in the region of the photoinduced gap (2 – 10 meV). These data were acquired at a base temperature $T = 100$ K with a fluence of 25 mJ/cm^2 and a pump-pulse duration of 200 ps. The top panel shows the time profile of the excitation pulse measured by cross-correlation with a 100 fs long laser pulse.

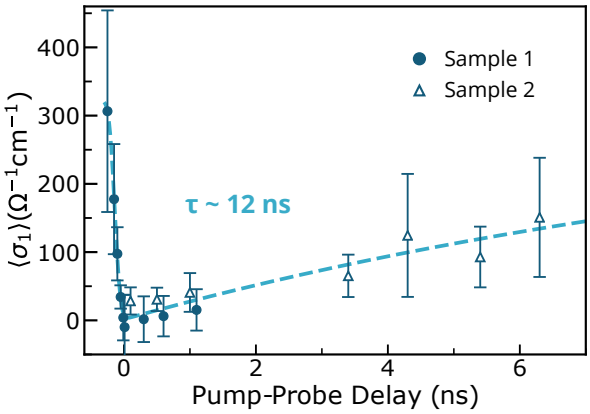

Figure 5.6: Decay of the light induced state on long timescales
Average spectral weight in the real part of the optical conductivity in the region of the photoinduced gap (2 – 10 meV) for different pump-probe delays measured on two different K_3C_{60} samples. These data were acquired at a base temperature $T = 100$ K with a fluence of 25 mJ/cm^2 and a pump-pulse duration of 200 ps. The dashed line is a fit to an error-function with subsequent exponential decay. The decay constant is about 12 ns. Error bars denote the standard deviation of the mean in the integrated frequency range.

To evaluate the relaxation dynamics of this metastable light induced effect, measurements with notably longer delays than supported by the longest optical translation stage in our setup were needed. Therefore, we added fixed retardations of about 1 m and 1.6 m into the probe beam path and extracted the data shown in Fig. 5.6. Again, the time-dependent mean value of σ_1 in the region between 2 meV and 10 meV is shown. By modeling the transient response exponentially, a decay constant of the fully gapped state after optical excitation of about 12 ns was revealed (cf. dashed line).

5.2.3 Pulse Length Dependence

The pulse length tunability of the CO_2 laser allowed us to extract the optical response of K_3C_{60} after different excitation durations. However, when extending the pulse length by semiconductor switching, the overall pulse power is increasing as well. In order to measure the true pump-pulse length dependency without influence of the total power, we accordingly attenuated the field using two polarizers. The upper panels in Fig. 5.7 show cross-correlations of such pulses with duration from 250 – 700 ps at constant pulse energy that resulted in a fluence of 22 mJ/cm^2 on the sample. The lower panels show corresponding data extracted from THz-TDS measurements. Here,

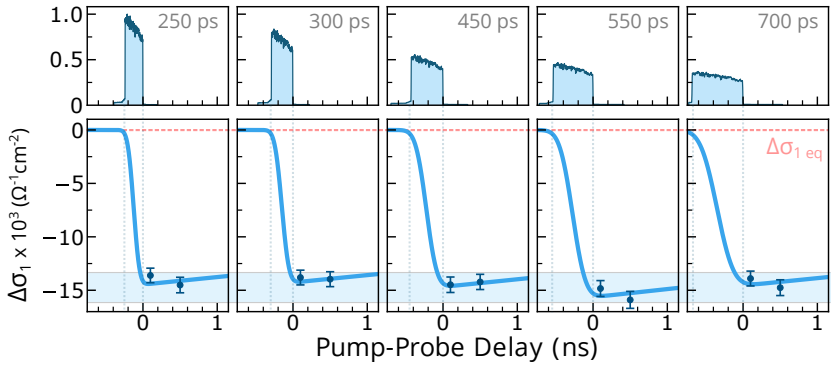

Figure 5.7: Dependence of the optical properties on the pump-pulse length
The lower panels show the photo-induced spectral weight loss $\Delta\sigma_1$ (as defined in Equation 5.1) measured for time delays of 100 ps and 500 ps after termination of the excitation pulse for different pump-pulse duration. The blue curves are a guide to the eye indicating the typical time dependence of the signal. A cross-correlation trace of the corresponding mid-infrared excitation pulse of each measurement is shown in the upper panels. The 10.6 µm pump was kept at a constant fluence of 22 mJ/cm^2 for all measurements and the base temperature was set to 100 K.

the reduction of spectral weight in the real part of the optical conductivity was calculated as

$$\Delta\sigma_1 = \int_{2.2\,\mathrm{meV}/\hbar}^{10\,\mathrm{meV}/\hbar} \sigma_1^{trans}(\omega) - \sigma_1^{eq}(\omega) d\omega \tag{5.1}$$

where $\sigma_1^{eq}(\omega)$ denotes the real part of the optical conductivity at equilibrium and σ_1^{trans} describes the corresponding values measured transiently after photoexcitation. For every pulse length $\Delta\sigma_1$ was measured 100 ps as well as 500 ps after excitation. The data indicate that, within the measurement accuracy, the photo-induced gap in the real part of the optical conductivity does not depend on the pump-pulse length and is also not influenced by the respective change of its maximum field amplitude. In this experiment pump-pulse lengths shorter than 250 ps were not measured since the fluence of 22 mJ/cm^2 could not be reached for these shorter pulses.

5.3 Electronic Transport on K_3C_{60}

An obvious parameter of interest in the context of superconductivity is the materials electrical resistance. For a superconductor at T_c the DC resistivity is dropping to zero and the current is carried exclusively by the supercon-

ducting phase while at finite frequencies also contributions of quasi-particles have to be taken into account. The frequency range accessible by state-of-the-art high speed electronics ranges into the GHz band which is corresponding to significantly slower time scales as compared to the picosecond relaxation times discussed in Section 3.2. In contrast, the nanosecond lifetime of the transient state upon excitation with longer and more intense light pulses, allowed us to reach the working range of standard electronic equipment and thus to measure the resistance of the sample directly.

5.3.1 Equilibrium Four-Probe Transport Measurements

Before trying to measure transient transport properties, we performed standard four-terminal resistance measurements on K_3C_{60} at equilibrium. Therefore, pressed pellets of powdered K_3C_{60} were incorporated into a sample carrier on patterned microstrip transmission lines (for details on sample praparation see Appendix E.1). The sample resistance was measured by a lock-in technique with sinusoidal excitation current of amplitude $I_{source} = 1\,\mu A$ at a frequency of 300 Hz. Figure 5.8 shows a typical temperature dependence of the materials resistance featuring the sharp superconducting phase transition at ~19 K. The width of this transition was always ~5 K for our samples. Very similar results on poly-crystalline thin films of K_3C_{60} were obtained before by Wang et al. and Palstra et al. [89, 93]. Like in our case, they report a negative temperature coefficient of the resistivity (TCR) above T_c which is a semiconductor-like behaviour. In contrast, for single crystals of K_3C_{60} several studies suggested a different, more metallic behavior with positive TCR [88, 91, 92, 182]. This difference in behaviour was attributed to the higher degree of disorder in the polycrystalline samples leading to a shorter mean-free-path and stronger correlations due to more localized electron-electron interactions [93, 183]. Further magnetotransport measurements suggested that more than the K_3C_{60} thin film granularity, microscopic disorder generated by doping inhomogeneity is influencing localization and thus electronic properties [89]. In summary, the normal state is understood as a weakly localized 3D metallic state with superconducting fluctuations just above T_c.

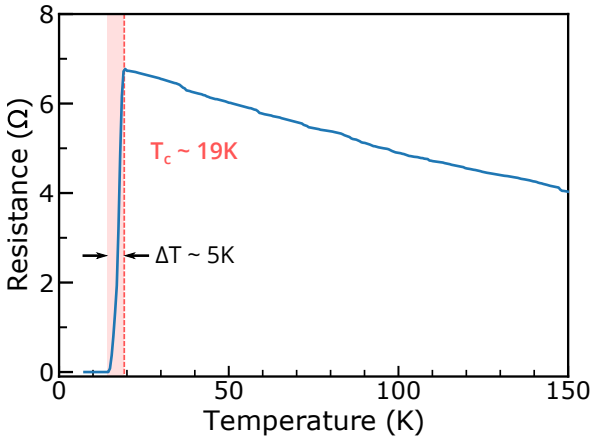

Figure 5.8: Temperature dependence of the K_3C_{60} resistance.
K_3C_{60} pellets that were incorporated in gold transmission lines were measured in a temperature controlled liquid helium cryostat. This data was measured in a four-terminal geometry to eliminate contact resistance.

5.3.2 Transient Time Resolved Transport Measurements

While the four-terminal resistance measurement described in the last section provides accurate values of the low frequency sample resistance R_{sample} it could only be applied up to frequencies of a few MHz due to the limited bandwidth of the high input impedance differential amplifiers that were necessary to measure the voltage drop without significant current flow as well as parasitic capacitances in the circuit. The lifetime of the light-induced superconducting state is several nanoseconds, hence four-terminal measurements are too slow to probe transport properties on these time scales. To overcome this issue, we performed high-frequency two-terminal resistance measurements where a homogeneous wave impedance can be obeyed at least approximately. Here, we tracked the resistance of the K_3C_{60} pellet at different times after excitation by transmitting a 1 ns voltage probe pulse and measuring its amplitude before and after the sample. This measurement mode is influenced by contact resistances which could be quantified and subtracted by comparing to the equilibrium four-terminal measurements described in the last section. Further details on the method are described in Appendix E.2 and E.3.

Figure 5.9 a shows the time evolution of the extracted K_3C_{60} sample resistance measured at $T = 100\,\mathrm{K}$ upon photoexcitation in similar conditions to those of the optical experiments reported in Section 5.2. Upon excitation, within the degree of uncertainty, the resistance drops to zero and slowly recovers only on a time scale of tens of nanoseconds.

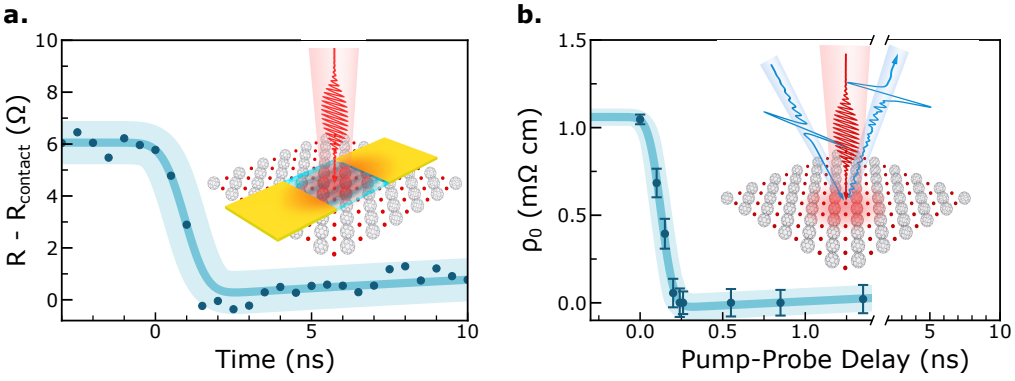

Figure 5.9: Transient resistivity measurements of the long-lived light-induced phase in K_3C_{60}.
a. Resistance of a laser irradiated K_3C_{60} pellet embedded in a microstrip transmission line. The resistance value is obtained from a transient two-point transport measurement where contributions of contact resistances are calibrated by a static four-point measurement. The shaded area indicates an estimate of the systematic error introduced by this calibration (see main text and Appendix E.2 for more details). **b.** Time evolution of the transient resistivity ρ_0 as obtained from an extrapolation to zero frequency of a Drude-Lorentz fit to the transient optical conductivities (cf. Appendix D.2). The insets display a schematic of the experimental geometry. These data were acquired at a base temperature $T = 100\,\mathrm{K}$ with a fluence of $25\,\mathrm{mJ/cm^2}$. The pump-pulse durations were 75 ps and 200 ps for the transport and optical measurements, respectively.

This quantity can be qualitatively compared with an estimate of the "zero-frequency resistivity" defined as

$$\rho_0 = \lim_{\omega \to 0} \frac{1}{\sigma_1(\omega)} \tag{5.2}$$

that was obtained by fitting a Drude-Lorentz model to the transient optical properties (for further details on the fitting see Appendix D.2). The values of ρ_0, extracted from the time dependent optical properties that were already used in Fig. 5.5 b, are shown in Fig. 5.9 b. Like the direct electrical resistivity measurement, this fitting procedure also suggests a vanishingly small $\rho_0(t)$ for all time delays after excitation.
In contrast, the timescales revealed by the two measurements are different due to differing time resolution of the two methods. In transient THz spectroscopy this is determined by the pulse length of the probe and gate pulses (~ 200 fs) while for electronic transport the length of the injected current pulse (~ 1 ns) limits the resolution. Despite this restriction, in transport it is much easier to implement an additional delay to measure the response of the system at long timescales. The full relaxation dynamics of the metastable state in K_3C_{60} measured by transport is depicted in Fig. 5.10. It turned out that a single exponential fit is not enough to capture the temporal progression back to the equilibrium. Rather a double exponential decay (light blue solid line) with a first time constant of $\tau_1 \approx 30$ ns and a second slower one of $\tau_2 \approx 550$ ns was necessary for a good fit. The fast decay is compatible

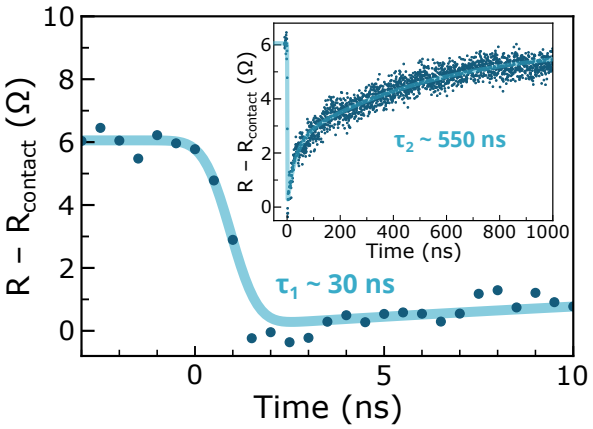

Figure 5.10: Timescales of the transient resistance of K_3C_{60} after photoexcitation
The graph displays the same data as in Fig. 5.9 a while the inset shows the relaxation dynamics of the signal on an extended timescale. The light blue solid line is a fit with a double exponential decay function featuring an early fast decay with $\tau_1 \approx 30$ ns and a second slower decay with $\tau_2 \approx 550$ ns. All measurements were performed at an excitation wavelength of 10.6 µm, and base temperature of $T = 100$ K.

with the order of magnitude that was measured optically before (cf. Fig. 5.6), while the long time scale was not accessible in THz-TDS.

5.3.3 Pulse Length and Fluence Dependence

Similar to the THz-TDS experiments shown in Section 5.2, we repeated the electrical probe experiments while varying excitation pulse duration and fluence. Figure 5.11 shows a color mesh plot of the calibrated K_3C_{60} pellet resistance which was extracted from two-terminal measurements as described in the last section. We used CdTe and Si as switching materials which resulted in pump pulses with good background suppression and maximum length of 100 ps. In contrast to optical measurements, where it is crucial to match the pump and probe beam sizes, in electronic transport the size of the excitation spot was matched to the electrode geometry on the K_3C_{60} pellet and the fluence was adjusted to similar maximum values as in the optical experiments. At higher fluence values the minimum achievable pulse length was higher, since the maximum power of our experimental setup was limited. The kink in the boundary of the measured values is caused by the decrease of the CdTe plasma level reflectivity.

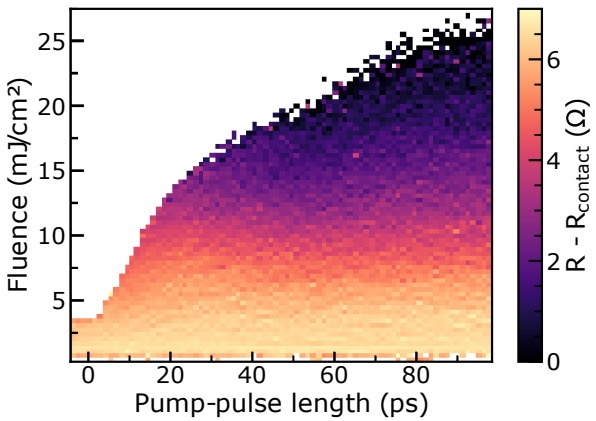

Figure 5.11: Map of the K_3C_{60} sample resistance vs. pump-pulse length and fluence

The resistance values displayed in color were extracted from two-terminal measurements that were calibrated by four-terminals as described in the text. The excitation pulses were shaped by semiconductor switching with CdTe and Si yielding a maximum pulse length of 100 ps at 10.6 µm wavelength in this experiment. All measurements were performed at a base temperature of $T = 100$ K.

The data suggests, that the resistance is diminishing with increasing fluence while there is no clear dependency on the excitation pulse length. Figure 5.12 a shows exemplary pump-pulse duration dependences of the measured sample photo resistivity for excitation fluences of 1.5 mJ/cm^2, 10 mJ/cm^2, and 25 mJ/cm^2 that were extracted from the same dataset. These results highlight that the photo-induced effect is mostly independent on the pump-pulse duration and rather depends on the total energy of the excitation pulse only. This is underscored by the data presented in Fig. 5.12 b, which illustrates the dependence of the sample resistance on the excitation pulse fluence. Beyond a range of intermediate fluences, where the resistance drop varies smoothly with the excitation pulse fluence, we observed the presence of a saturation threshold of ~ 20 mJ/cm^2. These observations are suggestive of a scenario where the mechanism does not dependent on the excitation peak field.

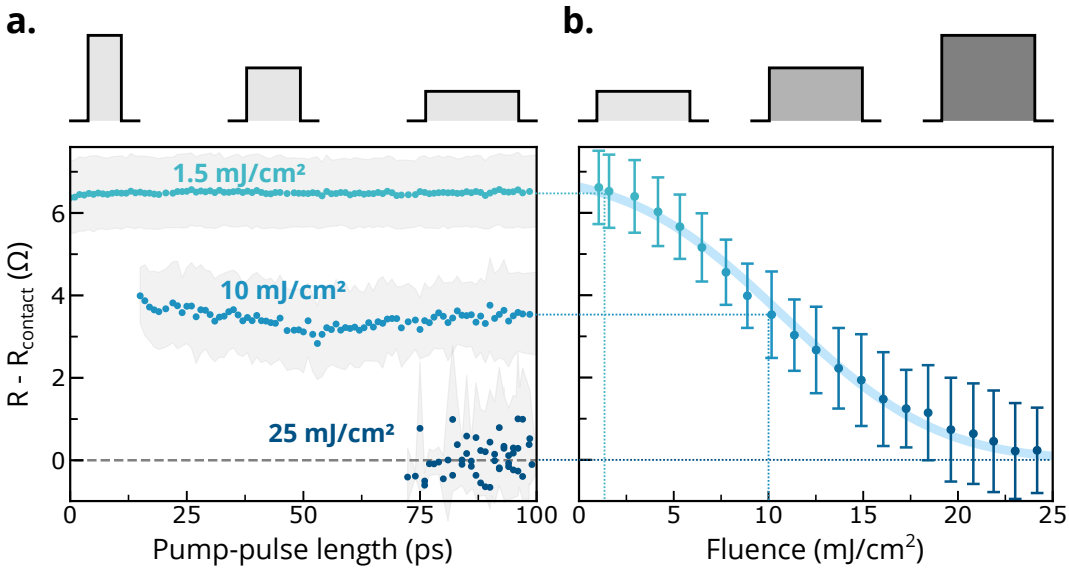

Figure 5.12: Pump-pulse duration and fluence dependence of the long-lived light-induced phase in K_3C_{60}

a. Pulse-length dependence of the resistance of a laser irradiated K_3C_{60} pellet measured at three different representative fluences of 1.5 mJ/cm^2, 10 mJ/cm^2, and 25 mJ/cm^2. For the higher fluence values of 10 mJ/cm^2 and 25 mJ/cm^2 the minimum achievable pulse length is higher due to limitations of our experimental setup. The shading represents the standard deviation of the measurements. The sample resistance was obtained as in Fig. 5.9 a by calibrating the contributions of contact resistance in the transient two-terminal measurement from a static four-point measurement (see Appendix E.2). **b.** Corresponding fluence dependence of the calibrated sample resistance measured at a constant pump-pulse duration of 95 ps. The solid line is a guide to the eye. The error bars display the standard deviation of the mean. These data were measured at a base temperature $T = 100$ K.

5.3.4 Temperature dependence

The light induced optical properties in K_3C_{60} have been measured earlier for different temperatures as published in [123]. Generally, superconducting-like optical properties could be induced above the critical temperature of ~ 19 K. In the region of the superconducting gap a complete gapping in $\sigma_1(\omega)$ a divergence in $\sigma_2(\omega)$ and a reflectivity of one was achievable up to ~ 100 K while for even higher temperatures all of these signatures of superconductivity were diminished.
In contrast, below T_c, the laser excitation led to an attenuation of the superconducting character of this material. This is a remarkable difference to other superconductors, e.g. the cuprates, where the excitation of vibrational modes led to a stiffening of superconductivity below T_c (see Section 1.2).

Here we explore the influence of the base temperature on the long lived light-induced state measured directly by electronic transport. As expected, both the absolute resistance of K_3C_{60} pellets as well as their contact resistance to the microstrip transmission lines were changing with temperature (cf. Section 5.3.1 and Appendix E.2). For this reason, Fig. 5.13 does not display absolute values but rather the change of the pellet resistance upon irradiation with 20 ps long 10.6 μm wavelength pulses for different temperatures across T_c. The resistance values were obtained as described briefly before and in detail in Appendix E.2 by calibration of two-terminal measurements with equilibrium four-probe measurements.
Most relevantly, the differential resistance showed a change in sign at about 17 K[1]. Below this temperature the resistivity of K_3C_{60} was reduced while at higher temperatures it was increased. This is in good agreement with the data measured by THz-TDS.
The time scales of the transient change of resistance above and below the critical temperature are rather different. Above T_c the effect is much shorter lived (on the order of several nanoseconds) than below. It is important to note that in contrast to the measurements with vanishing resistance shown earlier, here the excitation pulse length was shorter (20 ps) which also reduced the fluence to about 6 mJ/cm^2. This resulted in the much smaller maximum resistance drop of about 2 Ω. Furthermore, the measurable decay time of the light-induced state above T_c was reduced by this to less than 10 ns. Already at 50 K the transient response is slightly smaller than just above T_c. At even higher temperatures the effect was decreasing continuously.

1 The slightly smaller value of the transition temperature as compared with literature ($T_c \approx$ 19 K) might be due to a more inhomogeneous sample or temperature gradients between the cryostat measurement points and the sample.

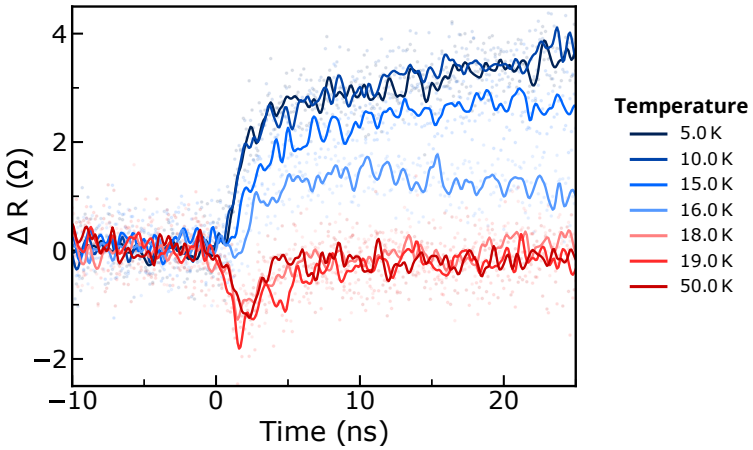

Figure 5.13: Temperature dependence of the transient light-induced resistance change of K_3C_{60} measured by electronic transport.
The excitation pulse length was 20 ps for all traces with the excitation starting at time zero. Blue colors indicate cold temperatures below the equilibrium superconducting transition, while higher temperatures are displayed in red. The line traces were obtained from raw data (weakly drawn points) by performing a sliding average binning to reduce the noise.

In contrast, below the critical temperature, where the material is in the superconducting state, the response changed sign, was stronger in magnitude and lived even longer. This is clearly an indication of destruction of superconductivity.
To obtain an estimate of the recovery rate of the superconducting state after its depletion by the pump, we measured the response on even longer time scales. The result is shown in Fig. 5.14 indicating a recovery rate in the tens of microseconds. These extremely long decay times (about three orders of magnitude longer than the nanosecond lifetime of the induced state above T_c) suggest a predominantly thermal effect. This is supported by the fact that with decreasing temperatures (e.g. 5 K trace in Fig. 5.14) the recovery time is shortening due to the increased cooling power.

In summary, the temperature dependence of the light induced effect obtained from THz-TDS could be reproduced in electronic transport. Below T_c heating of the sample seems to have a significant impact on microsecond timescales. Above T_c this effect appears to be rather negligible while enhancement effects could be observed on shorter, nanosecond timescales.
More measurements at higher fluence comparable to the experiments shown earlier (~ 25 mJ/cm^2) are needed to confirm this effect and to carefully map the dependence up to room temperature.

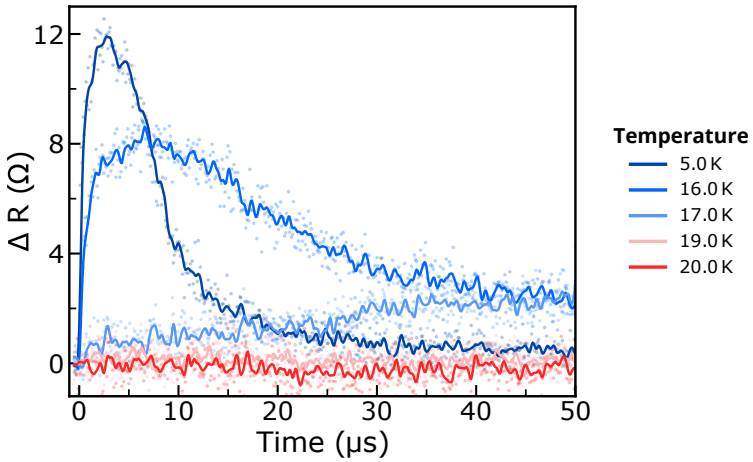

Figure 5.14: Temperature dependence of the transient light-induced resistance change on long time scales.
Colors are indicating the temperature above and below T_c as in Fig. 5.13. The K_3C_{60} pellet resistance was increased by the MIR pump and recovered within a time range of several tens of microseconds. Both the magnitude of the resistance enhancement and its decay rate back to the equilibrium state were increasing with a decrease of temperature.

5.4 Summary

With the data presented in this chapter we could show a significant life time extension of the transient photo-induced effects. This was achieved by excitation with longer and more intense mid-infrared light pulses. The optical properties of a superconductor, namely reflectivity of one, gapping in $\sigma_1(\omega)$ as well as $1/\omega$ divergence to low frequencies in $\sigma_2(\omega)$ could be observed by time resolved terahertz spectroscopy for several nanoseconds. This for the first time enabled direct electronic transport measurements that rely on such long life times.
Here, upon photo-excitation under similar experimental conditions, we observed a drop of the sample resistance that is compatible with a superconducting transition to zero resistance. It turned out that the materials properties obtained by both optical and transport measurements were mainly dependent on the overall fluence of the excitation as compared to the electric field. This has major implications on possible microscopic mechanisms that could explain such a behavior which will be discussed in the next chapter. Although THz-TDS and transport measurements have very different time resolution (~ 100 fs vs. ~ 1 ns), a similar decay time of the induced effect on the order of 10 ns could be extracted from the data. Transport experiments, however seem to be additionally influenced by heating effects that are observable on even longer nanosecond timescales.

Furthermore, first temperature dependent transport measurements suggest a similar behavior across the equilibrium superconducting transition temperature as the optical properties measured earlier.

6 Mechanisms for Light-Induced Superconductivity in K_3C_{60}

Shortly after publication of the first signatures of light-induced superconductivity in K_3C_{60} several theoretical works have been proposed aiming to interpret the microscopic origin of the transient state. Each of those approaches can be assigned to one of the following three theory subgroups:

- The resonant excitation of an IR-active phonon couples non-linearly to intramolecular Raman active modes that stabilize superconductivity [123, 184, 185].

- The resonant excitation of an IR-active phonon couples directly to the electronic degrees of freedom of the system that in turn influence its superconducting properties [121, 186–188].

- The incipient radiation directly couples to the electronic system of K_3C_{60} e.g. by excitation of an exciton, which influences superconductivity [189, 190].

On top of this, comparison to phenomenological descriptions of superconductivity and to mechanisms for dynamic synchronization, can describe several aspects of the superconducting state including the appearance of distinct timescales that match our experimental results. This chapter will review these approaches and evaluate them on the basis of our new experimental findings.

6.1 Microscopic Models

Although driven K_3C_{60} features remarkable similarities in its optical and electronic properties at high temperatures to its equilibrium superconduct-

ing state below T_c, the microscopic mechanism causing this is not yet understood.

6.1.1 Response via phonon-phonon coupling

An obvious approach for a microscopic interpretation relies on the resonant excitation of the mid-infrared T_{1u} vibrational modes (cf. Chapter 2). The wavelength dependence of the light induced effect presented in Fig. 3.4 b supports this argument as the highest effect was measured around $T_{1u}(3,4)$, while there was almost no response near 600 meV.

In the first paper on light-induced superconductivity in K_3C_{60} by Mitrano et al. [123] a mechanism based on a nonlinear phononic coupling between the IR-active T_{1u} mode and the Raman-active H_g mode was suggested. The highly intense driving pulses, which are on the order of few MV/cm, are capable to strongly distort the carbon bonds on the C_{60} molecules in an oscillatory manner. As an estimate, one can calculate the induced polarization when the $T_{1u}(4)$ phonon at $\omega_{pump} = 168.8$ meV is pumped:

$$P = \frac{\sigma_1(\omega_{pump})}{\omega_{pump}} E = 2.35 \times 10^{-6}\,\mathrm{C/cm^2} \tag{6.1}$$

Here $E = 1$ MV/cm is used and $\sigma_1(T_{1u}(4)) = 120\ ^{-1}\mathrm{cm}^{-1}$ was obtained from measurements in [191]. The necessary displacement to obtain this dipole moment is now calculated via

$$\delta = \frac{P}{nZ_{eff}e} \tag{6.2}$$

with n being the number of dipoles per unit volume and Z_{eff} the effective charge (cf. [192] for definition, $Z_{eff}(T_{1u}) = 0.147$). This yields a displacement of $\delta = 0.24$ Å which is ~17 % of the C-C bond length, when all incident photons contribute to the effect.

It can be expected that with such large modulation of the molecular structure, higher order coupling effects can no longer be neglected. Furthermore, it has been shown earlier [42, 45] that infrared- and Raman-active modes can be nonlinearly coupled and possibly drive a phase transition into a non-equilibrium superconducting state.

The lowest order nonlinear coupling possible is of the form $Q_{IR}^2 Q_R$ where Q_{IR} denotes the light-driven coordinate exciting the T_{1u} phonon. All even powers of Q_{IR} have finite time averages and can thus result in a static renor-

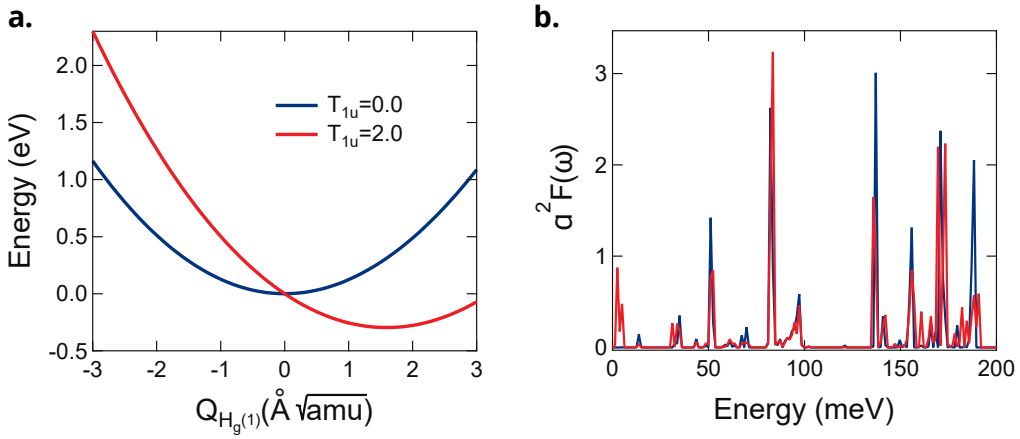

FIGURE 6.1: INFLUENCE OF $Q_{IR}^2 Q_R$ MODE COUPLING ON ELECTRONIC STRUCTURE.
a. Calculated total energy of the $H_g(1)$ vibrational mode. The equilibrium case is displayed in blue while its reshaping in the driven state is shown in red. Here, the equilibrium position of the $H_g(1)$ mode is shifted by about 1.5 Å$\sqrt{\text{amu}}$ when the amplitude of the T_{1u} mode is 2 Å$\sqrt{\text{amu}}$ **b.** $\alpha^2F(\omega)$ is the calculated electron-phonon coupling function plotted against energy. The equilibrium and distorted cases are displayed in the same color scale as in a. Figure adapted from [123].

malization of the Hamiltonian. Q_R describes the anharmonic coupled Raman coordinate. Possible candidates for this mode in K_3C_{60}, which are allowed by symmetry and known to be of importance for superconductivity in the fullerenes, are the H_g modes.
Figure 6.1 a shows the result of a density functional theory (DFT) calculation [123] predicting a shift of the energy minimum of the coupled $H_g(1)$ Raman mode when the $T_{1u}(4)$ vibration is excited. This implies a structural deformation along the $H_g(1)$ coordinate upon pumping the $T_{1u}(4)$ mode. A recalculation of the band structure in the distorted system revealed a lift of the degeneracy at the Γ point. In a next step the electron phonon coupling of the distorted structure can be compared to the equilibrium case (cf. Fig. 6.1 b). The most relevant changes can be observed for the low energy intermolecular modes at 5 meV which only couple to t_{1u} electrons in the driven state. Integration of the Eliashberg function $\alpha^2F(\omega)$ yielded a ratio of ~2.8 for the electron-phonon coupling in the dynamically distorted structure compared to the equilibrium. This enhancement was interpreted as leading to a higher pairing strength and superconducting transition temperature.

Besides this first order coupling, Knap et al. in Ref. [185] also analyzed the influence of higher order nonlinearities such as $Q_{IR}^2 Q_{R,k} Q_{R,-k}$. They identify a competition between enhanced Cooper pair formation and pair breaking due to the fact that when phonons are driven to high amplitudes, their electron-phonon scattering rate is increased which in turn weakens

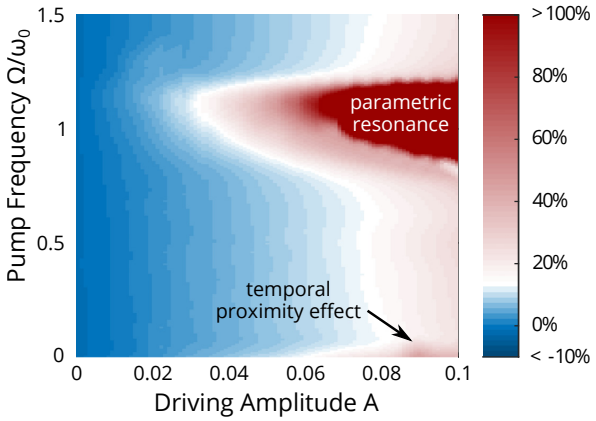

Figure 6.2: Increase of T_c via dynamical Cooper pair formation.
The enhancement of the critical temperature with respect to its equilibrium value is plotted in color as a function of the pump frequency Ω/ω_0 and driving amplitude A. ω_0 is the mean phonon frequency. Figure adapted from [185] with permission by the American Physical Society.

superconductivity. Figure 6.2 shows the enhancement of T_c with respect to pump frequency and driving amplitude. With a growing amplitude of driving, T_c is uniformly increased and strongly enhanced when the pump frequency is closely matching the phonon frequency. The enhancement of pairing strength in this model is presented as a combination of a static mode softening and dynamic phonon squeezing contribution. Statically, mode softening due to renormalized Raman phonon frequencies can, for a negative nonlinearity, suppress electron tunneling which increases the density of states at the Fermi level and thus favors superconductivity. Additionally, a parametrically driven oscillator can generate phonon squeezing correlations that further suppress electron tunneling.
The authors state that in principle one should be able to distinguish these two effects in optical pump-probe spectroscopy since mode softening should show a linear dependence with the driving field strength while phonon squeezing would in this case react quadratically. Therefore, already the static distortion of the lattice, which is mediated by a nonlinearity, should depend on some power of the electric driving field.

In our observations, however, the amplitude of the measured effect, at least in the long pulse and high fluence regime, depended only on the integrated pulse area and showed a rather flat dependence on the field strength (cf. Fig. 5.12). Therefore, the proposed nonlinear phonon mechanisms are most likely not correct or play only a negligible role.
Similar arguments also hold for a recent extension of this approach where Babadi et al. developed a theory of light-induced superconductivity based on lattice nonlinearities in driven phonon systems [184]. In contrast to the

previous studies they show that even stronger enhancement of the electron-phonon coupling can be achieved by taking into account dynamical effects similar to a parametric amplifier that are not described by time-averaged Hamiltonians. The authors point out that other competing effects such as the generation of high-energy phonons dissipating their excess energy to electrons have to be taken into account. Without an external cooling mechanism, in their model, enhancement of Cooper pairing might be limited to short timescales, that are not compatible with the metastable state observed in our experiments, as high-energy phonon excitations will ultimately also heat the electronic system.

6.1.2 Response via phonon-electron coupling

In this section we discuss alternative approaches that could possibly describe the non-equilibrium properties of photo-excited K_3C_{60}, which are still based on an excitation of infrared active phonons that now directly couple to the electronic system.
In charge transfer salts it was observed that mid-infrared excitation of localized molecular vibrations could periodically modulate the effective electronic interaction (the Hubbard U) of the conduction band [51, 129]. A modulation at twice the frequency of the vibrational mode was observed, which indicates a quadratic coupling of the molecular vibrations to the local charge density. A similar effect could be expected in the doped fullerides that in turn could interact with their superconducting properties. As described in Section 2.3, the intramolecular Coulomb repulsion U of the t_{1u} states is on the same order of magnitude as the bandwidth W, which implies a strong coupling regime. Furthermore, the H_g Jahn-Teller phonons have energies that present a significant fraction of W ($\omega_{ph}/W \sim 0.2$) and can drive the system into a situation of inverted Hund's coupling ($J = J_H + J_{ph} < 0$, cf. Section 2.4.2) where orbital fluctuations promote superconductivity. A change in U of the t_{1u} orbitals has little impact on J, which rather depends on the spin-orbit coupling but can influence the delocalization of electrons which is a prerequisite for superconductivity.

In [123] the authors estimate how much the Coulomb repulsion of the t_{1u} orbitals of a C_{60} molecule is changing, when the $T_{1u}(4)$ phonon mode is driven. They use tight binding calculations to obtain the relevant C_{60} molecular orbital hybridization. In combination with a "frozen-phonon" approach, which assumes that molecular orbitals follow the atomic distortions adiabatically (Born-Oppenheimer approximation), they obtain

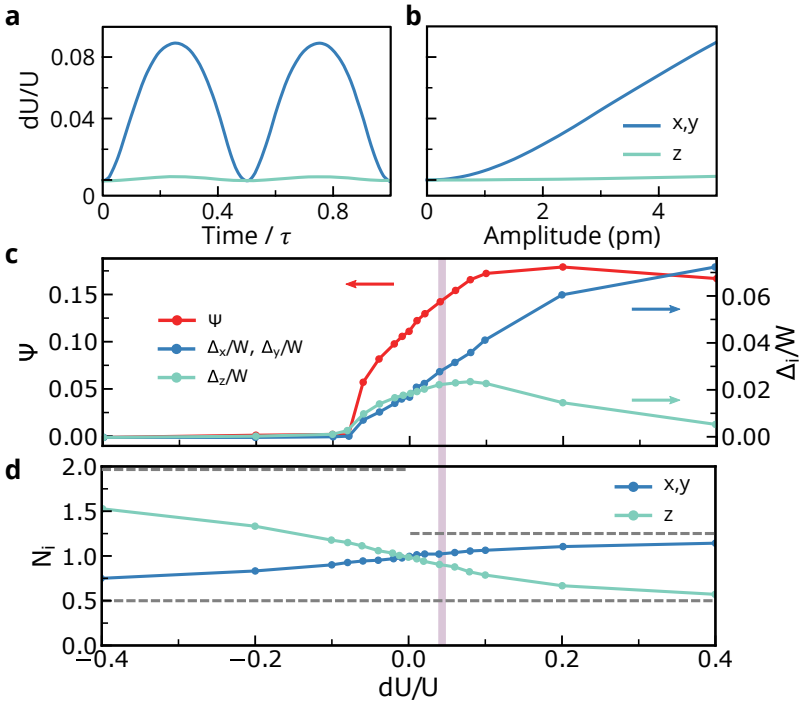

Figure 6.3: Influence of a modulated Coulomb repulsion on superconducting order.

a. Change of the intra-orbital Coulomb repulsion dU/U during a period of the excited $T_{1u}(4)$ vibration at a vibrational amplitude of 5 pm. The values for the x and y orbitals are shown in blue and for the z orbital in green. **b.** dU/U as a function of the amplitude of the phononic excitation. **c.** Dependence of the total superconducting order parameter Ψ (left axis, red) and the orbitally resolved superconducting gaps $\Delta_{x,y,z}/W$ (right axis, blue and green) on the imbalance in Coulomb repulsion dU/U. **d.** Orbital occupancies are displayed as a function of dU/U. The respective asymptotic behavior of the different orbitals is indicated as dashed gray lines. The vertical purple bar indicates the dU/U regime of a photoexcitation with a fluence of ~1 mJ/cm². Data for panels a and b was obtained from [123] while panels c and d are adapted from [121].

the relative change of U during a period of the oscillation (cf. Fig. 6.3 a). As expected, the variation of U is modulated at twice the frequency of the vibration and can reach almost 10 % at a C-atom displacement amplitude of 5 pm (cf. Fig. 6.3 b). Without restriction of generality, in this example the vibration is polarized along the z-axis leading to a degenerate x- and y-axis response that is much stronger compared to the z-axis.
Kim et al. theoretically showed in [121] that this kind of "interaction imbalance", where the intramolecular Coulomb repulsion is larger in one of the t_{1u} orbitals than in the others, can indeed enhance superconductivity due to enhanced orbital fluctuations. Mazza et al. furthermore showed that this dynamically formed superconducting state can extend beyond the equilibrium critical temperature [188].
Figure 6.3 c summarizes the findings of a significant increase of the superconducting order parameter (left axis, red curve) and the orbitally resolved gaps (right axis, blue and green curves) when $dU/U > 0$. The importance of an orbital differentiation is highlighted in panel 6.3 d, showing the individual occupancies of the three orbitals. For $dU/U > 0$ a crossover to a singlet state is created, e.g. with double occupancy in the x-orbital with a shared electron between y and z (see also Fig. 2.7).
In contrast, even if spin-singlet pairs are formed by a crystal-field splitting, stronger localization (dU/U < 0) is detrimental to superconductivity [121].
The purple vertical bar in Fig. 6.3 shows the estimated region for dU/U of our experiments at low fluence, indicating an enhancement of T_c by a factor of ~1.35.

Another theoretical approach that is based on a coupling of driven dipole active modes with the electron density suggests an electron-density-dependent squeezing of the phonon state, which was shown to provide an attractive contribution to the electron-electron interaction [187]. The authors apply a minimal tight-binding model of electrons in a lattice including electronic interactions. With this they not only show a light-induced formation of a superconducting gap but also compute optical properties that feature good similarity to our optical measurements with low power excitation.

Without claiming completeness, reference should be made to another approach based on a modulation of the electronic system that could be achieved via modulation of phonons [186]. In this case it was shown in a Hubbard-type model that periodic driving of site energies is capable of enhancing electron pairing in strongly correlated systems by slowing down electron hopping without reduction of superexchange interactions and pair hopping.

Although the theories discussed in this section present convincing arguments for enhanced superconductivity via coupling of an excited T_{1u} infrared mode to the t_{1u} electronic orbitals, due to inversion symmetry of these orbitals, modulation of U couples at lowest order to Q_{IR}^2. As stated before, this should result in a measurable dependence of the enhancement on the electric field of the drive, which at least in the long pulsed excitation regime we do not observe. Furthermore, in the experiments carried out using long CO_2 laser pulses (see Section 5.2), excitation is not centered exactly at one of the T_{1u} modes yet it shows the same superconducting features in the optical conductivity. The fact that superconductivity is enhanced in a rather broad frequency range (cf. also Fig. 3.4 b) suggests that most probably not only a specific phonon excitation is responsible for this effect.
The extremely long decay times of several nanoseconds after excitation with high power MIR pulses would be highly unusual for an effect that is relying on vibrating phonons since even long phonon dissipation times in the alkali doped fullerides are on the order of several picoseconds [193].

6.1.3 Pure electronic response

Since theoretical descriptions for light-induced superconductivity that rely on the coherent excitation of phonons do not seem to capture all experimental observations, including the broad wavelength dependence and metastability of the state, an all-electronic approach could provide further insights. Motivated by this Nava et al. proposed a mechanism based on infrared-induced excitons, that could provide an effective cooling allowing the transient state to persist up to much higher temperatures [190].

The light-induced gap opening in the optical conductivity features a broad frequency response measured from 80 to 200 meV (cf. Fig. 3.4 b) without any significant peaking. Rather, the effect seems to be comparable to the ~100 meV wide peak region of polaronic absorption centered around 50 meV (see σ_1 in Fig. 3.1).
As described already in Chapter 2.3 and 2.4, the band structure of K_3C_{60} features a narrow, threefold degenerate t_{1u} LUMO of C_{60} that is occupied by the potassium conduction electrons. The high symmetry of C_{60} results in large degeneracy of molecular orbitals and thus Jahn-Teller molecular distortions that lower this symmetry are expected to strongly influence the electronic system. Although Hund's rule exchange favors a high spin state, Jahn-Teller coupling inverts Hund's rules bringing the molecular ground state to $S = 1/2$ rather than $S = 3/2$.

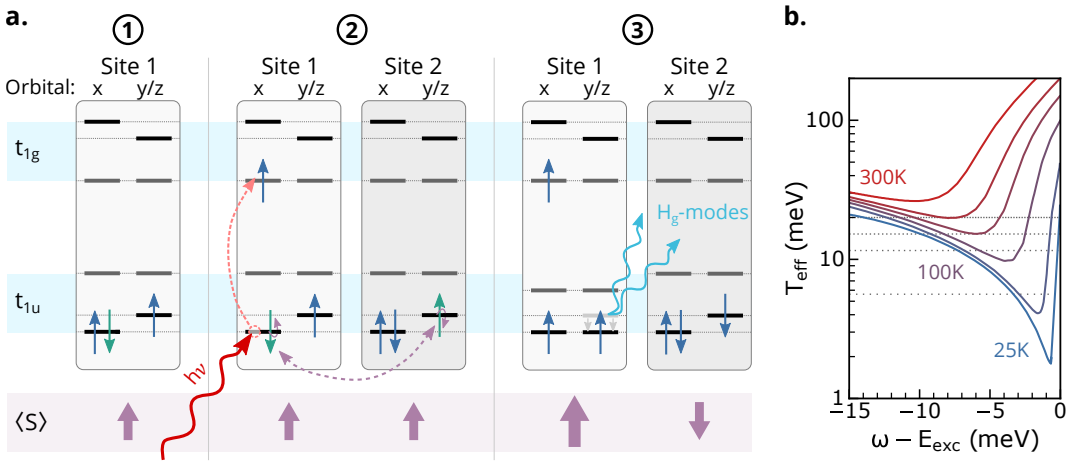

FIGURE 6.4: LASER INDUCED QUASIPARTICLE COOLING.

a. Schematic representation of the absorption of a laser pulse and subsequent electronic rearrangement. In the initial state (1) all three electrons per site occupy the t_{1u} band that is split due to the Jahn-Teller effect (cf. Fig. 2.7). Upon irradiation with the laser pulse in (2) two processes happen simultaneously: 1. a t_{1u} electron is lifted into a t_{1g} orbital. Note that here the JT-coupling has an opposite sign compared to the t_{1u} states. 2. A paramagnon is exchanged between site 1 and site 2 (violet arrow) resulting in a spin flip of the originally paired t_{1u} electron. This is caused by the antiferromagnetic exchange J, that favores an antiparallel over the original parallel configuration of magnetic moments in site 1 and 2 (thick violet arrows). In (3) site 1 finally relaxes into the JT distorted A_g state via emission of H_g phonons. **b.** Laser induced effective temperature T_{eff} after the laser pulse for different initial temperatures of $T = 300\,\mathrm{K}$, $200\,\mathrm{K}$, $150\,\mathrm{K}$, $100\,\mathrm{K}$, $50\,\mathrm{K}$, and $25\,\mathrm{K}$ from top to bottom. The x-axis defines the difference between the pump light frequency ω and the exciton energy E_{exc} with quasiparticle bandwidth of $100\,\mathrm{meV}$ and sharp exciton line. The horizontal dashed lines represent the levels of equilibrium T_c at $0\,\mathrm{GPa}$, $0.5\,\mathrm{GPa}$, $1\,\mathrm{GPa}$ and $2\,\mathrm{GPa}$ from top to bottom. Figure adapted according to [190].

The lowest dipole-allowed excitation of the C_{60}^{3-} molecule can be achieved by transferring one electron from the t_{1u} LUMO into the ~1.2 eV higher laying t_{1g} LUMO+1, which is also threefold degenerate (see Fig. 2.4). The subspace of states within this large energy gap, which is again generated by exchange interactions and Jahn-Teller vibrational couplings, consists of 90 states. Therefore, and due to the fact that Jahn-Teller couplings of the excited state are highly effective, the electronic state of the driven system is even more susceptible to deviations in those interaction potentials as compared to the t_{1u} ground state [190, 194, 195].

Nava et al. calculated that the energy of the next state within this gap (the $A_g(4)$ term) is drastically reduced by Jahn-Teller and dipole-dipole interactions leading to an effective transition energy on the order of 100 meV. The

transition from the T_{1u} to this low-lying A_g state is considered as a genuine triplet exciton responsible for the broad peak in the infrared spectrum of K_3C_{60}. Although optical creation of this exciton alone is not spin-allowed it could be realized upon simultaneous interaction with a paramagnon (this is a low-energy spin-triplet particle-hole pair). This effect is comparable to the virtual transitions described by Rice and Choi in [196] that allow the uncharged T_{1u} vibrations in C_{60} to gain oscillator strength so that optical excitation is at all possible.
Following this route, while the short infrared light pulse is applied, quasiparticles are excited and energy is transferred into the exciton-paramagnon system. At equilibrium there are more paramagnons available than excitons, which results in a net entropy flow from the former to the latter within the pulse duration.
Under the assumption that the lifetime of the exciton state is much longer than the laser pulse length, compared to its equilibrium conditions, an effective cooling of the Fermi liquid could be achieved resulting in light-induced superconductivity. This is compatible with the experimental observation from the reflection spectra of K_3C_{60}, where the opening of a superconducting gap could be seen as a removal of thermally excited quasiparticle states. Thus, an effective quasiparticle temperature $T_{eff} < T$ may result in a superconducting state at $T > T_c$.
Although the energy in this model is initially unevenly distributed among the distinct subsystems, the total energy of the system is increased by the laser pulse. Thus, on long timescales the excitons will eventually equilibrate with the quasiparticle subsystem resulting in overall heating.
Figure 6.4 a shows a sketch of the energy diagrams during and after laser excitation including exciton occupation and paramagnon exchange. Panel b shows a plot of the effective temperature T_{eff} after the laser pulse as a function of $\omega - E_{exc}$, where ω is the pump frequency and E_{exc} the sharp exciton energy. The vertical dashed lines represent equilibrium T_c with increasing pressure values (0 GPa, 0.5 GPa, 1 GPa and 2 GPa) from top to bottom. This indicates, that the effective temperature can indeed be lower than its equilibrium value when the pump frequency is lower than the exciton energy so that exciton creation additionally requires the absorption of thermal quasiparticle-hole triplet pairs. Furthermore, this model is compatible with the experimental observation that T_c is reduced with increasing pressure.

In a second paper the same group developed a toy model illustrating that impulse perturbations can be carefully tuned so that a transient cooling of low energy states at the expense of higher energy ones is possible until the system equilibrates [189]. A pictorial description of this model is given in Fig. 6.5. At first the system consists of a thermalized distribution of low- and high-energy excitations. In subfigures b and c the laser pulse first ef-

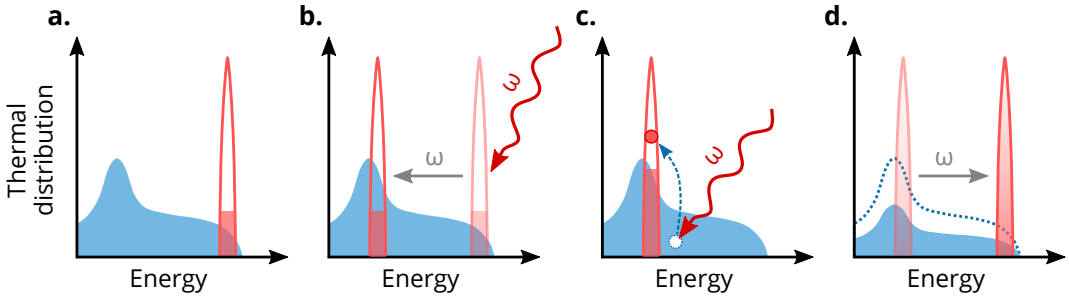

FIGURE 6.5: ILLUSTRATION OF THE COOLING MECHANISM BY IMPULSE PERTURBATION.
a. Thermalized distribution of low- (blue) and high-energy (red) excitations. **b.** A pump-pulse with energy $\hbar\omega$ arrives at the sample. For the duration of this pulse, the high-energy states are effectively shifted towards lower frequencies by its energy. **c.** Now the laser excites thermal quasiparticles into the shifted and poorly populated high-energy states. **d.** When the laser is turned off, the now highly populated high-energy states shift back to their initial position. Thus, at the expense of this overpopulated high energy peak, thermal states are removed from the equilibrium population resulting in an effective cooling of this subsystem. Figure adapted from [189].

fectively shifts the high energy excitations downward by its energy equivalent and then induces a population transfer from the thermal bath into the poorly populated state. Here, the peak of high energy excitation serves as an entropy sink during the laser irradiation. Once the laser is turned off again (see subfigure d) the now populated states turn back to their original position and therefore are effectively cooling the low energy excitations. From now on the entropy is slowly flowing back by recombination with a relaxation timescale longer than the laser pulse length.
In Ref. [190] the authors state that a non-radiative relaxation of a triplet exciton to a dark state might lead to a much longer overall lifetime that might be compatible with our experimental observations. Furthermore, for this kind of electronic excitation the "cooling strength" would depend mainly on the photon number rather than on the electric field of the pump. Finally, the theory is compatible with a relatively weak wavelength dependence and the experimental results under pressure, rendering it - to our knowledge - the most promising candidate to describe the light-induced effects in K_3C_{60}.

6.2 PHENOMENOLOGICAL MODELS

Clearly one of the main findings of this work is the nanosecond long lifetime of the transient light-induced state in K_3C_{60}. Although direct excitation of

the electronic system under certain conditions could allow for such relaxation times (see last section) most processes such as decay of vibrations and even non-radiative recombination rather occur on picosecond timescales. If the physics at hand is based on the relaxation of a superconducting into a metallic state after excitation, then it might be instructive to look for possible scenarios leading to this characteristic time scale within common phenomonological models for superconductivity.

From this point of view, we build a phenomenological time-dependent Ginzburg-Landau (TDGL) model on a lattice to capture the dynamics of the superconducting order parameter after laser excitation[1]. We follow a recent argument [197], that links out-of-equilibrium superconductivity to the presence of phase-incoherent Cooper pairs above the equilibrium T_c. We assume that under strong optical excitation these pairs become synchronized even at a base temperature in excess of the equilibrium T_c resulting in properties of a coherent superconductor. In our model we postulate the existence of such a phase-synchronized state above the equilibrium critical temperature and study how the order is lost when the light pulse has passed and the system is left to relax back to the equilibrium ground state.
On each site of the lattice a local superconducting order parameter $\Psi_m = |\Psi_m|e^{i\phi_m}$ is defined and the macroscopic properties of the system can be followed by $\langle\Psi_m\rangle$, their average over the whole lattice (see Appendix F for more details).

The relaxation of a superconducting state ($|\langle\Psi_m\rangle| > 0$) to the equilibrium metallic one ($|\langle\Psi_m\rangle| = 0$) can happen either by a fast decrease of the amplitudes of the local order parameters $|\Psi_m|$ (i.e. by annihilation of Cooper pairs) or by a significantly slower randomization of their phase. The latter is found to dominate in phase-incoherent superconductors, where phase fluctuations are significantly larger than amplitude fluctuations. In this case, the free energy surface of the system shows a minimum even above T_c at a finite local order parameter amplitude $|\Psi_m|$ suppressing amplitude fluctuations (cf. Fig. 6.6 a). Interestingly, as the relaxation to the non-superconducting ground-state happens via a thermally driven diffusion of the local phases, the synchronized state can survive significantly longer than the typical amplitude relaxation times in superconductors, which are on the order of several picoseconds [198].

1 This work was conducted in cooperation with F. Schlawin and D. Jaksch from the Department of Physics, Clarendon Laboratory, University of Oxford

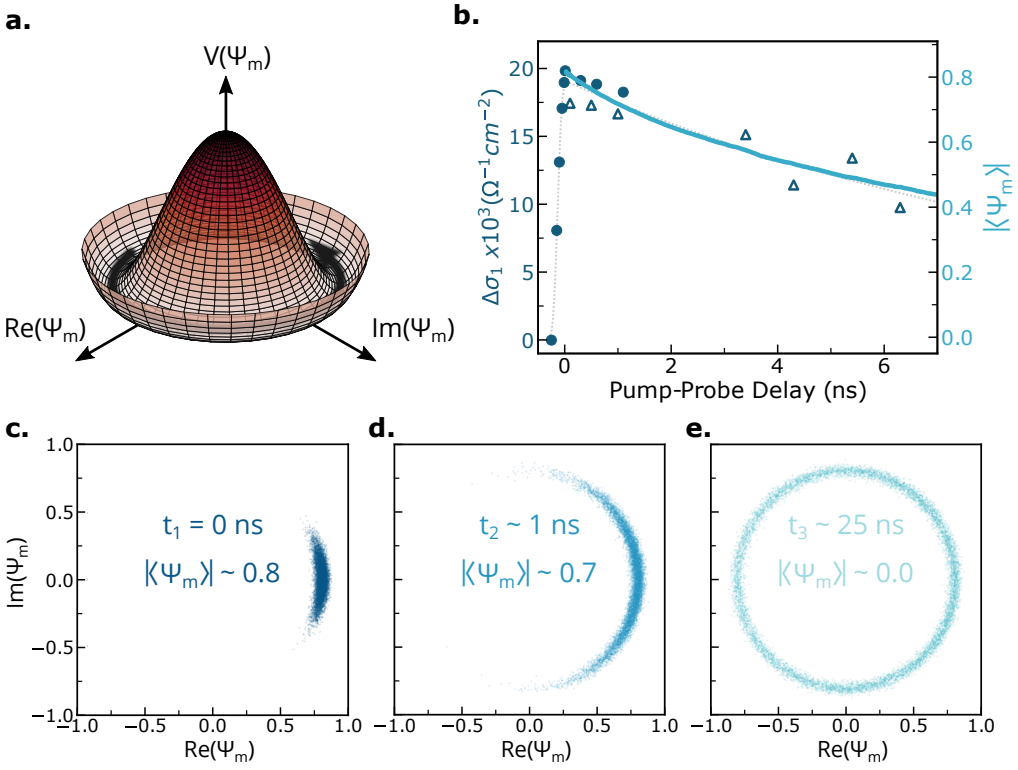

FIGURE 6.6: MODELLING OF THE RELAXATION OF THE METASTABLE SUPERCONDUCTING ORDER PARAMETER.

a. Local free energy potential as a function of the complex superconducting order parameter Ψ_m. **b.** Time evolution of the integrated loss of spectral weight in the region of the superconducting gap (left axis, blue dots and triangles denote measurements on two different samples) and corresponding modelling (right axis) using a time dependent Ginzburg Landau framework as described in the text. Three snapshots of the complex order parameter are shown in subfigures **c.** (directly after excitation), **d.** (1 ns after excitation) and **e.** (25 ns after excitation).

Figure 6.6 b displays the time dependence of the integrated spectral weight loss over the optical gap

$$\Delta\sigma_1 = \int [\sigma_1^{equil}(\omega) - \sigma_1^{trans}(\omega)]d\omega \tag{6.3}$$

that is a quantity proportional to the superfluid density in a superconductor. Here $\sigma_1^{equil}(\omega)$ and $\sigma_1^{trans}(\omega)$ are the real parts of the optical conductivities measured in the photo-induced and equilibrium state, respectively. This data is based on the same experiment already discussed in Chapter 5.2.2. This quantity can be compared to the normalized amplitude of the order parameter extracted from TDGL simulations (see Appendix F for more details) and a good agreement is found, yielding a phase relaxation time of approximately 15 ns. Figures 6.6 c-e complement this observation and show the time evolution of the complex order parameter extracted from the same simulations directly after excitation as well as 1 ns and 25 ns later. These snapshots illustrate directly how in this model the local order parameters Ψ_m evolve by randomizing their phase ϕ_m around a ring at constant $|\Psi_m|$ until the metallic state at $|\langle\Psi_m\rangle| = 0$ is reached.

7 Conclusions and Outlook

The interaction of light with matter is traditionally used as a valuable tool for spectroscopic material analysis. Beyond this, it now also enables precise control of the materials properties themselves. This approach is particularly promising for strongly correlated electron systems with many competing phases. High-intensity laser fields can selectively couple to microscopic degrees of freedom and generate novel non-equilibrium states from which new order can emerge. A fascinating example of this was found in the doped fullerides where excitation with mid-infrared light can drive the system in a state with superconducting properties at five times the static critical temperature.
Both from an academic and a technological perspective it was important to make this state more accessible for further analysis by extending its picosecond lifetime beyond the capabilities of ultrafast spectroscopy. Apart from the development of a new mid-infrared laser source capable of delivering intense and long pulses of tunable duration, the main achievement of this work is the discovery of a nanosecond long lived metastable state with the same properties as a superconductor. This enabled first electronic transport measurements, which further substantiate the idea of a light-induced superconductor at high temperatures.

The discovery of a metastable state prompts comparison with previously measured responses observed under sustained driving, such as the microwave enhancement of conventional superconductivity [199, 200]. One evident difference with these measurements is that the temperature scale observed here is far larger than that reported in the microwave enhancement case. Furthermore, in the case of microwave enhanced BCS superconductivity the effect was observed only for excitation below the superconducting gap, which was interpreted as a result of quasi-particle redistribution and of renormalization of the parameters entering the BCS equations [201]. In the microwave experiments, complementary measurements, where excitation was tuned immediately above the gap, yielded a reduction of the superconducting order. Our experiments are conducted in a different regime, that is at pump-photon energies that are at least one order of magnitude larger than the low temperature

equilibrium superconducting gap, and in a regime in which the primary coupling of the mid-infrared radiation is not with the condensate but with other high-energy excitations, such as molecular vibrations or collective electronic modes. Hence, it is unlikely that the mechanism invoked for microwave enhancement can explain these observations.

Other experimental reports have documented a sustained, metastable enhancement of superconductivity in oxygen deficient $YBa_2Cu_3O_{7-\delta}$ samples, after exposure to radiation with frequencies ranging from ultraviolet to near infrared [202–204] (cf. Chapter 1.2). However, in all these cases the superconducting transition temperature of the irradiated superconductor never exceeded the equilibrium transition temperature at optimal doping. These observations were either interpreted as a result of photodoping towards a more metallic state favoring superconductivity or involved annealing of oxygen deficient samples. In contrast, the data reported here show enhanced superconducting properties well above the equilibrium transition temperature by excitation with photon energies away from interband transitions. Thus, none of the previously invoked mechanisms offers a plausible explanation for our findings, in which the response is observed in a metal and the signatures of metastable photo-induced superconductivity extend far above the equilibrium transition temperature T_c.

Significant questions remain about dissipation during the drive. Indeed, energies of 20 mJ/cm² would be expected to raise the overall temperature of the sample by at least 100 K, although hot carrier diffusion at early times [197, 205] may reduce the heating to only a few tens of Kelvin. Regardless of the mechanism and the degree of heating, pre-thermalization of the driven superconducting order parameter, which may be immune to dissipation at early times, could be important.

The dependence of the light-induced effect on the energy and not on the pulse duration is surprising, and therefore descriptions that exclusively depend on the peak power of the excitation can be disregarded. On the other hand, this does by no means imply that exotic quantum effects cannot play a role in the generation of the light-induced state.
A collective synchronization of an ensemble of oscillators, which is a common phenomenon in various oscillatory systems such as phase locked Josephson junction arrays, cardiac pacemaker cells in the heart, power grid dynamics, flashing of fireflies and neuronal brain activity, depends strongly on the exact nature of the system [206]. Factors like the coupling strength, connectivity of the network, external forces and internal delays of the system affect the formation and relaxation of synchrony and so far we do not fully understand which of these are influenced most prominently

by a (picosecond long) pulsed excitation. This is to emphasize that the assumption of a light-induced phase synchronization of Cooper pairs may be consistent with the measured independence of the effect on the electric field.

Finally, the data reported here hold a significant promise in the quest to extend lifetimes even further. New lasers capable of generating longer pulses or suitably designed trains of pulses could be developed in order to sustain the coherence of this state. Already the long lifetimes of nanoseconds observed in this work open up the possibility of studying these effects with other low frequency probes, ranging from measurements of magnetic susceptibility to scattering and transport methods. Right now we are working on a measurement of the magnetic susceptibility of the light induced state wherein the Meissner effect represents a long desired benchmark for superconductivity.

Recent theoretical [207] and experimental reports [208] suggest that the superconducting order parameter can be influenced also by the electromagnetic environment of an optical cavity. The observations made in in alkali doped fullerides could be further expanded on by combining cavity settings with external driving [209], as a means to reduce the required excitation and hence dissipation and heating.

Appendices

A K_3C_{60} SAMPLE GROWTH AND CHARACTERIZATION

The K_3C_{60} powder pellets used in this work were prepared and characterized as previously reported [122, 123]. Finely ground C_{60} powder and metallic potassium in stoichiometric amounts were placed in a vessel inside a Pyrex vial, evacuated to 1×10^{-6} mbar, and subsequently sealed. The two materials were heated at 523 K for 72 h and then at 623 K for 28 h. To ensure that C_{60} was exposed only to a clean potassium vapor atmosphere, solid potassium and fullerene powder were kept separated during the heating cycle. The vial was then opened under inert atmosphere (in an Ar glove box with < 0.1 ppm O_2 and H_2O) and the black powder was reground, pelletized and further annealed at 623 K for 5 days. This yielded phase pure K_3C_{60} powders, as confirmed by powder X-ray diffraction measurements (Fig. A.1 a) that indicate an average grain size ranging from 100 – 400 nm. Figure A.1 b shows magnetic susceptibility measurements of the obtained K_3C_{60} pellets upon cooling with an external magnetic field of zero (ZFC) and 400 A/m (FC). A critical temperature around 19.8 K can be extracted, which is in agreement with literature [56].

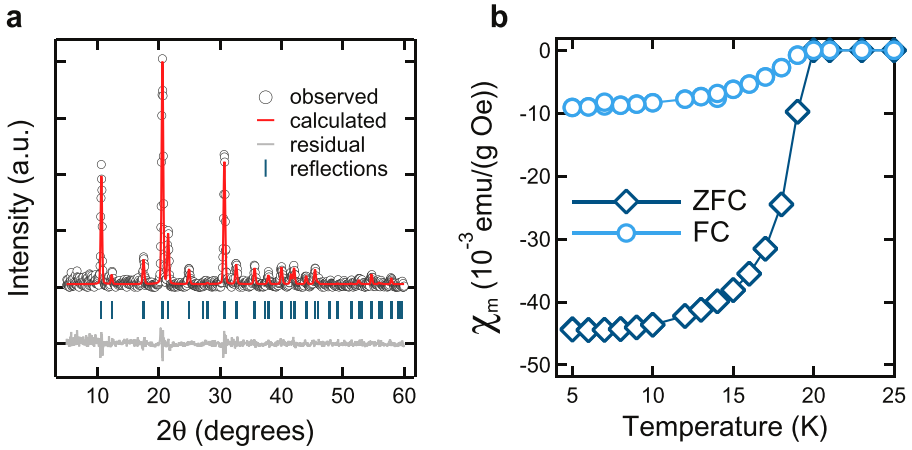

FIGURE A.1: SAMPLE CHARACTERIZATION.

a. X-ray diffraction data and single f.c.c. phase Rietveld refinement for the K_3C_{60} powder used in this work. **b.** Temperature dependence of the sample magnetic susceptibility measured by SQUID magnetometry upon cooling without (ZFC: zero field cooling) and with a magnetic field applied (FC: field cooling).

B Optical techniques

B.1 Hybrid solid-state gas laser pump-probe setup

A basic description of the setup is already given in Section 4.4. Based on this, Fig. B.1 summarizes the essential parameters of the apparatus developed in this work.
The first Ti:Al_2O_3 amplifier **(2a)** was used for nonlinear generation of femtosecond mid-infrared light pulses that were seeding the CO_2 oscillator. A second more powerful amplifier **(2b)** that was seeded by the same Ti:Al_2O_3 oscillator **(1)** was used for semiconductor switching as well as generation and detection of terahertz radiation. It was necessary to use a second amplifier for this, since the optical delay through the CO_2 oscillator and amplifier is on the order of 1.4 µs (cf. Section 4.2) which corresponds to more than 400 m optical delay. It is experimentally not practical to compensate such long paths with optical delay lines. Since the oscillator **(1)** is running at a much higher repetition rate of 80 MHz as compared to the 1 kHz repetition rate of the amplifiers, it was possible to seed these two amplifiers with two different, time-shifted pulses so that the maximum delay between both arms reduced to $1/80\text{MHz} = 12.5\,\text{ns}$ which is equivalent to an optical delay of less than 4 m. This we compensated with optical delay lines.

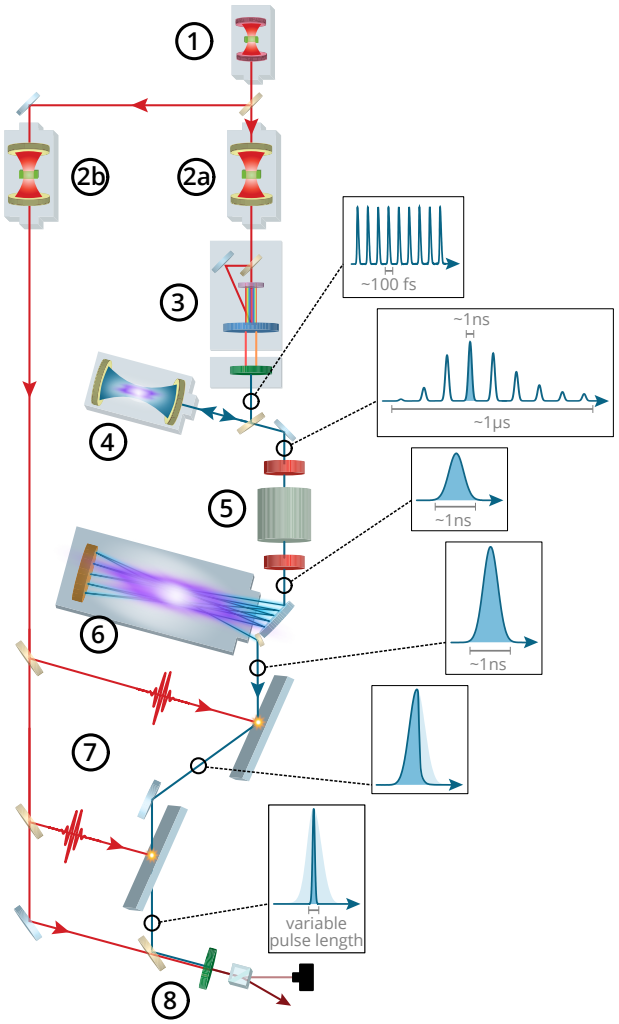

① Ti:Al_2O_3 oscillator
f = 80 MHz, λ = 800 nm
E = 6.25 nJ

② Ti:Al_2O_3 amplifiers
f = 900 Hz, λ = 800 nm
a: E = 5mJ, b: E = 7mJ

③ OPA + DFG
f = 900 Hz, λ = 10.6 µm
E = 10 µJ, L = 150 fs

④ CO_2 oscillator
f = 18 Hz, λ = 10.6 µm
Pulse train, E = 22mJ,

⑤ CdTe Pockels cell
selects central pulse
E = 730 µJ in L = 1.3 ns

⑥ CO_2 amplifier
f = 18 Hz, λ = 10.6 µm
E = 10 mJ in L = 1.3 ns

⑦ Semiconductor switching
variable pulse length
e.g.: E = 55 µJ in L = 100 ps

⑧ Cross-correlation &
Pump-probe experiments

Figure B.1: CO_2 laser setup and parameters.
The different stages of the setup are numbered and typical beam parameters are given on the right side.

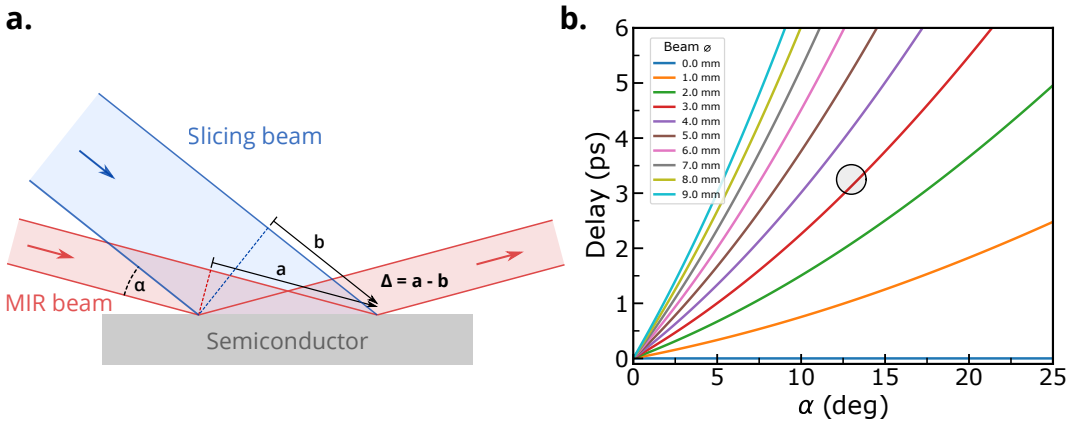

FIGURE B.2: DEPENDENCE OF THE PULSE RISE TIME ON SLICING BEAM ANGLE.
a. Schematic of the slicing geometry. Δ is the maximum path length difference. **b.** Calculation of the resulting time delay for different angles α and beam diameters. The black circle indicates the region of operation in our setup.

Another detail that was only briefly discussed in Chapter 4.3.4 relates to the limitations in the adjustability of the pulse length. Although the reflectivity rise time in a plasma mirror should mainly depend on the excitation pulse length, which in our case is about 100 fs, the minimum rise time in our setup was on the order of 5 ps. This was caused by geometrical constraints of the optical setup. Figure B.2 a displays the geometry of the sliced MIR beam and the NIR beam used for plasma generation. For a finite angle α the distances a and b are not the same. If the two pulses are perfectly overlapped in time at the left most contact point with the semiconductor, this results in an overlap mismatch at the most right contact point that corresponds to a temporal delay of $\frac{\Delta}{c} = \frac{a-b}{c}$, with c being the speed of light. Such a delay effectively limits the slicing response time when integrating the intensity spatially across the beam. Figure B.2 b shows this delay for different angles and beam diameters. The black circle indicates the situation that was realized in our setup, which explains why the measured cross-correlations of sliced pulses were always limited to rise-times of several picoseconds.

B.2 Generation of mid-infrared pulses by optical parametric amplification

Optical parametric amplification is a nonlinear process that was used in this work in combination with difference frequency generation (DFG) to convert NIR pulses from a commercial laser system into MIR pulses. These were either used for the direct excitation of the sample (cf. Sections 3.2 and 5.1) or for seeding of the CO_2 laser setup (cf. 4.2). The optical setup is very similar in both cases and a schematic drawing of the OPA with subsequent DFG used for seeding is shown in Fig. B.3.
Here, the 800 nm input beam was generated from a conventional Ti:Al_2O_3 laser system with a pulse duration of 100 fs at 1 kHz repetition rate and an energy per pulse of about 3 mJ. After the pump light for the two amplifier stages has been branched off by two beam splitters, a small portion of a few µJ remained for the generation of s-polarized white light in a 2 mm thick Al_2O_3 (sapphire) crystal. From its broadband spectrum, the visible part was removed by a low-pass filter (LP in Fig. B.3) before it was focused on a 3 mm thick, type-II BBO crystal, cut at 28° for optimum phase matching. Here it was non-collinearly overlapped with the first NIR pump beam of about 200 µJ per pulse resulting in the generation of about 5 µJ of $\lambda_{sig} = 1.48\,\mu m$ wavelength pulses. Using this as an input for the second collinear amplifi-

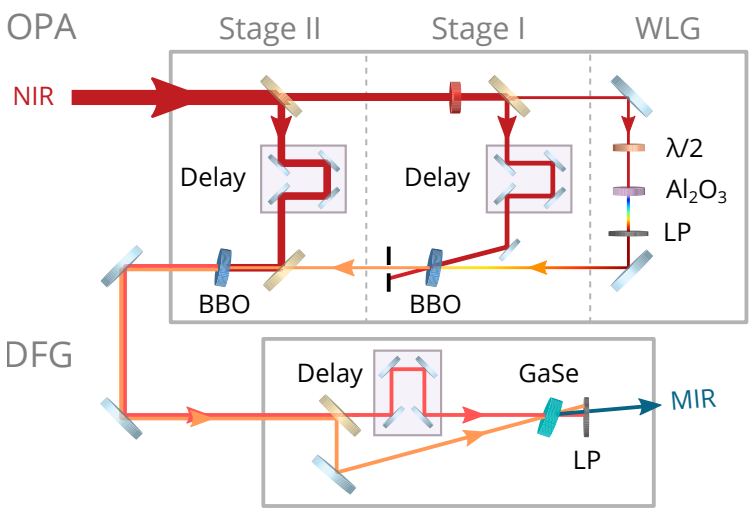

Figure B.3: Schematic of the two-stage optical parametric amplifier. From the NIR input pulses broadband white light is generated in sapphire (WLG). Out of this, a specific wavelength is amplified in the first OPA stage in a BBO. This wavelength (the signal beam) is amplified together with another MIR wavelength (the idler beam) in the second OPA stage. Subsequent DFG of signal and idler results in the MIR output pulses.

cation stage with about 2.7 mJ of pump energy per pulse in another type-II BBO crystal resulted in an amplified signal and an additional idler beam of $\lambda_{idl} = 1.74\,\mu m$ wavelength. The total output power of the cross-polarized beams was about 800 µJ. The angles of the BBO crystals were tuned to give the above output wavelengths so that DFG of the signal and idler beams in a 1.5 mm thick GaSe crystal yielded up to 12 µJ of 10.6 µm wavelength radiation with a stability of 0.5 % and a pulse length of about 150 fs. The wavelength of the DFG setup was verified by means of linear FTIR spectroscopy before the beam was used for injection seeding of the CO_2 laser.

B.3 Time resolved THz pump-probe spectroscopy

In this section we will review the utilized techniques for the generation and detection of THz radiation and appropriate methods for beam characterization. The mid-infrared pump, THz probe experiments presented in this thesis were performed on compacted K_3C_{60} powder pellets pressed against a diamond window to ensure an optically flat interface. As K_3C_{60} is water and oxygen sensitive, the pellets were sealed in an air-tight holder and all sample handling operations were performed in an Argon filled glove box with < 0.1 ppm O_2 and H_2O. The sample holder was then installed at the end of a commercial Helium cold-finger (base temperature 5 K), to cool the pellets down to the desired temperature.
Figure B.4 provides a schematic of the THz-TDS pump-probe setups used in this work. Here, a beam of 800 nm pulses, that was generated by a Ti:Al_2O_3 laser and optically synchronized with the one producing the mid-infrared excitation pulses, was divided by a beam splitter. At position (1), the reflected portion was used for the generation of THz pulses either by optical rectification or via a photoconductive antenna. The divergence of the generated THz output beam was collimated by a gold coated parabolic mirror and focused at normal incidence on the K_3C_{60} sample by another parabolic mirror. The latter allowed a maximum focusing aperture and therefore a small, nearly diffraction limited spot size. A small hole in the second focusing element permitted the simultaneous excitation of the sample by MIR pulses. The THz light reflected from the sample was collected by the same parabolic mirror and a 50:50 beam splitter made from high resistivity float zone silicon (HRFZ-Si), which has a flat transmission in the far infrared, was used to pick a portion of the beam. This part was eventually recombined with the second portion of the NIR gate beam at position (2) and used for subsequent measurement of the THz electric field profile by electro-optic

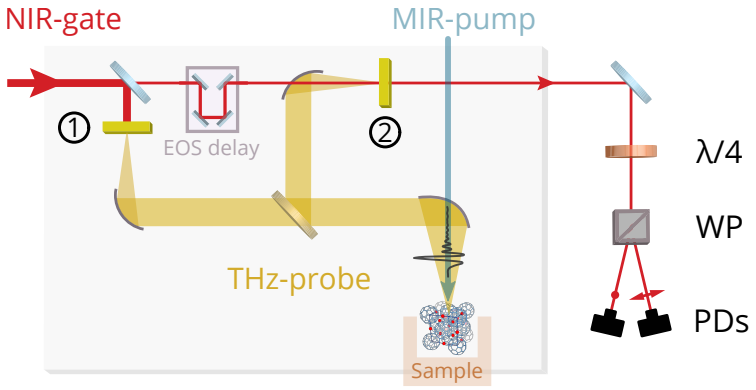

Figure B.4: Schematic of the THz time-domain spectroscopy setup.
The 800 nm gating pulse for THz generation and detection is shown in red, the mid-infrared light for sample excitation in blue and the THz-probe light in yellow. Further details of the setup are explained in the text.

sampling. The different field values were sampled by changing the optical delay between probe and gate pulses while a second delay stage (not shown) enabled the variation of the pump-probe delay. To minimize the effects of the finite duration of the THz probe pulse on the pump-probe time resolution, we performed the experiment as described in [210, 211]. The transient reflected THz field at each time delay τ after excitation was obtained by fixing the delay τ between the pump pulse and the electro-optic sampling gate pulse, while scanning the delay t of the single-cycle THz probe pulse. To prevent ice formation at the sample position and absorptions from air within the probe band, the sample holder as well as THz generation and detection was performed in a vacuum chamber at pressures of about 10^{-6} mBar (cf. grey box in Fig. B.4).

B.3.1 Generation of THz probe-pulses

The terahertz probe light for all presented time-domain spectroscopy experiments was generated either by optical rectification of 800 nm femtosecond pulses from a Ti:Al_2O_3 laser in non-centrosymmetric nonlinear crystals or by excitation of a photoconductive antenna.
In the first case, the incident electric field of a short laser pulse creates a nonlinear polarization in the crystal and the second-order effect has a time dependence proportional to the incident pulse envelope. Thus, phase-stable, few-cycle THz pulses are generated [212, 213]. Their exact beam parameters are limited by the bandwidth of the pump pulse, the length of the crystal and its transmission for both NIR and FIR frequencies. Since nonlinear crystals

feature a relevant dispersion for propagating light pulses, while low energy radiation is generated, the time-overlap of the two light beams deteriorates until the induced polarization in the material eventually becomes destructive. Thus, for efficient phase-matching, the nonlinear crystal should have a thickness shorter than this walk-off length[1]. Furthermore, long crystals limit the accessible bandwidth of the THz pulse. On the other hand, the longer a crystal is, the more THz light is generated resulting in a stronger THz field. In early THz-TDS experiments on K_3C_{60} (cf. experiments in [123]) the probe light was generated with 100 fs long 800 nm laser pulses at a repetition rate of 1 kHz in a 900 µm thick ⟨110⟩-cut ZnTe crystal. This led to a bandwidth in the range of 0.7 – 2.7 THz (~ 3 – 11 meV). Later experiments under pressure and the experiments of Section 5.1 obtained a much broader bandwidth in the range of 1 – 7 THz (~ 4.1 – 29 meV) by using shorter 35 fs long NIR pulses of 0.9 mJ power and a 200 µm thick ⟨110⟩-cut GaP generation crystal.
In contrast, in all experiments with tunable pulse length (see Section 5.2), a commercial photoconductive antenna[2] was used. Here, a voltage bias is applied across gapped electrodes on a semiconductor. Once an ultrashort optical pulse (we used a pulse length of 100 fs at 800 nm wavelength and 900 Hz repetition rate) with a photon energy higher than the bandgap of the semiconductor hits the antenna surface, suddenly free carriers are generated and subsequently accelerated by the bias voltage. Depending on the properties of the excitation pulse and the carrier lifetimes, THz radiation can be generated. Although the above mentioned nonlinear generation techniques generally feature a higher emission intensity, one advantage of a photoconductive antenna is its lower noise. This is due to its operation in saturation as compared to the nonlinear non-saturated optical rectification process. Furthermore, the antenna could generate a higher spectral weight at low frequencies down to ~ 0.7 THz which is of interest in the framework of long lived states and had a reasonably high bandwidth up to ~ 3 THz.

B.3.2 Detection of THz radiation by electro-optic sampling

The reflected pulses of freely propagating THz-radiation were measured in an electro-optic crystal via the induced phase modulation on the co-propagating 800 nm gate pulse. In an electro-optic crystal, an external electric field results in a linear change of the refractive index of the material due to the Pockels effect. Because of this, the varying electric field of the

1 Alternatively, more complicated measures such as a tilt of the wavefront or a periodically modulated crystalline structure can be applied but were not used in this work
2 Tera-SED10, Laser Quantum

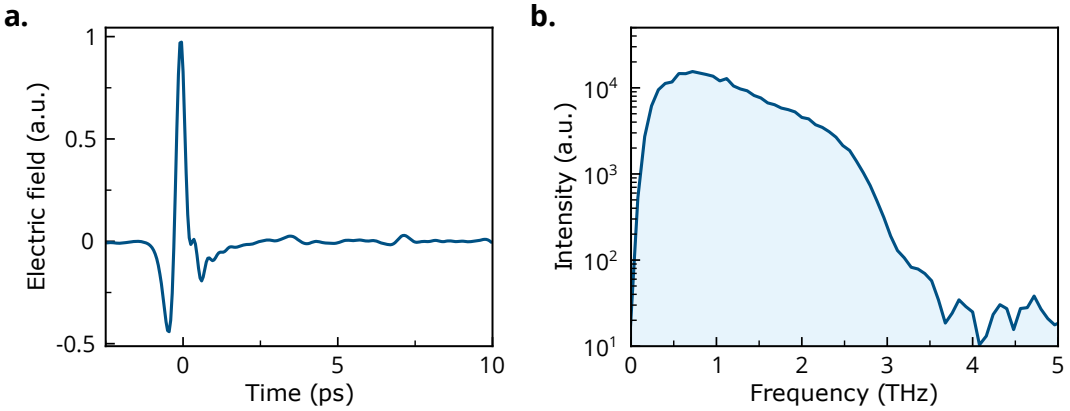

Figure B.5: Terahertz probe pulse in time and frequency domain.
a. Typical time-domain scan of the THz field generated with a photoconductive antenna and reflected from a K_3C_{60} sample at equilibrium. **b.** Spectrum of the THz field amplitude. The spectral content is ranging from about 500 GHz to above 3 THz.

THz pulse induces a phase modulation in the NIR gate beam which is effectively tracking the THz electric field. The polarization state of the gate beam is subsequently analyzed: At first the linearly polarized laser light is converted into circularly polarized light by a $\lambda/4$-waveplate. Afterwards the two perpendicular polarization components s and p are separated by a Wollaston prism and their respective intensity is monitored via a balanced photodetection. If the gate beam carries a phase modulation engraved by the electro-optic interaction with the reflected THz beam, this change in polarization can now be monitored as the difference signal of the balanced photodetector.
In our setups, depending on the bandwidth of the generated THz radiation, we either used 1 mm thick ZnTe, or 0.2 mm thick GaP ⟨110⟩-cut crystals. The ZnTe based setup had a measurement bandwidth ranging from 3.3 meV to 12 meV, while the GaP based one spanned the range between 4.1 meV to 29 meV. The time resolution of both setups is determined by the measurement bandwidth and was ~300 fs and ~150 fs, respectively. Figure B.5 displays typical traces of a raw THz pulse generated by the photoconductive antenna and detected in ZnTe, in time and frequency domain. Since this spectrum was recorded under vacuum, it does not show absorptions from air.

B.3.3 THz beam characterization

The alignment of optics for low intensity THz radiation can be challenging since there are not many ways to track the propagation and check the profile of such beams. Typical semiconductor based camera sensors and also photoluminescent detection cards do not work in this frequency regime and most detectors for thermal radiation are not sensitive enough. Photoconductive THz emitters radiate on the order of 1 nJ of energy per pulse which at a repetition rate of 1 kHz results in a power of 1 μW. This is too low for the detection with thermal or liquid-crystal paper and even commercial detectors and cameras based on thermopile sensors[3] are not sensitive enough. The detection in nonlinear crystals via EOS is possible but a well aligned and time-synchronized system is needed to obtain the high electric THz field and its overlap with the NIR beam for detection. Therefore it is not suitable for general beam characterization in arbitrary positions in the setup. Superconducting bolometers are highly sensitive but typically need cryogenic cooling by liquid helium and are therefore expensive and bulky. However, the recent developments in the field of uncooled microbolometer arrays offer an interesting and less expensive perspective for beam imaging.
Parallel to the work presented in this thesis we developed a sensitive and easy to handle detector based on the pyroelectric effect in $LiTaO_3$. If this material is irradiated with heat, it expands and the resulting deformations of the crystal structure, according to the piezoelectric effect, induce a charge polarization at the interfaces. This polarization can be measured by amplification of the small electric currents that conduct to the electrodes until charge balance is reached. Since the measured current depends on the change in polarization, pyroelectric sensors are sensitive to changes in temperature. While maintaining a small footprint and low cost, the sensitivity of our sensor is quite high (up to 15 V/mW at a noise equivalent power (NEP) of 350 $pW/Hz^{1/2}$) so that it was possible to measure the THz beam even outside of its focus. Figure B.6 a shows a series of beam images that were obtained by scanning the detector in x, y and z direction to obtain the optimum beam quality and focus position. It turned out that already slight misalignments of the parabolic mirror of few arc seconds are sufficient to significantly deteriorate the beam profile (see Fig. B.6 d). This shows the importance of good beam characterization.
To obtain absolute values for the energy per pulse or power of the beam, an absolute calibration of the pyroelectric detector was performed. Therefore, the reflection of the $LiTaO_3$ detection element (that is coated with a black absorber layer) was measured in a commercial Fourier-transform in-

3 e.g. Pyrocams from Ophir with RMS sensitivity of 64 nW/pixel or 1 mW/cm² at 25 Hz

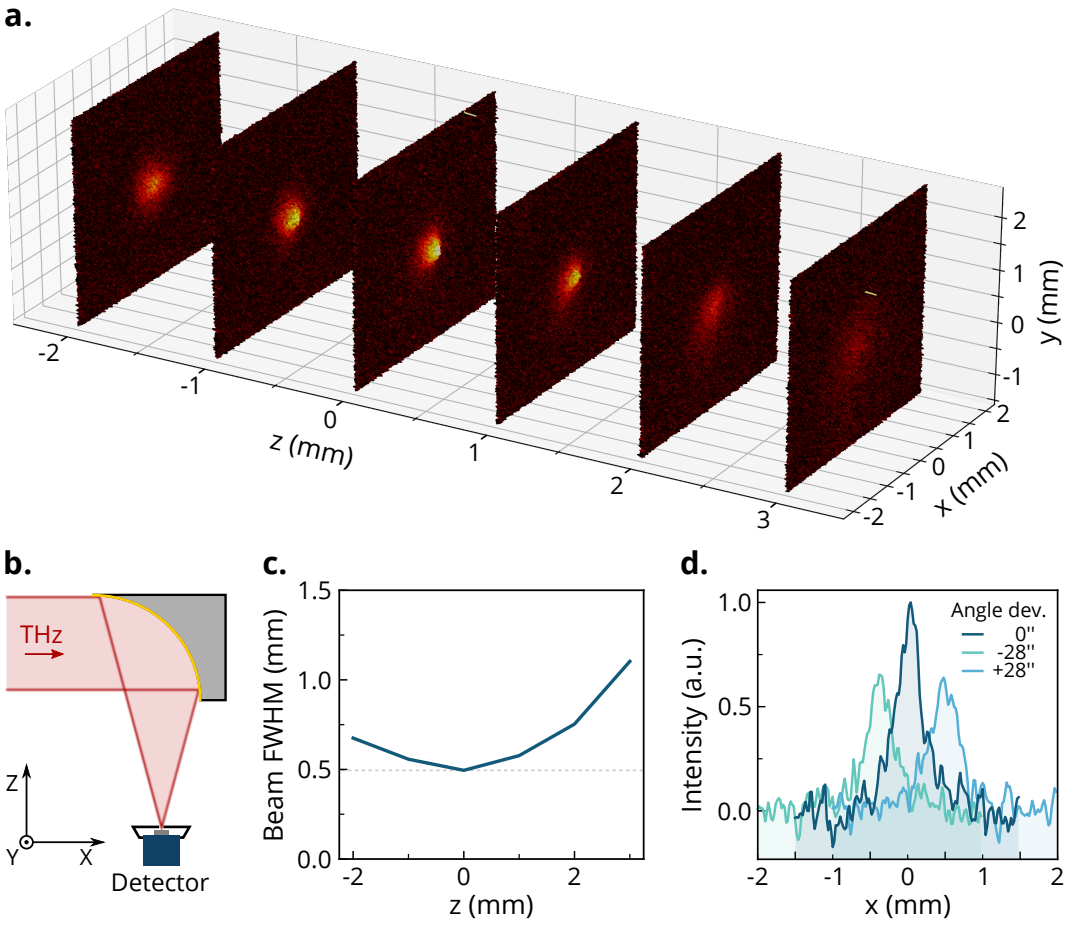

Figure B.6: THz beam imaging with a pyroelectric detector.

a. Map of 6 × 100 × 100 pixels that were scanned with a single channel pyroelectric detector **b.** Schematic of the experimental setup. The detector is scanned in x, y, and z direction through the focus of a parabolic mirror that is irradiated with THz radiation from a photoconductive antenna. To increase the spatial resolution of the detector, a 300 µm diameter pinhole was mounted right in front of the sensing element. **c.** Beam waist of the focused THz radiation obtained by taking the FWHM diameter from the images in a. The minimum size is about 500 µm. **d.** Line traces in x-direction through the center of the beam at the optimal focus z-position for different angles of the focusing parabolic mirror.

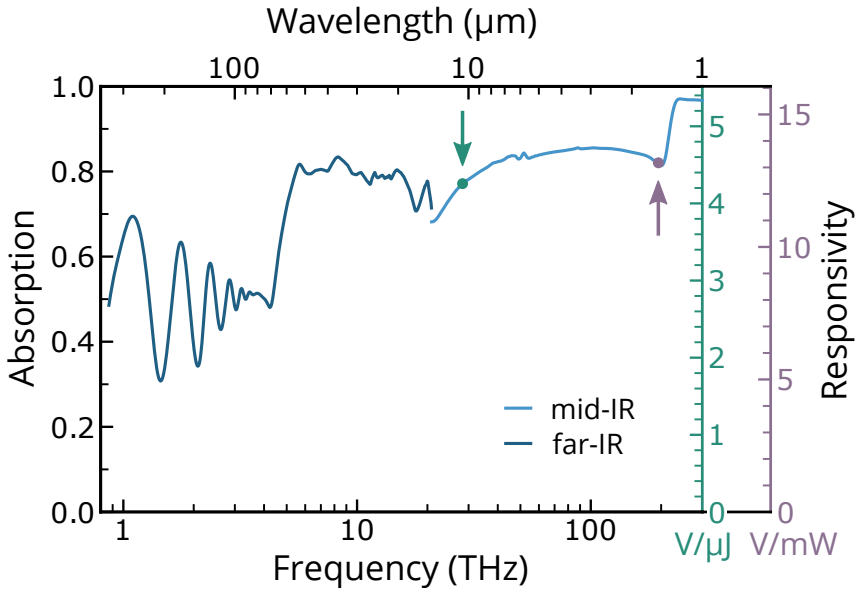

Figure B.7: Absolute calibration of the pyroelectric detector.
The absorption was measured by FTIR with two different detectors. The FIR region (dark blue) was measured with a liquid-helium cooled Si bolometer while in the MIR (light blue) a liquid-nitrogen cooled MCT was used. The arrows indicate the points of calibration as described in the text. The right axes display calibrated output voltage per incident energy in a short pulse in green and per average incident switched power in purple.

frared spectrometer (FTIR)[4]. The reflection was referenced against a gold mirror to obtain the absolute absorption of the detection chip. Figure B.7 shows that over a wide range of about 5 – 200 THz the absorption is flat at about 80 %. Above 200 THz the absorption rises to ~ 98 %. Only in the region below 5 THz, where the wavelength reaches the order of magnitude of the pyroelectric layer thickness, an etalon effect results in interference fringes around 50 % absorption. These are however very well reproducible, so that a calibration of low-energy measurements is also possible. Since the absorbed radiation directly transforms into the strength of the pyroelectric effect, calibration of the detector was performed with the attenuated CO_2 laser at 10.6 μm and with a solid state laser diode at 1.55 μm by comparison with commercial calibrated infrared detectors[5] (cf. arrows in Fig. B.7 and additional green and purple axes). This was possible despite the lower sensitivity of the commercial sensors by adjusting the laser power to the respective highest and lowest measurable range. The nanosecond CO_2 laser pulse results in an impulsive response so that the green calibration refers to an energy per pulse. In contrast, the semiconductor diode is a cw-laser that

4 Bruker Vertex-80 with liquid-helium cooled Si-bolometer in the FIR and liquid-nitrogen cooled MCT in the MIR.
5 Ophir 3A thermopile sensor and PTB calibrated detector from SLT.

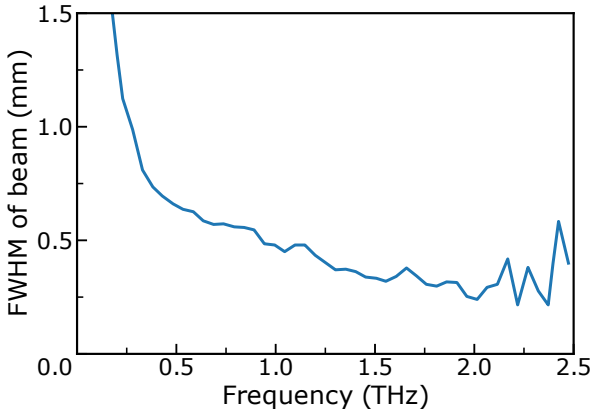

Figure B.8: Exemplary frequency resolved intensity spot size.
The measurement was performed by electro-optic sampling as described in the text. The displayed curve is close to the theoretical spot size limit given by the optics in the experimental setup.

was switched on and off at 20 Hz so that the purple calibration refers to an average power. For any cw-source without on- and off-switching capability the use of an optical chopper gives equivalent results.

For an optimal pump-probe signal, the MIR spot size has to be matched with the low frequencies in the well focused THz spot. Therefore, after beam alignment and characterization but before starting a THz-TDS experiment, it is critical to measure the frequency resolved intensity spot size of the THz beam. This was obtained by 'knife-edge' measurements in which the spectrum of the THz beam is obtained via EOS while a sharp beam blocking edge is introduced in the beam. Thus, the frequency content with respect to the position in the beam can be reconstructed. Figure B.8 shows a typical frequency distribution which is in close proximity to the diffraction limit of the optical setup.

C Data aquisition

C.1 Lock-in amplifier vs. DAQ-Card

For the acquisition of small signals and their differentiation from large backgrounds both a careful experimental design and thorough data acquisition is essential. In this section, on the basis of a typical example in pump-probe spectroscopy, we describe which methods for data acquisition can be used and what advantages and disadvantages they have.
In a pump-probe experiment the recorded parameter during a measurement usually is a voltage trace generated from the amplifier of a photodiode that is being hit by a train of laser pulses. For the balanced detection of an EOS setup the detector signal is a series of pulses whose intensity is proportional to the polarization rotation induced by the reflected THz electric field. Depending on the arrangement and frequency of the pump and probe pulses different information can be obtained from a spike in the corresponding photodiode signal. In the case of pump-probe spectroscopy the following four combinations can be encoded in the signal:

	Probe	Pump
A	on	on
B	off	off
C	on	off
D	off	on

Table C.1: Pump-probe signal combinations

The electric field E of the (THz-) probe pulse is now calculated from the respective signal intensities via

$$E = \mathrm{C} - \mathrm{B}. \tag{C.1}$$

and the pump induced change of the electric field results from

$$\Delta E = \mathrm{A} - \mathrm{C} \tag{C.2}$$

Thus, during an experiment not only signals A and C, which are needed to obtain the pump-induced changes, but ideally all these combinations are

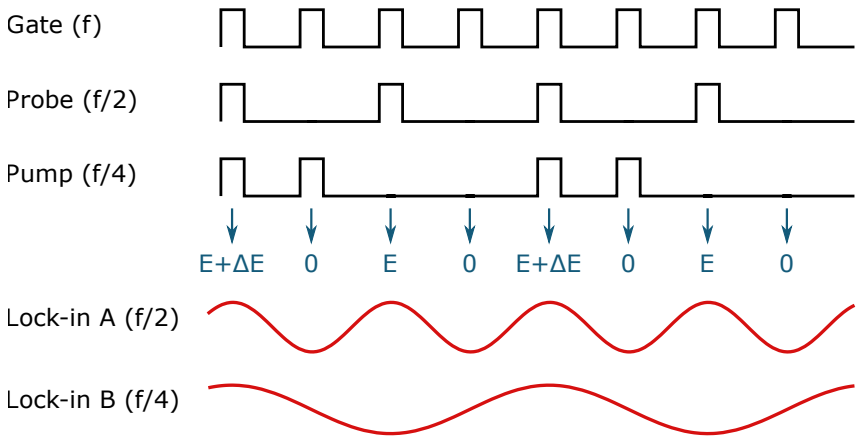

Figure C.1: Detection scheme with two lock-in amplifiers.
The three rows at the top indicate the timings of gate, probe and pump pulses where the frequencies are set to f, $f/2$ and $f/4$ respectively (e.g. by a chopper). The information encoded in each signal is shown in blue for all time slots. The red curves indicate the sinusoidal signal the amplifier locks into at the respective frequencies.

measured repeatedly. This way, potential drifts of the probe electric field can also be monitored and taken in to account.

Since the photodiode signal we want to measure is at a constant frequency, a good option for low-noise detection is provided by a lock-in amplifier (LIA) that is synchronized with the pulse train. However, to record all four types of signals, two LIAs at different frequencies are needed. A good review of this technique (for the example of a biased plasma in air) can be found in [214]. One convenient detection scheme is depicted in Fig. C.1. Here the gating signal has the highest frequency f (e.g. 1 kHz) while pump and probe are reduced in frequency e.g. by a beam chopper or by electronic switching. Accordingly, the two lock-in amplifiers are referenced to the probe and pump frequencies at $f/2$ and $f/4$ but they both get the same photodiode input signal.
At this point it is important to note that a photodiode signal is not necessarily optimal for direct input into a LIA. As this amplifier is trying to measure the amplitude and phase of a *sinusoidal* signal, the shape of the photodiode output is important to obtain reasonable results. This means, the decay time of the photodiode should be smaller but on the order of $1/f$. If the photodetector is much faster, a boxcar integrator should be connected before the lock-in amplifier to obtain a square wave signal that can be easily evaluated.
As can be seen from the red traces in Fig. C.1, when the phase is set cor-

rectly, the two LIAs demodulate different physical quantities from the same photodiode signal. Comparison results in:

$$\text{Output}(\text{LIA}_\text{A}) = \frac{(E + \Delta E) + E}{2} = E + \frac{\Delta E}{2} \tag{C.3}$$

$$\text{Output}(\text{LIA}_\text{B}) = (E + \Delta E) - E = \Delta E \tag{C.4}$$

Therefore, the electric field of the probe and the pump induced changes therein can be calculated by:

$$\Delta E = \text{Output}(\text{LIA}_\text{B}) \tag{C.5}$$

$$E = \text{Output}(\text{LIA}_\text{A}) - \frac{\text{Output}(\text{LIA}_\text{B})}{2} \tag{C.6}$$

This approach is based on the assumption that signal D (probe off, pump on) is always zero, which means that the pump beam does not influence the measurement when there is no probe beam present. Furthermore, it is not possible to distinguish this from the background signal B of the experiment when both pump and probe beam are off.

An alternative approach is to use a data-acquisition card for digitization of the photodetector time-trace signal and subsequent software-based data analysis. This has the advantage of a much higher flexibility of a given experimental setup since with a single acquisition card all possible measurement configurations can be recorded at the same time and the measured quantity only depends on the software and the gating scheme. Figure C.2 shows the measurement principle using realistic frequencies from the CO_2 laser setup. Here, the NIR laser for EOS gating is running at $f = 900\,\text{Hz}$ which is set as a multiple of the CO_2 laser triggered at 18 Hz ($f/50$). The THz probe pulses are generated with a photoconductive antenna biased at $f/2 = 450\,\text{Hz}$. This way, the recorded photodetector time-trace can be divided into a series of experimental configurations consisting of one A event, followed by one B event and 48 times a series of C,B events before the next A event occurs. After data acquisition, the digitized time trace can be sorted according to the different events and a value can be computed each, e.g. by taking the baseline subtracted integral of the detector pulse. Eventually, the values for E and ΔE could be calculated by using Equations C.1 and C.2.

This reveals another advantage of digital data acquisition: It is possible to measure signals that have a huge frequency mismatch. In a lock-in experiment, the low repetition rate of the CO_2 laser would lead to a distribution of the information introduced through the pump pulse at 18 Hz over many higher harmonics (their number depends on the sharpness of the photodiode signal), which effectively suppresses the signal. Since the pump-induced changes are typically on the order of 1 % and lower, it was not pos-

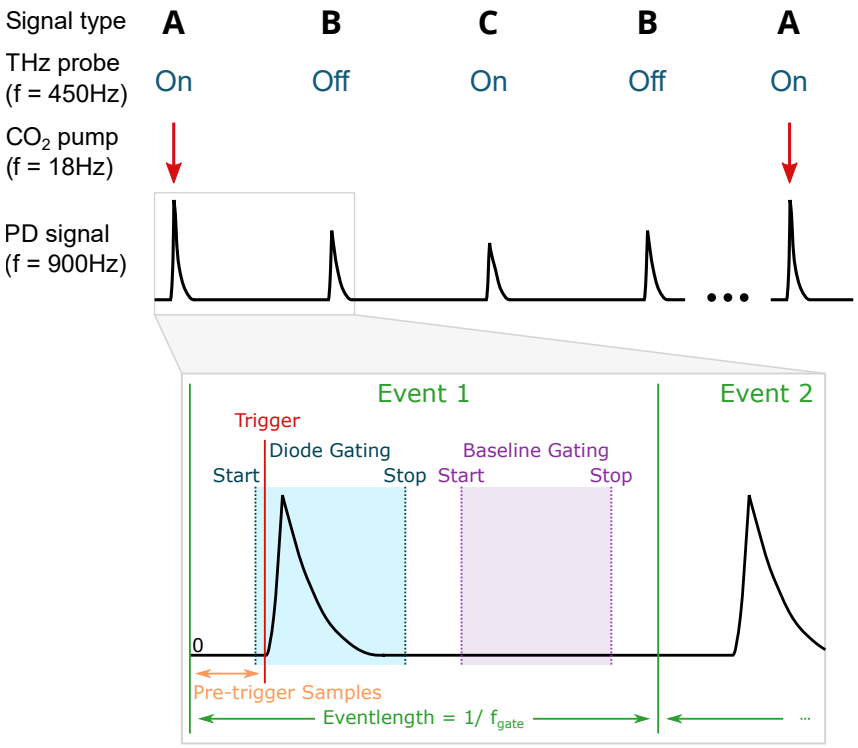

FIGURE C.2: DETECTION SCHEME WITH A DAQ-CARD.
The photodiode (PD) signal of the 900 Hz NIR gating laser is recorded and the resulting pulse train is sliced by software into several events that represent different measurement configurations. These events can be individually evaluated to obtain the targeted physical quantities as described in the text.

sible to reliably resolve the CO_2 laser pump-probe signal with a lock-in amplifier. In contrast, the digital DAQ-approach allowed us to select the desired events already in the time regime, where the information is separated and not distributed over a wide frequency range as in the Fourier domain.
To obtain a similar signal-to-noise ratio comparable to what a LIA is able to measure under optimal conditions, a low input noise of the DAQ-card is the most important factor. However, modern digitizers can reach the noise level of analog LIAs without limitations.[1] Besides that, the digital data-acquisition is also faster since there is no need to wait for stabilization of a transient response. Furthermore, most DAQ-cards feature additional channels that can be simultaneously measured. In the context of balanced detection EOS, this for example enables the measurement of both the photodiodes difference signal, which contains the information on polarization rotation, and the sum signal, revealing an estimate on the lasers power fluctuations. This considerably extends the options for data analyis, e.g. with regard to noise reduction.

C.2 PulseSearchPlus data acquisition and analysis software

Due to the above mentioned advantages of digital data acquisition we chose this approach for the CO_2 laser experiment. This required a software to obtain the targeted physical quantities from the photodiode signal trace. Due to the lack of flexible existing solutions we developed "PulseSearchPlus", a python software that is not only capable to acquire and sort the data but can also perform arbitrary calculations on specific signals. We furthermore integrated the capability to control arbitrary optical delay stages, temperature controllers, component flippers and beam shutters as well as lock-in amplifiers and electronic signal generators. Figure C.3 displays a screenshot of the graphical user interface (GUI), that allows to setup an experiment and to control it in real time.

1 We used an Adlink PCIe-9834 digitizer card with 4 channels, 16-bit, 40 MHz and up to 80 Ms/s at a SNR of 67 dB.

One of the most useful features is the ability to control a measurement not only via the GUI, but also by writing simple XML scripts of type:

```
<commands>
  <listloop values="50,100,300" var="temp">
    <setTemperature
      temperature="temp"
      wait="True" waitTimeSeconds="60" stdDevKelvin="0.25"/>
    <loop from="1" step="2.0" to="10" var="ICWiener">
      <move stage="Pump-Probe" to="ICWiener"/>
      <scan
        displayTab="Advanced Measurements"
        experiment="20-08-31_exampleMeasurement"
        stage="EOS" from="0" to="100" step="0.2"
            conversionID="ps"
        into="[YY-MM-DD_hh-mm-ss]_Temp_[ICWiener]_K"/>
    </loop>
  </listloop>
</commands>
```

This allows to write and reuse scripts for relatively complex measurement routines in a simple and human readable way. The software is structured internally so that all actions are based on such XML commands. This also enables to setup a measurement in the GUI and save the corresponding XML script for future reference.

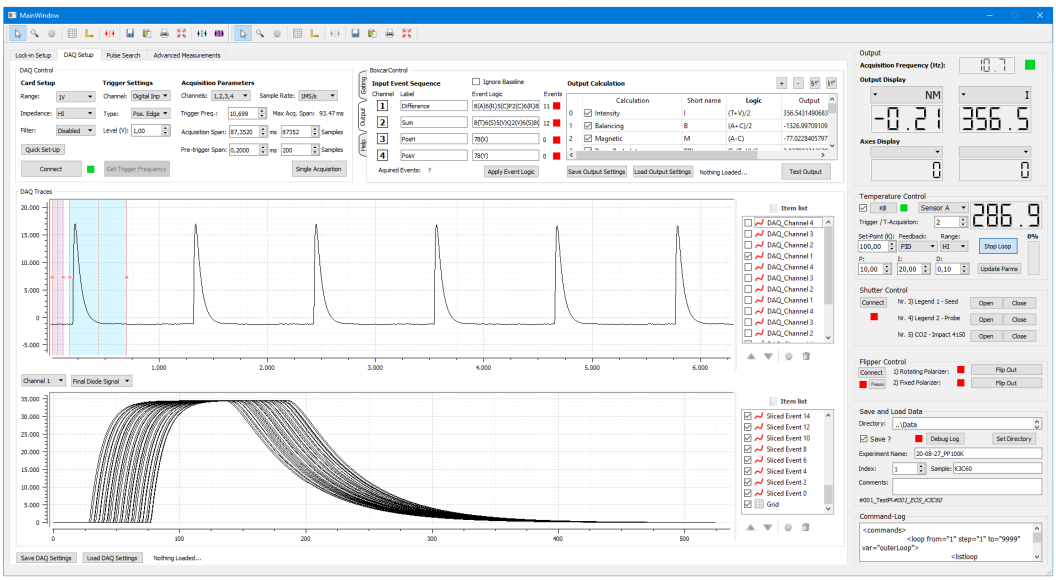

FIGURE C.3: SCREENSHOT OF THE PULSESEARCHPLUS GUI.

D Data analysis for time resolved THz spectroscopy

D.1 Determination of the out-of-equilibrium optical response

The electric field reflected by the unperturbed sample, $E_R(t)$, and the pump-induced changes, $\Delta E_R(t,\tau)$ were simultaneously acquired at each time delay τ by acquiring the electro-optic sampling signals and chopping the pump and probe beams at different frequencies. Simultaneous measurement of the reference electric field $E_R(t)$ and the light-induced changes $\Delta E_R(t,\tau)$ avoids the introduction of possible phase artifacts (e.g. due to long term drifts) and is particularly useful when the measured electric field contains fast-varying frequencies.

$E_R(t)$ and $\Delta E_R(t,\tau)$ were then independently Fourier transformed to obtain the complex-valued, frequency dependent $\tilde{E}_R(\omega)$ and $\Delta\tilde{E}_R(\omega,\tau)$. The photo-excited complex reflection coefficient $\tilde{r}(\omega,\tau)$ was determined by

$$\frac{\Delta\tilde{E}_R(\omega,\tau)}{\tilde{E}_R(\omega)} = \frac{\tilde{r}_R(\omega,\tau) - \tilde{r}_0(\omega)}{\tilde{r}_0(\omega)} \tag{D.1}$$

where $\tilde{r}_0(\omega)$ is the stationary reflection coefficient known from the equilibrium optical response (cf. Chapter 3.1). As the mid-infrared pump penetrated less ($d_{pump} \approx 0.2\,\mu m$) than the THz probe ($d_{probe} \approx 0.6 - 0.9\,\mu m$), these light-induced changes, measured at each pump-probe delay τ, were reprocessed to take this mismatch into account. As the pump penetrates in the material, its intensity is reduced and it induces progressively weaker changes in the refractive index of the sample. A sketch of this scenario is shown in Fig. D.1, which was modelled by considering the probed depth of the material d_{probe} as a stack of thin layers, with a homogeneous refractive index and assuming the excitation profile to follow an exponential decay. By calculating the complex reflection coefficient of this "multilayer" system

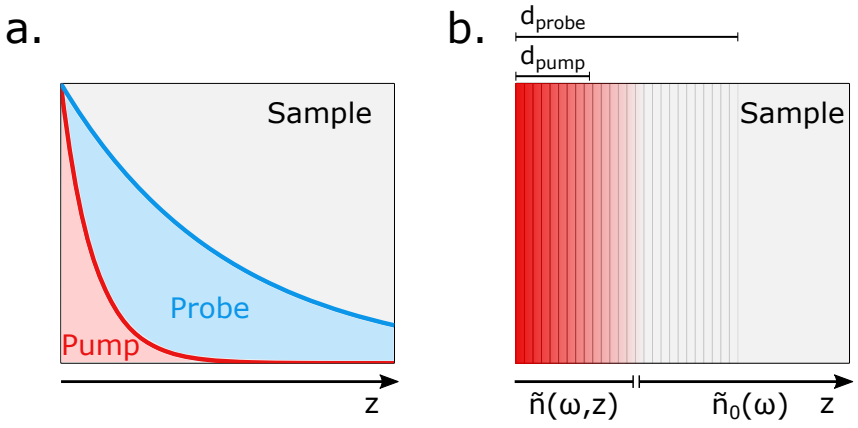

FIGURE D.1: MODELLING PUMP AND PROBE PENETRATION.
a. Schematics of pump-probe penetration depth mismatch. **b.** Multi-layer model with exponential decay used to calculate the pump-induced changes in the complex refractive index $\tilde{n}(\omega, \tau)$ for each pump-probe delay τ. The transition from red to background (grey) represents the decaying pump-induced changes in $\tilde{n}(\omega, z)$.

with a characteristic matrix approach[215], the complex refractive index at the surface $\tilde{n}(\omega, \tau)$, can be self-consistently retrieved. From this, the complex conductivity for a homogeneously transformed volume was obtained as:

$$\sigma(\omega, \tau) = \frac{\omega}{4\pi i}[\tilde{n}(\omega, \tau)^2 - 1] \tag{D.2}$$

The only free parameter in this modelling is the intensity penetration depth of the mid-infrared pump, which is determined by the equilibrium intensity extinction coefficient at the pump wavelength, λ_{pump} / $(4\pi Im(\tilde{n}_0(\omega = \omega_{pump})))$. The probe penetration depth d_{probe} is a frequency- and time-dependent quantity that was self-consistently extracted from the transient response of the material $Im(\tilde{n}(\omega, \tau))$ through the multilayer modelling.

D.2 DRUDE-LORENTZ FITS OF THE OUT-OF-EQUILIBRIUM OPTICAL RESPONSE

The out-of-equilibrium optical response of the photo-irradiated K_3C_{60} pellets was modelled by fitting simultaneously the reflectivity and complex op-

tical conductivity with the same Drude-Lorentz model used to fit the equilibrium response described in Chapter 3.1:

$$\sigma_1(\omega) + i\sigma_2(\omega) = \frac{\omega_p^2}{4\pi}\frac{1}{\gamma_D - i\omega} + \frac{\omega_{p,osc}^2}{4\pi}\frac{\omega}{i(\omega_{0,osc}^2 - \omega^2) + \gamma_{osc}\omega} \tag{D.3}$$

As previously reported in [122], this model is also able to capture the photo-induced superconducting-like response of K_3C_{60} as in the limit of $\gamma_D \to 0$ the Drude conductivity can capture the response of a superconductor below gap:

$$\sigma_1(\omega) + i\sigma_2(\omega) = \frac{\pi}{2}\frac{N_s e^2}{m}\delta[\omega = 0] + i\frac{N_s e^2}{m}\frac{1}{\omega} + \frac{\omega_{p,osc}^2}{4\pi}\frac{\omega}{i(\omega_{0,osc}^2 - \omega^2) + \gamma_{osc}\omega} \tag{D.4}$$

Here N_s, e, and m are the superfluid density, electron charge, and mass, respectively. Furthermore, the transient nature of a photo-induced superconductor having a finite lifetime appears as a broadening of the zero-frequency Dirac delta [216]. The data acquired with broadband THz probe (see Fig. 5.2 of the main text) were fitted by optimizing iteratively the parameters of both the Drude (ω_p and γ_d) and mid-infrared absorption band ($\omega_{p,osc}$, $\omega_{0,osc}$, and γ_{osc}). On the other hand, data acquired with narrower probe bandwidths (cf. Fig. 5.4) were fitted also by keeping only ω_p and γ_d free to vary. Importantly, in both cases the fits yielded similar Drude parameters and we chose to only optimize the Drude parameters for these data as the probed frequency range does not overlap with the mid-infrared oscillator.

Figure D.2 shows representative fits to data measured at 100 K for three different time delays of −150 ps, −100 ps, and 10 ps. The fitting was performed on transient conductivity spectra for each time delay shown in Fig. 5.9 b. The obtained parameters were used to calculate the zero-frequency extrapolated optical conductivity σ_0 and from this the "optical resistivity" ρ_0 as:

$$\rho_0 = 1/\sigma_0 = \lim_{\omega \to 0} 1/\sigma_1(\omega) \tag{D.5}$$

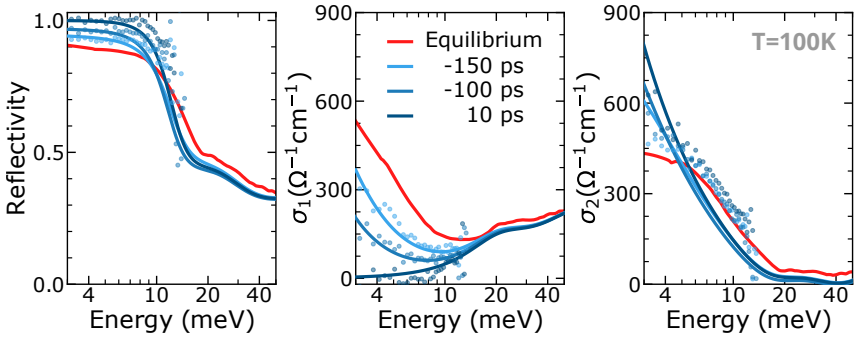

Figure D.2: Drude-Lorentz fits to the optical conductivity for different time delays.

Measured optical properties (reflectivity, real, and imaginary part of the optical conductivity) of K_3C_{60} measured at a temperature of 100 K at equilibrium (red curve) and at three different time delays of −150 ps, −100 ps, 10 ps (blue filled symbols). These data were acquired with a pump-pulse duration of 200 ps and by definition the time delay is zero when the pulse ends (cf. Fig. 5.5 b). The solid lines are Drude-Lorentz fits to the transient optical properties.

D.3 Influence of uncertainties in the equilibrium optical properties

The error of the reconstructed light induced transient optical response of K_3C_{60} is primarily determined by uncertainties in: (i) the measured values of the normalized change of the electric field $\Delta E/E$, (ii) the pump penetration depth d_{pump} , which is used to reconstruct the $\tilde{n}(\omega, z)$ profile in the multilayer model (see Appendix D.1), and (iii) the absolute value of the measured equilibrium reflectivity, which is typically smaller than 2 %. To display the effect of these uncertainties we display transient optical properties reconstructed from the $\Delta E/E$ values measured 1 ns after photo-excitation at a temperature $T = 100$ K. In Figs. D.3 a, D.3 b, D.3 c, we show as shaded colored bands the propagated uncertainties introduced by ±5 % variations in $\Delta E/E$, ±10 % and ±20 % uncertainties in the value of the pump penetration depth, and a ±2 % error in the value of the equilibrium reflectivity $R(\omega)$ respectively. Importantly, all features of the light induced response such as the gap opening in $\sigma_1(\omega)$ and the presence of a divergence in $\sigma_2(\omega)$ are not affected by any of these uncertainties.

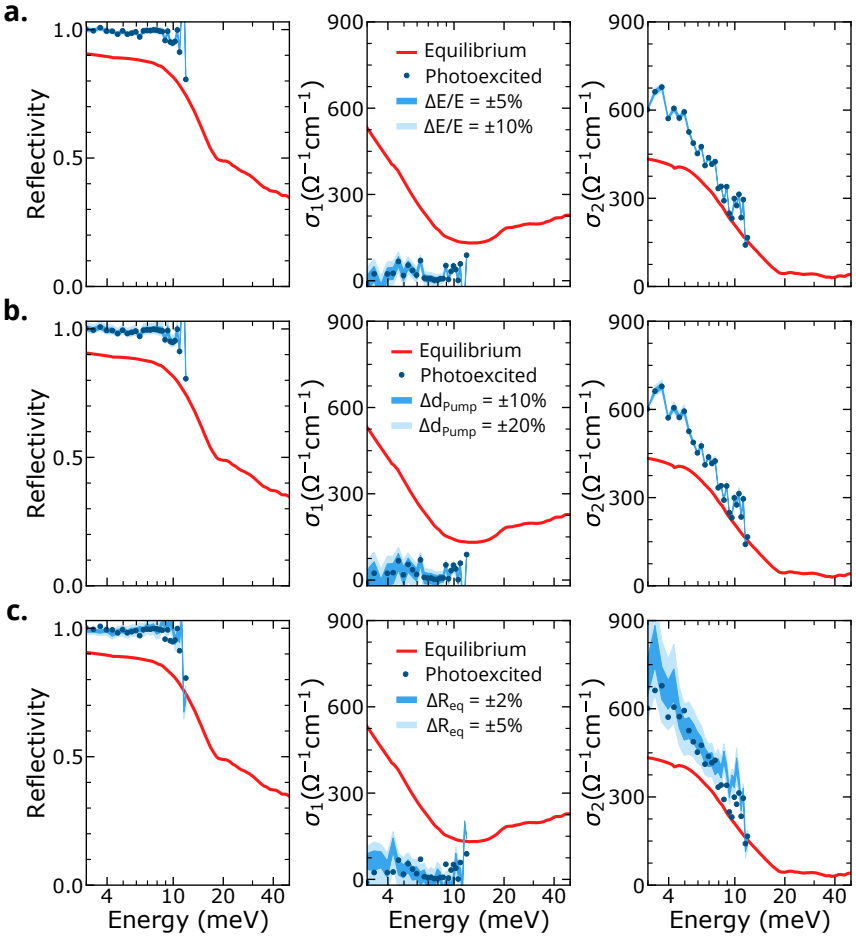

Figure D.3: Errors in the transient optical properties caused by different sources of uncertainty.

The propagated error on the optical properties is shown as light and dark blue coloured bands and was propagated from **a.** ±5 % and ±10 % uncertainty in the measured $\Delta E/E$ **b.** ±10 % and ±20 % uncertainty in the value of the pump penetration depth and **c.** ±2 % and ±5 % uncertainty in the value of the equilibrium $R(\omega)$. All measurements (red curves at equilibrium and blue dots 1 ns after photoexcitation) were carried out at $T = 100$ K. Photoexcitation was performed in the same conditions as the data presented in Fig. 5.4.

E TIME-RESOLVED ELECTRICAL TRANSPORT MEASUREMENTS

E.1 SAMPLE PREPARATION

For time-resolved electrical transport measurements, pellets of K_3C_{60} were integrated into a sample carrier with patterned microstrip transmission lines. Figure E.1 shows a picture of the sample carrier and a sketch of its cross-section. The four Ti(10 nm)/Au(270 nm) microstrip structures were grown using a combination of e-beam evaporation, laser-lithography, and lift-off processing, on a 500 µm thick diamond substrate, transparent to the 10.6 µm radiation. The wave impedance of the transmission lines was adapted to 50 Ω. A pellet of 1 mm diameter and ~75 µm thickness was made from K_3C_{60} powders with a pellet die and a manual press. All the sample handling operations were carried out in an Argon filled glove box with < 0.1 ppm O_2 and H_2O to prevent sample oxidation. To ensure good electrical contact between the polycrystalline pellet and the transmission lines at low temperatures, a layer of 2 µm thick indium was deposited on the inner parts of the Au transmission lines by an additional lithography and lift-off step. To reproducibly position the pellet in the center of the four microstrips, a ~50 µm thick layer of photoresist (SU8) with a 1 mm central bore was deposited. The K_3C_{60} pellet enclosed in the photoresist layer, was then capped with a 500 µm thick sapphire plate and sealed with vacuum compatible glue. This assembly was placed on a copper holder and then installed at the end of a commercial LHe cold-finger, in order to cool the K_3C_{60} pellets down to a base temperature of 5 K. The microstrips were terminated to SMP connectors to connect them to 50 Ω wave impedance coaxial cables that are thermally anchored on the cold finger, and routed to the outside of the cryostat.

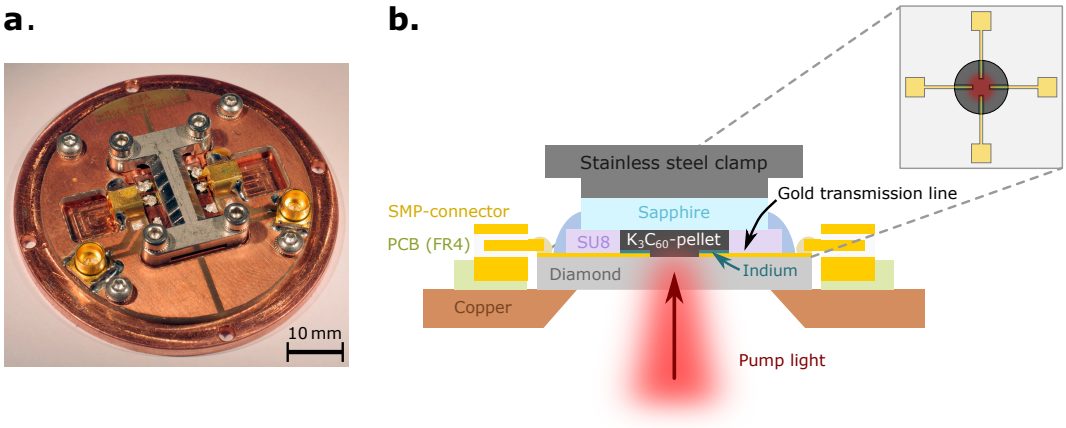

FIGURE E.1: K_3C_{60} SAMPLES FOR ELECTRICAL TRANSPORT.
a. Photograph of the sample carrier used for transport measurements. **b.** Schematic section-view of the K_3C_{60} sample assembly (not to scale). The pulsed mid-infrared excitation reaches the sample from below. The upper right panel shows a sketch of the electrode geometry similar to the one used in both four- and two-terminal measurements.

E.2 CALIBRATION OF TWO-TERMINAL MEASUREMENTS

Standard four-terminal resistance measurements (Fig. E.2 a) were performed on K_3C_{60} pellets encapsulated in the high-frequency sample carrier using a lock-in technique with a sinusoidal excitation current of amplitude $I_{source} = 1\,\mu A$ at a frequency of 300 Hz. While this technique provides accurate values of the low frequency sample resistance R_{sample} it could only be applied up to frequencies of a few MHz due to the limited bandwidth of the high input impedance differential amplifiers as well as parasitic capacitances in the circuit. The lifetime of the light-induced superconducting state is several nanoseconds, hence four-terminal measurements are too slow to probe transport properties on these time scales. To overcome this issue, we performed high-frequency two-terminal resistance measurements. These measurements were conducted by launching a 1 ns long voltage pulse from a commercial pulse generator through the microstrip transmission lines and the K_3C_{60} pellet in the sample carrier. A gated integrator was then used to detect the amplitudes of the injected voltage pulse $V_{in}(t)$, and of the one transmitted through the sample $V_{out}(t)$. An equivalent circuit diagram of this two-terminal measurement is shown in Fig. E.2 b. These measurements allow to retrieve the resistance $R^*_{2P} = R_{sample} + R_{C1} + R_{C2}$ which includes contributions from wiring and contact resistances. As the injected voltage pulse propagates, it can be reflected at the input and output terminals of R^*_{2P} due to a possible impedance mismatch. To account for this, it is convenient to describe the propagation of the pulse through the network using the

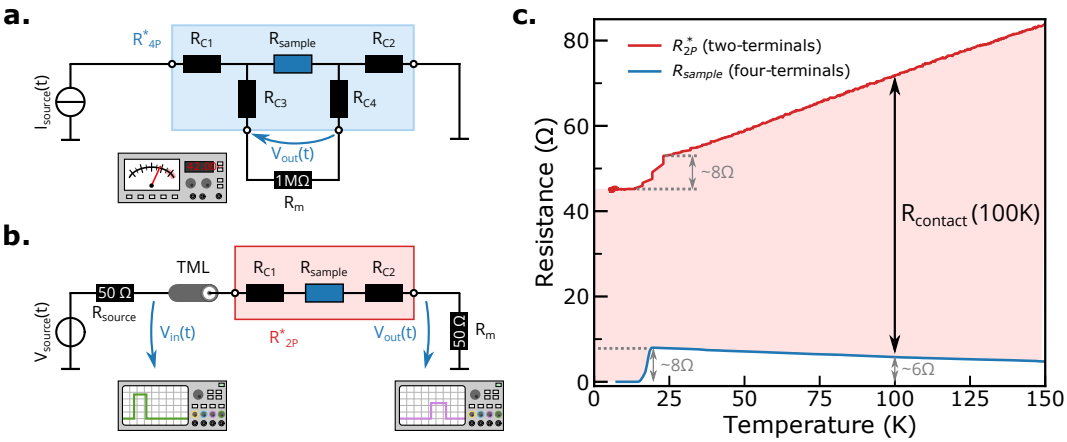

FIGURE E.2: CALIBRATION OF ELECTRICAL TRANSPORT MEASUREMENTS.

a. Equivalent circuit of a four-terminal resistance measurement. A constant amplitude sinusoidal current is injected into R_{sample} through the contact resistances R_{C1}, and R_{C2}. The voltage drop across R_{sample} is detected by a high input impedance lock-in amplifier through the contact resistances R_{C3} and R_{C4}. The sample resistance can be directly retrieved as V_{out} / I_{source}. **b.** Equivalent circuit for two-terminal measurements. The sample with intrinsic resistance R_{sample} and contact resistances R_{C1} and R_{C2} is connected via two terminals. TML indicates the coaxial cable which acts as a transmission line for high frequency signals. **c.** Temperature dependent resistance measured in a two- and four-terminal measurement. The temperature-dependent contact resistance $R_{contact} = R_{C1} + R_{C2}$ is displayed as red shading inbetween the graphs. Both measurements were performed on the same type of pellet with identical preparation procedure and equal electrode geometry.

two-port scattering matrix formalism [217], from which the total resistance of the sample R^*_{2P} can be retrieved as:

$$R^*_{2P} = R_{sample} + R_{C1} + R_{C2} = 2\left(\frac{V_{in}}{V_{out}} - 1\right)R_m. \tag{E.1}$$

Here, V_{in} and V_{out} are the amplitudes of the injected pulse and of the pulse transmitted through the sample while $R_m = 50\,\Omega$ is the input impedance of the gated integrator used for signal detection. This result was quantitatively verified by simulating the equivalent circuit with the software QucsStudio starting from measured values of the elements in the circuits (see Section F for more details). Extracting R_{sample} from R^*_{2P} requires knowledge of the contact resistance from the low-frequency four-terminal measurements. In order to calibrate the contact resistance $R_{contact} = R_{C1} + R_{C2}$ we compared the temperature dependence of the resistance R^*_{2P} (measured in the pulsed two-terminal geometry, red curve in Fig. E.2 c) to that of the sample resistance R_{sample} (measured in the four-terminal geometry, blue curve in Fig. E.2 c). In both measurements, the equilibrium superconducting transition of K_3C_{60} is observed as a drop in the measured resistance of ~8 Ω as the sample becomes superconducting. Hence, the two- and four-terminal measurements are equally sensitive to changes in R_{sample} and are only offset by the contact resistance $R_{contact}$ (red shaded area in Fig. E.2 c), allowing us to extract R_{sample} from the high-frequency two-terminal measurements. The time-resolved resistance measurements of the photo-irradiated K_3C_{60} pellet shown in Fig. 5.9 a were performed at 100 K by repeating the pulsed two-terminal measurements at different time delays after photoexcitation. This was achieved by electronically synchronizing the pulse generator that provided the probe voltage pulse to the laser system. These measurements yielded the total resistance R^*_{2P}, from which the contact resistance $R_{contact}(100\,\mathrm{K}) = 66\,\Omega$ was subtracted to obtain the time-dependent resistance of the K_3C_{60} sample alone. Note that the change of the resistance in the time-resolved experiment at $T = 100\,\mathrm{K}$ is $\Delta R = 6\,\Omega$ (cf. Fig. 5.9), which is what is quantitatively expected from the DC four-terminal measurement if the sample turns superconducting at this temperature.

E.3 Modeling time-resolved electrical transport measurements

To ensure that the experimental procedure used to extract the sample resistance (described in Appendix E) was not affected by additional contribution due to stray impedances we have modelled the experimental setup using the software QucsStudio, that simulates propagation of electrical signals in the time domain.
The simulations were performed according to the setup described in Fig. E.3 a, that matches closely the experimental setup. A 1 ns long voltage pulse generated by a commercial pulse generator, was split in two identical replicas by a power divider; one was sent through the sample while the other was used as a reference. Both pulses were sampled with a real-time oscilloscope with 20 GHz bandwidth and 80 GSamples/s. The recorded signals are referred to as $V_{out}(t)$ and $V_{ref}(t)$ in the following. Figure E.3 d shows the $V_{out}(t)$ and $V_{ref}(t)$ time traces (red and blue lines) measured at 30 K, and corresponding simulations (green and yellow lines) of the equivalent circuit diagram shown in Fig. E.3 a, where the two-terminal resistance R^*_{2P} is simply modelled by two contact resistors (R_{C1} and R_{C2}) and the intrinsic sample resistance (R_{sample}). Remarkably, all peak positions and amplitudes are reproduced with good agreement. The $V_{ref}(t)$ trace, shows the injected pulse at ~0 ns and a later pulse, around ~13.5 ns which is a reflection from the sample arm. The $V_{out}(t)$ trace shows a pulse appearing at ~8 ns which is the injected pulse after propagation through the sample and contacts. Because of the voltage drop across R^*_{2P} it has lower amplitude compared to the injected pulse.
As mentioned in Section E, the propagation of voltage pulses through this network can be described by applying the two-port scattering matrix formalism to retrieve the sample resistance R_{sample} directly from the amplitude of the reference (V_{ref}) and transmitted ($V_{out}(t)$) pulses. Thus we can use formula E.1 and replace V_{in} with V_{ref}.
For an accurate measurement of R^*_{2P} it is important that the amplitude of the reference and transmitted pulses is not changed by parasitic effects. To evaluate the influence of possible parasitic capacitances at the contacts, that might short the contact resistance at high frequencies, we simulated the extended equivalent circuit diagram for R^*_{2P} shown in Fig. E.3 c. We estimated 2 pF and 2 nH as realistic upper limits for the respective capacitance and inductance values. The results of these simulations are compared to those in the ideal case in Fig. E.3 e. The additional stray impedances resulted in voltage spikes on top of the nanosecond pulses, that are stronger in amplitude than the deviations observed between the

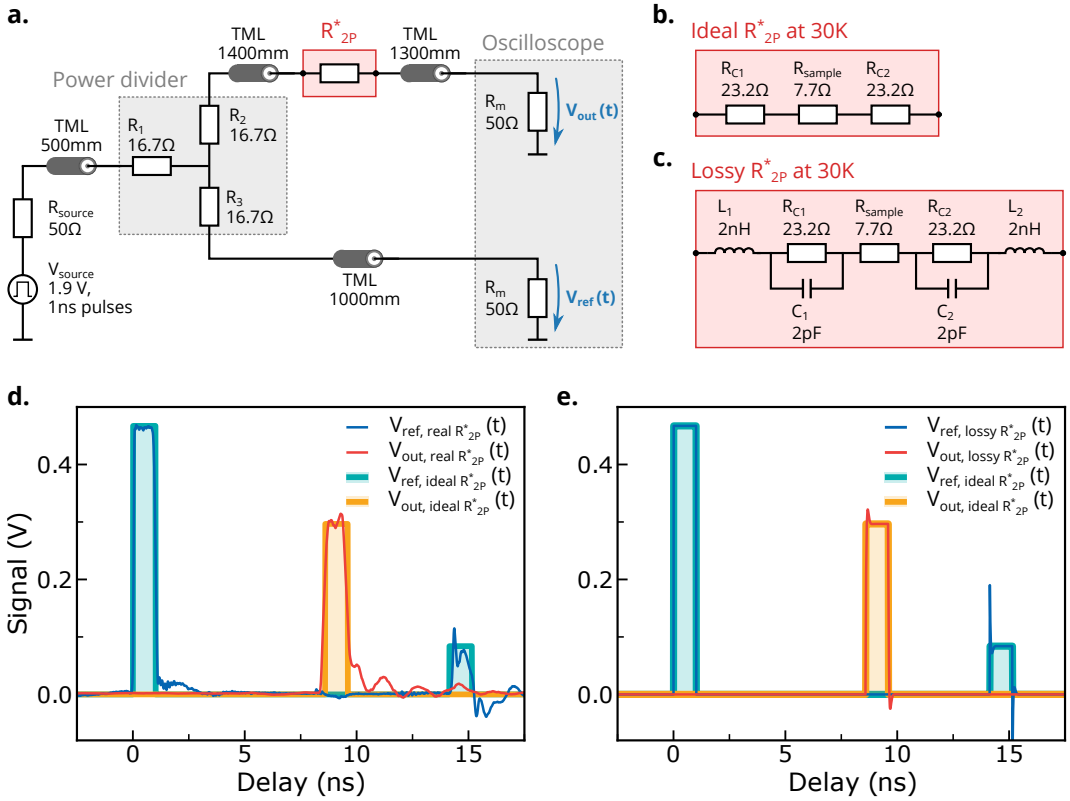

FIGURE E.3: MODELING ELECTRICAL TRANSPORT MEASUREMENTS.

a. Schematic description of the setup for measuring the unknown R^*_{2P} resistance in a two-terminals configuration. TML denotes HF compatible microstrip transmission lines. Their length was adjusted so that pulses are not overlapping when measured on the oscilloscope. **b.** Ideal equivalent circuit diagram for R^*_{2P} consisting of two contact resistors (R_{C1} and R_{C2}) and the intrinsic resistance of the sample (R_{Sample}). **c.** Lossy equivalent circuit diagram for R^*_{2P} considering a capacitive as well as inductive component of the contacts. **d.** Time traces for $V_{ref}(t)$ (blue) and $V_{out}(t)$ (red) measured at a temperature of 30 K without photo-excitation and corresponding numerical simulations (green and yellow lines) performed under the assumption of an ideal R^*_{2P}. The measured oscillations at the base of the first pulse in $V_{out}(t)$ and the second pulse in $V_{ref}(t)$ are caused by residual reflections not relevant to our analysis. **e.** Comparison of two simulations with ideal and lossy R^*_{2P}. Parasitic capacitances and inductances of 2 pF and 2 nH were introduced resulting in voltages spikes that are bigger than any deviation observed between the measurement and the ideal case simulation.

measured signals and simulations in the ideal case. A similar simulation (not shown) with additional parasitic capacitances to ground yielded comparable results, the only differences were due to the lower bandwidth of the circuit. The good agreement between the ideal simulations and our measured signals strongly suggests that capacitive and inductive contributions to the contact resistance are negligible. More importantly, these putative contributions do not lead to a significant change of the average pulse amplitude which is used to calculate the resistance.

F Simulations of the superconducting order parameter relaxation

In the following, we describe a phenomenological theory for the relaxation of the superconducting order parameter following laser excitation. This model is similar to phenomenological models used for cuprate superconductors [218–220], shown to be capable to accurately reproduce a surprising amount of the available experimental data on these materials. As argued in the main text, in a situation where preformed pairs exist in the material above T_c, and superconductivity is destroyed by phase fluctuations, a laser-induced synchronized state can decay very slowly.

We considered a phenomenological Ginzburg-Landau model of the superconducting order parameter on a two-dimensional square lattice with 100×100 sites and periodic boundary conditions. The order parameter at site m is denoted $\psi_m(t) = |\psi_m| e^{i\phi_m}$, where $|\psi_m|$ is the local amplitude and ϕ_m the local phase. As in Ref. [218], we assumed that the order parameter is microscopically related to the local singlet pairs, i.e. $\Psi_m \sim \langle c_{m\downarrow} c_{m\uparrow} - c_{m\uparrow} c_{m\downarrow} \rangle$, but no assumptions were made on how these pairs are generated microscopically. The free energy potential was chosen as:

$$F = \sum_m \left(A |\psi_m|^2 + \frac{B}{2} |\psi_m|^4 \right) + \frac{C}{2} \sum_{<m,n>} |\psi_m| |\psi_n| \cos(\phi_n - \phi_m), \tag{F.1}$$

where the summation $\langle m, n \rangle$ runs over neighboring sites. The first term describes a local potential, which determines the equilibrium Cooper pair density. This theory contains three free parameters A, B, and C which we specify below. We chose the parameters such that the mean local order parameter is given by $\langle |\psi_m| \rangle = \sqrt{-A/B} = \sqrt{1 - T/T_0}$, where T_0 is the temperature at which Cooper pairs start to form in the material. The second term in the free energy potential couples adjacent sites and determines the phase stiffness. A positive parameter C means it is energetically favorable for the phases to align. The strength of this phase coupling controls the temperature scale, at which the relative phase of pairs on different sites can lock and the condensate achieves phase coherence. Here we focused on the situation where $C \ll |A|, B$, i.e. we consider a gas of localized bosons which weakly interact with one another. The weak interaction can lead to condensation only at low

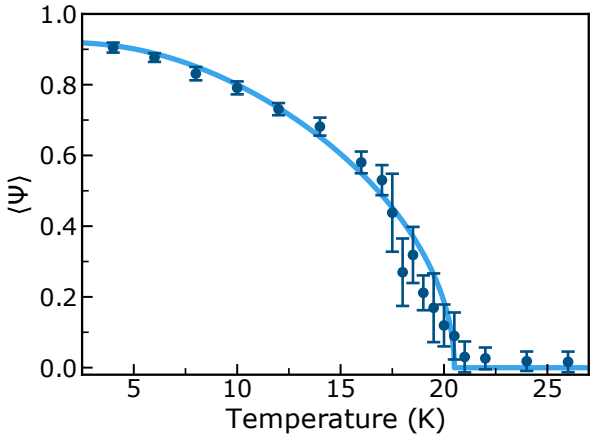

Figure F.1: Temperature dependence of the superconducting order parameter. The amplitude of the average superconducting order parameter $\langle|\psi_m|\rangle$ was calculated from the Ginzburg-Landau model described in the text and shows a transition at $T_c \simeq 20\,\mathrm{K}$. The light blue line is a guide to the eye.

temperatures. Importantly, the model reproduces correctly the equilibrium phase transition at $\simeq 20\,\mathrm{K}$ as displayed in Fig. F.1.

To describe the nonequilibrium relaxation, we set the superconducting gap $2\Delta_0 \sim 10\,\mathrm{meV}$ as observed in the transient optical measurements. To describe the relaxation of the photo-induced superconducting state we simulated the dynamics using the time-dependent Ginzburg-Landau (TDGL) equation:

$$\tau \partial_t \psi_m(t) = -\frac{\delta F\left(\psi_m, \psi_m^*\right)}{\delta \psi_m^*} + \eta_m(t) \tag{F.2}$$

where $\eta_m(t)$ is a random force describing random thermal fluctuations and obeys $\langle \eta_m^*(t)\eta_{m'}\left(t'\right)\rangle = 2\tau\frac{k_B T}{f\Delta_Q}\delta_{m,m'}\delta\left(t-t'\right)$, where f is a dimensionless parameter which is introduced below. Here τ is a free parameter that determines the characteristic time scale at which the dynamics evolve and that needs to be determined from a fit to the experiments. We found that a good match between the measurements and simulated relaxation is obtained for $\tau \sim 1.5\,\mathrm{ps}$ and $f = 6000$ (see Fig. 6.6 b).

Discussion

If the order parameter is driven away from its equilibrium value, the time evolution due to the derivative of the free energy potential gives rise to an exponential decay back to its unperturbed value. For small perturbations, and neglecting the spatial variation of the order parameter, we linearize the TDGL equation as:

$$\tau \partial_t \psi_m(t) \simeq -|A|\psi_m(t), \tag{F.3}$$

to obtain the amplitude relaxation time

$$T_{\text{amplitude}} = \frac{\tau}{|A|} \tag{F.4}$$

This sets the time scale for relaxation driven by the deterministic part of the TDGL equation.

As our model considers a situation where incoherent Cooper pairs survive above the critical temperature, another relaxation time scale emerges naturally. It stems from the thermal diffusion of local phases taking place at the minimum $\sqrt{-A/B}$ of the local free energy potential. Below the critical temperature, the relative phases are kept fixed due to the coupling C. But above T_c, this attraction is overpowered by thermal noise and phase coherence is lost. To assess the timescale on which this should take place, we consider a high temperature regime where fluctuations dominate the dynamics,

$$\tau \partial_t \psi_m(t) \simeq \eta_m(t). \tag{F.5}$$

We consider the noise as $\eta_m = \eta_1 + i\eta_2$, where η_1 and η_2 are real-valued independent random variables, respectively. We note that $\langle \eta_1(t)\eta_1(t')\rangle = \langle \eta_2(t)\eta_2(t')\rangle = \tau\frac{k_B T}{f\Delta_0}\delta(t-t')$ and $\langle \eta_1\eta_2\rangle = 0$. Assuming that the amplitude has reached its equilibrium value $\langle|\psi_m|\rangle = \sqrt{1-T/T_0}$, we obtain a time evolution equation for the phase:

$$\sqrt{1-\frac{T}{T_0}}\tau\partial_t\phi_m(t) = \eta_2\cos(\phi_m) - \eta_1\sin(\phi_m) = \eta'(t). \tag{F.6}$$

In the second equality, we recognize that the noise term can again be written as a random noise η' with the same variance as η_1 and η_2. Consequently, we find that the phase undergoes a one-dimensional random walk induced by the random force η'. The diffusion time scale can be found by solving the associated Fokker-Planck equation for the probability distribution of ϕ_m (see e.g. Ref. [221]). Solving this diffusion equation, we find the phase relaxation timescale:

$$T_{\text{phase}} = \frac{f\Delta_0(1-T/T_0)}{k_B T}\tau. \tag{F.7}$$

We note that in this case, it is determined by the ratio between the superconducting gap Δ_0 and the thermal energy $k_B T$ of the environmental degrees of freedom.

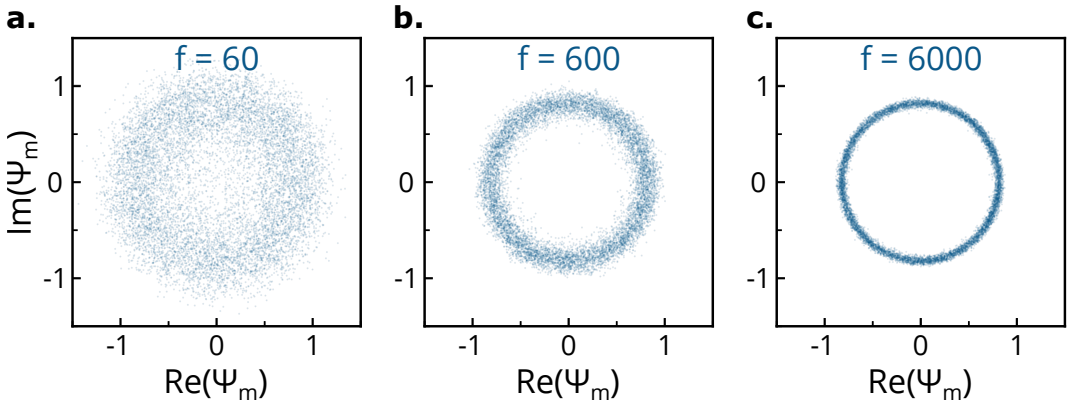

Figure F.2: Snapshots of the on-site order parameter Ψ_m.
Ψ_m is shown in the complex plane after time evolution up to $t = 10^3 \frac{\tau}{|A|}$. The simulations were performed at $T = 100\,\mathrm{K}$ using three different f parameter values of 60, 600, and 6000 (left to right). The on-site order parameters Ψ_m are initialised in a synchronised state, $\Psi_m(t = 0) = \sqrt{-A/B}$ and then relaxed according to the TDGL equation described in the text.

The ratio between phase and amplitude relaxation time is proportional to the steepness of the free energy potential,

$$\frac{T_{\text{phase}}}{T_{\text{amplitude}}} \propto f \tag{F.8}$$

If the free energy potential is shallow and amplitude fluctuations are large, the ratio can be close to one. If phase fluctuations dominate, phase relaxation becomes much slower than the amplitude relaxation. Furthermore, if the temperature of the environmental degrees of freedom in which the relaxation takes place, is close to the 'pseudogap' temperature T_0, the ratio becomes smaller. Figure F.2 displays snapshots of the phase distribution for different values of f. When f = 60, the potential is very shallow and the phases relax to a broad distribution with vanishing average amplitude. Clearly, in such a situation there can be no distinction between phase and amplitude relaxation. However, when f increases, amplitude fluctuations are suppressed and the local order parameters are confined to a narrow ring with radius $\sqrt{-A/B}$. In such a situation, phase relaxation becomes the dominant relaxation pathway and a synchronized state can survive much longer.

Parametrization

We write the coefficients of the free energy as:

$$
\begin{aligned}
A &= -\frac{\Delta_0}{k_B T_0}\left(1 - \frac{T}{T_0}\right) \\
B &= \frac{\Delta_0}{k_B T_0} \\
C &= -\frac{c}{f}\frac{\Delta_0}{k_B T_0}
\end{aligned}
\tag{F.9}
$$

where we assume that the relevant energy scale is $\Delta_0/k_B T_0$. Here we assume that A changes its sign at a very large temperature $T_0 = 300\,\mathrm{K}$, i.e. a local Cooper pair density can survive up to room temperature. In addition, we introduce the dimensionless parameter f, which determines the relative strength of amplitude fluctuations. This parameter determines the relative speed of the amplitude and phase relaxation: An increase of f reduces the absolute amplitude of thermal fluctuations as well as the pair coupling constant C, such that the superconducting transition temperature remains constant. Finally, the parameter $c = 4.5$ is adjusted to induce a superconducting transition at $\simeq 20\,\mathrm{K}$ at equilibrium (see Fig. F.1).

Frequently Used Acronyms

ASE	Amplified spontaneous emission
BBO	Beta barium borate
BSCO	Bismuth strontium calcium copper oxide ($Bi_2Sr_2Ca_{n-1}Cu_nO_{2n+4+x}$)
CDW	Charge density wave
CMR	Colossal magnetoresistance
DECP	Displacive excitation of coherent phonons
DFG	Difference frequency generation
DMFT	Dynamical mean field theory
FIR	Far-infrared radiation
FTIR	Fourier-transform infrared spectrometer
HRFZ-Si	High resistivity float zone silicon
IRS	Ionic raman scattering
ISRS	Impulsive stimulated raman scattering
LIA	Lock-in amplifier
LSCO	Lanthanum strontium coppper oxide ($La_{2-x}Sr_xCuO_4$)
MCT	Mercury cadmium telluride (HgCdTe)
MIR	Mid-infrared radiation
NIR	Near-infrared radiation
OPA	Optical parametric amplifier
PDW	Pair density wave
PPLN	Periodically poled lithium niobate
QCL	Quantum cascade laser
SFG	Sum frequency generation

SHG	Second harmonic generation
TCR	Temperature coefficient of the resistivity
TDFS	Transient depletion field screening
TDGL	Time-dependent Ginzburg-Landau
TDS	Time-domain spectroscopy
THz	Tera hertz
UV	Ultra violet
VIS	Visible
WLG	White light generation
YBCO	Yttrium barium copper oxide ($YBa_2Cu_3O_{7-x}$)

List of Publications

This dissertation is the result of the author's work as a graduate student at the Max Planck Institute for the Structure and Dynamics of Matter, within the Quantum Condensed Matter Dynamics division and at the University of Hamburg. The scientific findings presented in this manuscript result in the following scientific publications:

1. M. Budden, T. Gebert, M. Buzzi, G. Jotzu, E. Wang, T. Matsuyama, G. Meier, Y. Laplace, D. Pontiroli, M. Riccò, F. Schlawin, D. Jaksch and A. Cavalleri, *"Evidence for Metastable Photo-Induced Superconductivity in K_3C_{60}"* arXiv:2002.12835, accepted in Nature Physics (2020)

2. M. Budden, T. Gebert and A. Cavalleri, *"Hybrid CO_2-Ti:sapphire laser with tunable pulse duration for mid-infrared-pump terahertz-probe spectroscopy"*, Optics Express 29, 3575-3583 (2021)

Parts of Chapters 4, 5, 6 as well as of Appendizes A, B.1, D, E and E.3 are based on these publications.

ACKNOWLEDGEMENT

I would like to express my sincere gratitude to the multitude of colleagues and friends who have supported me and the project during the course of this dissertation journey.

First and foremost, I would like to thank Prof. Andrea Cavalleri for the opportunity to work in what was in many ways a unique, highly motivating and stimulating research environment. You structured the institute in a way that for me resembled a large research playground with almost unlimited possibilities to discuss ideas and to solve relevant problems. I appreciate your open nature, your availability and honest interest in and feedback on the current state of the experiments as well as your open-mindedness for new and sometimes risky research ideas. Through your support I was able to participate actively in numerous international seminars and conferences already at an early stage. Your special emphasis on the presentation of results and thorough scientific writing was very instructive. Furthermore, I would like to express my special thanks for the fact that you not only tolerated independent projects alongside the work at the Institute, but even generously supported them.

Next I would like to thank Prof. Henning Moritz and Prof. Ludwig Mathey for being my additional supervisors. I very much enjoyed the several (lunch-) meetings where you provided me with helpful advice on both a physics and organizational perspective and I am grateful for the external view you provided on the project itself.

Moreover, I appreciate the cooperative work together with the whole team of the Quantum Condensed Matter Dynamics group at the Max-Planck-Institute for the Structure and Dynamics of Matter.
I would like to address special thanks to Thomas Gebert, who probably was the person I spent most of the time with in the lab during the course of this PhD. We built the whole CO_2 laser beamline and also conducted the experiments on K_3C_{60} together and I am happy I not only found a brilliant colleague, physicist and engineer but also a good friend. I really enjoyed the moonwalking discussions during coffee breaks and am looking forward to further exciting side projects. Thank you, Thomas.
Many thanks go to Guido Mayer, for his continuous support, advice and guidance on various topics even beyond the present work. Besides

the discussions about physics during work and anything at lunch, I appreciated your perseverance to practice talks and to read every text (sometimes several times) including this thesis, and your clear and to the point helpful comments.
I want to express my gratitute also to Michele Buzzi, for countless hours of joint data evaluation, figure (re-)plotting and manuscript (re-)writing. It was a pleasure to learn nonlinear optics and complex physics from you and to make plans for the best experimental approaches.
Sincere thanks are directed to Toru Matsuyama especially for his relentless efforts to solve electronic problems. Your friendly commitment and helpfulness beyond this dissertation project is incredible.
Yannis Laplace was an experienced postdoc when I joined the group, and I am grateful for him being my first optics teacher (which I had no idea about when I started as a real greenhorn to lasers). I am happy to have joined the project you started.
I also want to thank Gregor Jotzu for sharing his deep knowledge and passion about physics and his support regarding the K_3C_{60} experiment. I am happy that you took over and improved the beamline in search of Meissner effects and I am looking forward to further collaborative work on this.
A big thank you goes to the unstoppable Eryin Wang who trained me in pressing powder pellets and building delicate electronic transport samples. Your kind, funny and determined character was a pleasure.
This also holds for Benedikt Schulte. Thank you for your support in cleanroom-activities and for the relaxing shared moments on the water.
It is important to me to thank Tobia Nova, my all time office mate and pleasant companion. Thank you for many open discussions about the ups and downs in life, about future, technology and happiness.
Warm thanks go to Andrea Cartella, the master of nonlinear conversion and my teacher of OPA- and DFG alignment. I really appreciate your sense of humor and word-art and your readiness to help with everything at any time.
Alice Cantaluppi taught me the sweaty process of pellet sample preparation in a glove box. It was always a pleasure to have you around.
Chīle ma, Biaolong Liu? Thank you for teaching me Chinese, introducing me to your delicious world of food and for being my enjoyable lab neighbor.
Ankit Disa was one of the few people of the group who were actively supporting the DAQ software by programming. Thank you for always being ready to help and for your thoughts on sustainability and animal rights.
Furthermore, I am grateful to Michael Först for always having an open ear for problems and his help with both organizational and physics related

questions.
I want to thank Daniele Nicoletti for support in multiple areas, for great shared conference time and for advice in scientific writing.
I also want to mention Eliza Casandruc, Srivats Rajasekaran, Sven Aeshlimann, Marianna Chavez Cervantes, Ratzvan Krause and Alex von Högen who significantly contributed to the quality of life at MPSD.
I want to pay tribute to Matteo Mitrano, on whose groundbreaking experimental results this research builds. I am glad for your advice right after joining the group and for the supportive interaction thereafter.
This project would not have been possible without the extensive help on countless technical details. Michael Volkmann beautifully designed a huge Faraday cage, table extensions, laser housings, cryostat holders, instrument racks and much more.
Elena König persistently helped with lithographic sample preparation and the production of thin films.
Boris Fiedler was always on hand when the CO_2 laser electrics broke another time and for dozens of smaller and bigger electronics projects.
This also holds for Birger Höhling who fearlessly routed and assembled even the most complicated circuit boards.
Jörg Harms had always a helping hand for preparing nice graphics.
Fridjof Tellkamp, Hendrik Schikora and Jan-Philipp Leimkohl were providing one of the most helpful workshops in the institute (not only because of 3D printing) and were always on hand with technical advice and (polishing-) action.
However, without the precision of the workshop team around Stephan Fleig, Michael Hampe and Markus Link this work would not have been possible either. Thank you for all the "express orders".
Also from an administrative perspective, there were several people with helping hands. Dagmar Schröder-Huse enabled several unusual requests and always found a way to settle things unbureaucratically. I am happy about your commitment to the student workshop.
Regina Brodowski, Katja Schröder, Tanja Hartin and Ulrike Warda were the team that made travel organization, employment matters and myriads of orders easy.
Björn Witt, Alina Maetzold and Dennis Braun provided excellent service around IT matters.
I do not underestimate the support of Sakir Sagir, who was doing the multiple small things that smoothen the day and who was of great help with shipping boxes. Thank you all for your help and the wonderful time when working together.

There were also multiple people external to the institute who contributed to the success of this work. The theoretical approach to understanding the long relaxation times was based on a fruitful cooperation with Prof. Dieter Jaksch and Frank Schlawin of Oxford University.
Raw K_3C_{60} sample powder was prepared by Prof. Daniele Pontiroli and Prof. Mauro Riccò of the University of Parma.
A special thanks goes to Nicholas Wolter, a longstanding friend, who was of great help with many problems related to software development and scripting. Thank you for sharing countless hours on the quest for impossible bugs.

It is especially important to me to thank the people who make my personal life meaningful. This relates to my family consisting of Monika, Hans-Günter and my siblings Christina and Florian as well as of my partner Janina. All of you supported me at all times wholeheartedly and most warmly. Thank you for your interest in my projects, your motivation, advice, understanding, perseverance and love.

BIBLIOGRAPHY

[1] *Synergetics Far from Equilibrium*. Vol. 3. Springer Series in Synergetics. Berlin, Heidelberg: Springer Berlin Heidelberg, 1979.

[2] A. Cavalleri. *"Photo-Induced Superconductivity"*. In: Contemporary Physics 59.1 (2018), pp. 31–46.

[3] S. K. Sundaram and E. Mazur. *"Inducing and Probing Non-Thermal Transitions in Semiconductors Using Femtosecond Laser Pulses"*. In: Nature Materials 1.4 (4 2002), pp. 217–224.

[4] F. Bloch. *"Über die Quantenmechanik der Elektronen in Kristallgittern"*. In: Zeitschrift für Physik 52.7 (1929), pp. 555–600.

[5] R. D. L. Kronig, W. G. Penney, and R. H. Fowler. *"Quantum Mechanics of Electrons in Crystal Lattices"*. In: Proceedings of the Royal Society of London. Series A, Containing Papers of a Mathematical and Physical Character 130.814 (1931), pp. 499–513.

[6] A. Sommerfeld. *"Zur Elektronentheorie der Metalle auf Grund der Fermischen Statistik"*. In: Zeitschrift für Physik 47.1 (1928), pp. 1–32.

[7] N. F. Mott. *"The Basis of the Electron Theory of Metals, with Special Reference to the Transition Metals"*. In: Proceedings of the Physical Society. Section A 62.7 (1949), pp. 416–422.

[8] N. F. Mott. *"Metal-Insulator Transition"*. In: Reviews of Modern Physics 40.4 (1968), pp. 677–683.

[9] C. N. R. Rao. *"Transition Metal Oxides"*. In: Annual Review of Physical Chemistry 40.1 (1989), pp. 291–326.

[10] M. Imada, A. Fujimori, and Y. Tokura. *"Metal-Insulator Transitions"*. In: Reviews of Modern Physics 70.4 (1998), pp. 1039–1263.

[11] N. F. Mott. *Metal-Insulator Transitions*. 2nd ed. London ; New York: Taylor & Francis, 1990.

[12] J. Torrance, P. Lacorre, A. Nazzal, E. Ansaldo, and C. Niedermayer. "*Systematic study of insulator-metal transitions in perovskites $RNiO_3$ (R=Pr,Nd,Sm,Eu) due to closing of charge-transfer gap*". In: Physical Review B 45.14 (1992), pp. 8209–8212.

[13] J. H. Van Santen and G. H. Jonker. "*Electrical Conductivity of Ferromagnetic Compounds of Manganese with Perovskite Structure*". In: Physica 16.7 (1950), pp. 599–600.

[14] *Low-Dimensional Electronic Properties of Molybdenum Bronzes and Oxides*. Red. by F. Lévy and E. Mooser. Vol. 11. Physics and Chemistry of Materials with Low-Dimensional Structures. Dordrecht: Springer Netherlands, 1989.

[15] A. McMahan, C. Huscroft, R. Scalettar, and E. Pollock. "*Volume-Collapse Transitions in the Rare Earth Metals*". In: Journal of Computer-Aided Materials Design 5.2 (1998), pp. 131–162.

[16] J. G. Bednorz and K. A. Müller. "*Possible highTc Superconductivity in the Ba−La−Cu−O System*". In: Zeitschrift für Physik B Condensed Matter 64.2 (1986), pp. 189–193.

[17] D. N. Basov, R. D. Averitt, D. van der Marel, M. Dressel, and K. Haule. "*Electrodynamics of Correlated Electron Materials*". In: Reviews of Modern Physics 83.2 (2011), pp. 471–541.

[18] E. Dagotto. "*Complexity in Strongly Correlated Electronic Systems*". In: Science 309.5732 (2005), pp. 257–262.

[19] A. Cavalleri, C. Tóth, C. W. Siders, J. A. Squier, F. Ráksi, P. Forget, and J. C. Kieffer. "*Femtosecond Structural Dynamics in VO_2 during an Ultrafast Solid-Solid Phase Transition*". In: Physical Review Letters 87.23 (2001), p. 237401.

[20] M. Fiebig, K. Miyano, Y. Tomioka, and Y. Tokura. "*Visualization of the Local Insulator-Metal Transition in $Pr_{0.7}Ca_{0.3}MnO_3$*". In: Science 280.5371 (1998), pp. 1925–1928.

[21] H. Uemura, H. Matsuzaki, Y. Takahashi, T. Hasegawa, and H. Okamoto. "*Ultrafast Charge Dynamics in Organic One-Dimensional Mott Insulators*". In: Physica B: Condensed Matter. Proceeding of the 8th International Symposium on Crystalline Organic Metals, Superconductors and Ferromagnets; Yamada Conference LXIV 405 (11, Supplement 2010), S357–S359.

[22] S. Wall, D. Brida, S. R. Clark, H. P. Ehrke, D. Jaksch, A. Ardavan, S. Bonora, H. Uemura, Y. Takahashi, T. Hasegawa, H. Okamoto, G. Cerullo, and A. Cavalleri. *"Quantum Interference between Charge Excitation Paths in a Solid-State Mott Insulator"*. In: Nature Physics 7.2 (2 2011), pp. 114–118.

[23] D. Polli, M. Rini, S. Wall, R. W. Schoenlein, Y. Tomioka, Y. Tokura, G. Cerullo, and A. Cavalleri. *"Coherent Orbital Waves in the Photo-Induced Insulator–Metal Dynamics of a Magnetoresistive Manganite"*. In: Nature Materials 6.9 (9 2007), pp. 643–647.

[24] H. Ehrke, R. I. Tobey, S. Wall, S. A. Cavill, M. Först, V. Khanna, T. Garl, N. Stojanovic, D. Prabhakaran, A. T. Boothroyd, M. Gensch, A. Mirone, P. Reutler, A. Revcolevschi, S. S. Dhesi, and A. Cavalleri. *"Photoinduced Melting of Antiferromagnetic Order in* $La_{0.5}Sr_{1.5}MnO_4$ *Measured Using Ultrafast Resonant Soft X-Ray Diffraction"*. In: Physical Review Letters 106.21 (2011), p. 217401.

[25] M. C. Hoffmann and J. A. Fülöp. *"Intense Ultrashort Terahertz Pulses: Generation and Applications"*. In: Journal of Physics D: Applied Physics 44.8 (2011), p. 083001.

[26] M. Rini, R. Tobey, N. Dean, J. Itatani, Y. Tomioka, Y. Tokura, R. W. Schoenlein, and A. Cavalleri. *"Control of the Electronic Phase of a Manganite by Mode-Selective Vibrational Excitation"*. In: Nature 449.7158 (7158 2007), pp. 72–74.

[27] D. Nicoletti and A. Cavalleri. *"Nonlinear Light–Matter Interaction at Terahertz Frequencies"*. In: Advances in Optics and Photonics 8.3 (2016), pp. 401–464.

[28] M. Först, R. I. Tobey, S. Wall, H. Bromberger, V. Khanna, A. L. Cavalieri, Y.-D. Chuang, W. S. Lee, R. Moore, W. F. Schlotter, J. J. Turner, O. Krupin, M. Trigo, H. Zheng, J. F. Mitchell, S. S. Dhesi, J. P. Hill, and A. Cavalleri. *"Driving Magnetic Order in a Manganite by Ultrafast Lattice Excitation"*. In: Physical Review B 84.24 (2011), p. 241104.

[29] M. Först, C. Manzoni, S. Kaiser, Y. Tomioka, Y. Tokura, R. Merlin, and A. Cavalleri. *"Nonlinear Phononics as an Ultrafast Route to Lattice Control"*. In: Nature Physics 7.11 (11 2011), pp. 854–856.

[30] M. Först, R. Mankowsky, H. Bromberger, D. M. Fritz, H. Lemke, D. Zhu, M. Chollet, Y. Tomioka, Y. Tokura, R. Merlin, J. P. Hill, S. L. Johnson, and A. Cavalleri. *"Displacive Lattice Excitation through Nonlin-*

ear Phononics Viewed by Femtosecond X-Ray Diffraction". In: Solid State Communications 169 (2013), pp. 24–27.

[31] R. Mankowsky, M. Först, and A. Cavalleri. *"Non-Equilibrium Control of Complex Solids by Nonlinear Phononics"*. In: Reports on Progress in Physics 79.6 (2016), p. 064503.

[32] A. Subedi, A. Cavalleri, and A. Georges. *"Theory of Nonlinear Phononics for Coherent Light Control of Solids"*. In: Physical Review B 89.22 (2014), p. 220301.

[33] A. von Hoegen, R. Mankowsky, M. Fechner, M. Först, and A. Cavalleri. *"Probing the Interatomic Potential of Solids with Strong-Field Nonlinear Phononics"*. In: Nature 555.7694 (7694 2018), pp. 79–82.

[34] A. S. Disa, M. Fechner, T. F. Nova, B. Liu, M. Först, D. Prabhakaran, P. G. Radaelli, and A. Cavalleri. *"Polarizing an Antiferromagnet by Optical Engineering of the Crystal Field"*. In: Nature Physics (2020), pp. 1–5.

[35] T. F. Nova, A. Cartella, A. Cantaluppi, M. Först, D. Bossini, R. V. Mikhaylovskiy, A. V. Kimel, R. Merlin, and A. Cavalleri. *"An Effective Magnetic Field from Optically Driven Phonons"*. In: Nature Physics 13.2 (2 2017), pp. 132–136.

[36] D. F. Agterberg, J. S. Davis, S. D. Edkins, E. Fradkin, D. J. Van Harlingen, S. A. Kivelson, P. A. Lee, L. Radzihovsky, J. M. Tranquada, and Y. Wang. *"The Physics of Pair-Density Waves: Cuprate Superconductors and Beyond"*. In: Annual Review of Condensed Matter Physics 11.1 (2020), pp. 231–270.

[37] Y. Wang, D. F. Agterberg, and A. Chubukov. *"Coexistence of Charge-Density-Wave and Pair-Density-Wave Orders in Underdoped Cuprates"*. In: Physical Review Letters 114.19 (2015), p. 197001.

[38] S. Rajasekaran, J. Okamoto, L. Mathey, M. Fechner, V. Thampy, G. D. Gu, and A. Cavalleri. *"Probing Optically Silent Superfluid Stripes in Cuprates"*. In: Science 359.6375 (2018), pp. 575–579.

[39] Y. J. Uemura, G. M. Luke, B. J. Sternlieb, J. H. Brewer, J. F. Carolan, W. N. Hardy, R. Kadono, J. R. Kempton, R. F. Kiefl, S. R. Kreitzman, P. Mulhern, T. M. Riseman, D. L. Williams, B. X. Yang, S. Uchida, H. Takagi, J. Gopalakrishnan, A. W. Sleight, M. A. Subramanian, C. L. Chien, M. Z. Cieplak, G. Xiao, V. Y. Lee, B. W. Statt, C. E. Stronach, W. J. Kossler, and X. H. Yu. *"Universal Correlations between T_c and $\frac{n_s}{m^*}$*

(Carrier Density over Effective Mass) in High-T_c Cuprate Superconductors". In: Physical Review Letters 62.19 (1989), pp. 2317–2320.

[40] D. Fausti, R. I. Tobey, N. Dean, S. Kaiser, A. Dienst, M. C. Hoffmann, S. Pyon, T. Takayama, H. Takagi, and A. Cavalleri. *"Light-Induced Superconductivity in a Stripe-Ordered Cuprate"*. In: Science 331.6014 (2011), pp. 189–191.

[41] M. Först, R. I. Tobey, H. Bromberger, S. B. Wilkins, V. Khanna, A. D. Caviglia, Y.-D. Chuang, W. S. Lee, W. F. Schlotter, J. J. Turner, M. P. Minitti, O. Krupin, Z. J. Xu, J. S. Wen, G. D. Gu, S. S. Dhesi, A. Cavalleri, and J. P. Hill. *"Melting of Charge Stripes in Vibrationally Driven* $La_{1.875}Ba_{0.125}CuO_4$*: Assessing the Respective Roles of Electronic and Lattice Order in Frustrated Superconductors"*. In: Physical Review Letters 112.15 (2014), p. 157002.

[42] W. Hu, S. Kaiser, D. Nicoletti, C. R. Hunt, I. Gierz, M. C. Hoffmann, M. Le Tacon, T. Loew, B. Keimer, and A. Cavalleri. *"Optically enhanced coherent transport in $YBa_2Cu_3O_{6.5}$ by ultrafast redistribution of interlayer coupling"*. In: Nature Materials 13.7 (7 2014), pp. 705–711.

[43] S. Kaiser, C. R. Hunt, D. Nicoletti, W. Hu, I. Gierz, H. Y. Liu, M. Le Tacon, T. Loew, D. Haug, B. Keimer, and A. Cavalleri. *"Optically induced coherent transport far above T_c in underdoped* $YBa_2Cu_3O_{6+\delta}$*"*. In: Physical Review B 89.18 (2014), p. 184516.

[44] E. Pavarini, I. Dasgupta, T. Saha-Dasgupta, O. Jepsen, and O. K. Andersen. *"Band-Structure Trend in Hole-Doped Cuprates and Correlation with $T_{c\max}$"*. In: Physical Review Letters 87.4 (2001), p. 047003.

[45] R. Mankowsky, A. Subedi, M. Först, S. O. Mariager, M. Chollet, H. T. Lemke, J. S. Robinson, J. M. Glownia, M. P. Minitti, A. Frano, M. Fechner, N. A. Spaldin, T. Loew, B. Keimer, A. Georges, and A. Cavalleri. *"Nonlinear lattice dynamics as a basis for enhanced superconductivity in $YBa_2Cu_3O_{6.5}$"*. In: Nature 516.7529 (7529 2014), pp. 71–73.

[46] M. Magnuson, T. Schmitt, V. N. Strocov, J. Schlappa, A. S. Kalabukhov, and L.-C. Duda. *"Self-doping processes between planes and chains in the metal-to-superconductor transition of $YBa_2Cu_3O_{6.9}$"*. In: Scientific Reports 4.1 (1 2014), p. 7017.

[47] R. Mankowsky, M. Först, T. Loew, J. Porras, B. Keimer, and A. Cavalleri. *"Coherent modulation of the* $YBa_2Cu_3O_{6+x}$ *atomic structure by dis-*

placive stimulated ionic Raman scattering". In: Physical Review B 91.9 (2015), p. 094308.

[48] S. J. Denny, S. R. Clark, Y. Laplace, A. Cavalleri, and D. Jaksch. *"Proposed Parametric Cooling of Bilayer Cuprate Superconductors by Terahertz Excitation"*. In: Physical Review Letters 114.13 (2015), p. 137001.

[49] R. Höppner, B. Zhu, T. Rexin, A. Cavalleri, and L. Mathey. *"Redistribution of Phase Fluctuations in a Periodically Driven Cuprate Superconductor"*. In: Physical Review B 91.10 (2015), p. 104507.

[50] E. Uykur, K. Tanaka, T. Masui, S. Miyasaka, and S. Tajima. *"Persistence of the Superconducting Condensate Far above the Critical Temperature of* $YBa_2(Cu,Zn)_3O_y$ *Revealed by c-Axis Optical Conductivity Measurements for Several Zn Concentrations and Carrier Doping Levels"*. In: Physical Review Letters 112.12 (2014), p. 127003.

[51] R. Singla, G. Cotugno, S. Kaiser, M. Först, M. Mitrano, H. Y. Liu, A. Cartella, C. Manzoni, H. Okamoto, T. Hasegawa, S. R. Clark, D. Jaksch, and A. Cavalleri. *"THz-Frequency Modulation of the Hubbard U in an Organic Mott Insulator"*. In: Physical Review Letters 115.18 (2015), p. 187401.

[52] M. Buzzi, D. Nicoletti, M. Fechner, N. Tancogne-Dejean, M. A. Sentef, A. Georges, T. Biesner, E. Uykur, M. Dressel, A. Henderson, T. Siegrist, J. A. Schlueter, K. Miyagawa, K. Kanoda, M.-S. Nam, A. Ardavan, J. Coulthard, J. Tindall, F. Schlawin, D. Jaksch, and A. Cavalleri. *"Photomolecular High-Temperature Superconductivity"*. In: Physical Review X 10.3 (2020), p. 031028.

[53] H. W. Kroto, J. R. Heath, S. C. O'Brien, R. F. Curl, and R. E. Smalley. *"*C_{60}*: Buckminsterfullerene"*. In: Nature 318.6042 (6042 1985), pp. 162–163.

[54] W. Krätschmer, L. D. Lamb, K. Fostiropoulos, and D. R. Huffman. *"Solid* C_{60} *: a new form of carbon"*. In: Nature 347.6291 (6291 1990), pp. 354–358.

[55] R. C. Haddon, A. F. Hebard, M. J. Rosseinsky, D. W. Murphy, S. J. Duclos, K. B. Lyons, B. Miller, J. M. Rosamilia, R. M. Fleming, A. R. Kortan, S. H. Glarum, A. V. Makhija, A. J. Muller, R. H. Eick, S. M. Zahurak, R. Tycko, G. Dabbagh, and F. A. Thiel. *"Conducting films of* C_{60} *and* C_{70} *by alkali-metal doping"*. In: Nature 350.6316 (6316 1991), pp. 320–322.

[56] A. F. Hebard, M. J. Rosseinsky, R. C. Haddon, D. W. Murphy, S. H. Glarum, T. T. M. Palstra, A. P. Ramirez, and A. R. Kortan. *"Superconductivity at* 18 K *in potassium-doped* C_{60}*"*. In: Nature 350.6319 (6319 1991), pp. 600–601.

[57] K. Holczer, O. Klein, S.-m. Huang, R. B. Kaner, K.-j. Fu, R. L. Whetten, and F. Diederich. *"Alkali-Fulleride Superconductors: Synthesis, Composition, and Diamagnetic Shielding"*. In: Science 252.5009 (1991), pp. 1154–1157.

[58] M. J. Rosseinsky, A. P. Ramirez, S. H. Glarum, D. W. Murphy, R. C. Haddon, A. F. Hebard, T. T. M. Palstra, A. R. Kortan, S. M. Zahurak, and A. V. Makhija. *"Superconductivity at* 28 K *in* Rb_xC_{60}*"*. In: Physical Review Letters 66.21 (1991), pp. 2830–2832.

[59] K. Tanigaki, T. W. Ebbesen, S. Saito, J. Mizuki, J. S. Tsai, Y. Kubo, and S. Kuroshima. *"Superconductivity at* 33 K *in* $Cs_xRb_yC_{60}$*"*. In: Nature 352.6332 (6332 1991), pp. 222–223.

[60] W. I. F. David, R. M. Ibberson, J. C. Matthewman, K. Prassides, T. J. S. Dennis, J. P. Hare, H. W. Kroto, R. Taylor, and D. R. M. Walton. *"Crystal structure and bonding of ordered* C_{60}*"*. In: Nature 353.6340 (6340 1991), pp. 147–149.

[61] D. L. Novikov, V. A. Gubanov, and A. J. Freeman. *"Electronic structure, electron-phonon interaction and superconductivity in* K_3C_{60}*,* Rb_3C_{60} *and* Cs_3C_{60}*"*. In: Physica C: Superconductivity 191.3 (1992), pp. 399–408.

[62] O. Zhou, Q. Zhu, J. E. Fischer, N. Coustel, G. B. M. Vaughan, P. A. Heiney, J. P. Mccauley, and A. B. Smith. *"Compressibility of* M_3C_{60} *Fullerene Superconductors: Relation Between Tc and Lattice Parameter"*. In: Science 255.5046 (1992), pp. 833–835.

[63] R. H. Zadik, Y. Takabayashi, G. Klupp, R. H. Colman, A. Y. Ganin, A. Potočnik, P. Jeglič, D. Arčon, P. Matus, K. Kamarás, Y. Kasahara, Y. Iwasa, A. N. Fitch, Y. Ohishi, G. Garbarino, K. Kato, M. J. Rosseinsky, and K. Prassides. *"Optimized Unconventional Superconductivity in a Molecular Jahn-Teller Metal"*. In: Science Advances 1.3 (2015), e1500059.

[64] D. Koller, M. C. Martin, L. Mihály, G. Mihály, G. Oszlányi, G. Baumgartner, and L. Forró. *"Energy Gap in Superconducting Fullerides: Optical and Tunneling Studies"*. In: Physical Review Letters 77.19 (1996), pp. 4082–4085.

[65] S. Sasaki, A. Matsuda, and C. W. Chu. *"Fermi-Liquid Behavior and BCS s-Wave Pairing of K_3C_{60} Observed by ^{13}C-NMR"*. In: Journal of the Physical Society of Japan 63.5 (1994), pp. 1670–1673.

[66] Z. Zhang, C.-C. Chen, and C. M. Lieber. *"Tunneling Spectroscopy of M_3C_{60} Superconductors: The Energy Gap, Strong Coupling, and Superconductivity"*. In: Science 254.5038 (1991), pp. 1619–1621.

[67] Y. Kasahara, Y. Takeuchi, T. Itou, R. H. Zadik, Y. Takabayashi, A. Y. Ganin, D. Arčon, M. J. Rosseinsky, K. Prassides, and Y. Iwasa. *"Spin frustration and magnetic ordering in the $S = \frac{1}{2}$ molecular antiferromagnet* fcc $-$ Cs_3C_{60}*"*. In: Physical Review B 90.1 (2014), p. 014413.

[68] K.-P. Bohnen, R. Heid, K.-M. Ho, and C. T. Chan. *"Ab initio investigation of the vibrational and geometrical properties of solid* C_{60} *and* K_3 C_{60}*"*. In: Physical Review B 51.9 (1995), pp. 5805–5813.

[69] A. F. Hebard. *"Superconductivity in Doped Fullerenes"*. In: Physics Today 45.11 (1992), pp. 26–32.

[70] O. Gunnarsson. *"Superconductivity in Fullerides"*. In: Reviews of Modern Physics 69.2 (1997), pp. 575–606.

[71] T. W. Ebbesen, J. S. Tsai, K. Tanigaki, H. Hiura, Y. Shimakawa, Y. Kubo, I. Hirosawa, and J. Mizuki. *"Dopant isotope effect on superconductivity in Rb_3C_{60}"*. In: Physica C: Superconductivity 203.1 (1992), pp. 163–166.

[72] A. P. Ramirez, A. R. Kortan, M. J. Rosseinsky, S. J. Duclos, A. M. Mujsce, R. C. Haddon, D. W. Murphy, A. V. Makhija, S. M. Zahurak, and K. B. Lyons. *"Isotope effect in superconducting* Rb_3C_{60}*"*. In: Physical Review Letters 68.7 (1992), pp. 1058–1060.

[73] C.-C. Chen and C. M. Lieber. *"Isotope Effect and Superconductivity in Metal-Doped C_{60}"*. In: Science 259.5095 (1993), pp. 655–658.

[74] C. C. Chen and C. M. Lieber. *"Synthesis of pure $^{13}C_{60}$ and determination of the isotope effect for fullerene superconductors"*. In: Journal of the American Chemical Society 114.8 (1992), pp. 3141–3142.

[75] O. Gunnarsson and G. Zwicknagl. *"Coulomb pseudopotential, screening and superconductivity in* C_{60}*"*. In: Physical Review Letters 69.6 (1992), pp. 957–960.

[76] C. Christides, D. A. Neumann, K. Prassides, J. R. D. Copley, J. J. Rush, M. J. Rosseinsky, D. W. Murphy, and R. C. Haddon. *"Neutron-scattering study of C_{60}^{n-} (n=3,6) librations in alkali-metal fullerides"*. In: Physical Review B 46.18 (1992), pp. 12088–12091.

[77] V. P. Antropov, O. Gunnarsson, and A. I. Liechtenstein. *"Phonons, electron-phonon, and electron-plasmon coupling in C_{60} compounds"*. In: Physical Review B 48.10 (1993), pp. 7651–7664.

[78] L. Degiorgi. *"The Complete Excitation Spectrum of the Alkali-Metal-Doped Superconducting Fullerenes"*. In: Modern Physics Letters B 09.08 (1995), pp. 445–468.

[79] O. Gunnarsson. *Alkali-Doped Fullerides: Narrow-Band Solids with Unusual Properties*. River Edge, N.J: World Scientific, 2004.

[80] M. Schlüter, M. Lannoo, M. Needels, G. A. Baraff, and D. Tománek. *"Superconductivity in alkali intercalated C_{60}"*. In: Journal of Physics and Chemistry of Solids 53.11 (1992), pp. 1473–1485.

[81] S. Satpathy, V. P. Antropov, O. K. Andersen, O. Jepsen, O. Gunnarsson, and A. I. Liechtenstein. *"Conduction-band structure of alkali-metal-doped C_{60}"*. In: Physical Review B 46.3 (1992), pp. 1773–1793.

[82] C. T. Chen, L. H. Tjeng, P. Rudolf, G. Meigs, J. E. Rowe, J. Chen, J. P. McCauley, A. B. Smith, A. R. McGhie, W. J. Romanow, and E. W. Plummer. *"Electronic states and phases of K_xC_{60} from photoemission and X-ray absorption spectroscopy"*. In: Nature 352.6336 (6336 1991), pp. 603–605.

[83] W. H. Wong, M. E. Hanson, W. G. Clark, G. Grüner, J. D. Thompson, R. L. Whetten, S.-M. Huang, R. B. Kaner, F. Diederich, P. Petit, J.-J. André, and K. Holczer. *"Normal-State Magnetic Properties of K_3C_{60}"*. In: Europhysics Letters (EPL) 18.1 (1992), pp. 79–84.

[84] S. C. Erwin and W. E. Pickett. *"Theoretical Fermi-Surface Properties and Superconducting Parameters for K_3C_{60}"*. In: Science 254.5033 (1991), pp. 842–845.

[85] R. C. Haddon. *"Electronic structure, conductivity and superconductivity of alkali metal doped C_{60}"*. In: Accounts of Chemical Research 25.3 (1992), pp. 127–133.

[86] R. W. Lof, M. A. van Veenendaal, B. Koopmans, H. T. Jonkman, and G. A. Sawatzky. *"Band gap, excitons, and Coulomb interaction in solid C_{60}"*. In: Physical Review Letters 68.26 (1992), pp. 3924–3927.

[87] J. E. Han and O. Gunnarsson. *"Metal–Insulator Transitions in Systems with Electron–Phonon and Coulomb Interactions"*. In: Physica B: Condensed Matter 292.3 (2000), pp. 196–207.

[88] X.-D. Xiang, J. G. Hou, G. Briceño, W. A. Vareka, R. Mostovoy, A. Zettl, V. H. Crespi, and M. L. Cohen. *"Synthesis and Electronic Transport of Single Crystal K_3C_{60}"*. In: Science 256.5060 (1992), pp. 1190–1191.

[89] Z. H. Wang, A. W. P. Fung, G. Dresselhaus, M. S. Dresselhaus, K. A. Wang, P. Zhou, and P. C. Eklund. *"Electron-electron interactions and superconducting fluctuations in weakly localized K_3C_{60}"*. In: Physical Review B 47.22 (1993), pp. 15354–15357.

[90] C. Politis, V. Buntar, W. Krauss, and A. Gurevich. *"Magnetic Properties of Superconducting Rb_3C_{60}"*. In: Europhysics Letters (EPL) 17.2 (1992), pp. 175–179.

[91] Y. Maruyama, T. Inabe, H. Ogata, Y. Achiba, S. Suzuki, K. Kikuchi, and I. Ikemoto. *"Observation of Metallic Conductivity and Sharp Superconducting Transition at* 19 K *in Potassium-Doped Fulleride, C_{60}, Single Crystal"*. In: Chemistry Letters 20.10 (1991), pp. 1849–1852.

[92] X.-D. Xiang, J. G. Hou, V. H. Crespi, A. Zettl, and M. L. Cohen. *"Three-dimensional fluctuation conductivity in superconducting single crystal K_3C_{60} and Rb_3C_{60}"*. In: Nature 361.6407 (6407 1993), pp. 54–56.

[93] T. T. M. Palstra, R. C. Haddon, A. F. Hebard, and J. Zaanen. *"Electronic transport properties of K_3C_{60} films"*. In: Physical Review Letters 68.7 (1992), pp. 1054–1057.

[94] T. T. M. Palstra, A. F. Hebard, R. C. Haddon, and P. B. Littlewood. *"Fermi-liquid behavior in the electrical resistivity of K_3C_{60} and Rb_3C_{60}"*. In: Physical Review B 50.5 (1994), pp. 3462–3465.

[95] S. Rogge, A. Dunn, T. Melin, C. Dekker, and L. Geerligs. *"Electrical transport through ultrathin ordered K_3C_{60} films on Si"*. In: Carbon 38.11-12 (2000), pp. 1647–1651.

[96] A. F. Hebard, T. T. M. Palstra, R. C. Haddon, and R. M. Fleming. *"Absence of saturation in the normal-state resistivity of thin films of K_3C_{60} and Rb_3C_{60}"*. In: Physical Review B 48.13 (1993), pp. 9945–9948.

[97] M. Gurvitch. *"Ioffe-Regel Criterion and Resistivity of Metals"*. In: Physical Review B 24.12 (1981), pp. 7404–7407.

[98] V. Buntar and H. W. Weber. *"Magnetic Properties of Fullerene Superconductors"*. In: Superconductor Science and Technology 9.8 (1996), pp. 599–615.

[99] V. Buntar, F. M. Sauerzopf, and H. W. Weber. *"Solid State and Magnetic Properties of Pure, Intercalated and Superconducting Fullerenes"*. In: Australian Journal of Physics 50.2 (1997), pp. 329–361.

[100] A. Y. Ganin, Y. Takabayashi, P. Jeglič, D. Arčon, A. Potočnik, P. J. Baker, Y. Ohishi, M. T. McDonald, M. D. Tzirakis, A. McLennan, G. R. Darling, M. Takata, M. J. Rosseinsky, and K. Prassides. *"Polymorphism control of superconductivity and magnetism in Cs_3C_{60} close to the Mott transition"*. In: Nature 466.7303 (7303 2010), pp. 221–225.

[101] R. M. Fleming, A. P. Ramirez, M. J. Rosseinsky, D. W. Murphy, R. C. Haddon, S. M. Zahurak, and A. V. Makhija. *"Relation of structure and superconducting transition temperatures in A_3C_{60}"*. In: Nature 352.6338 (6338 1991), pp. 787–788.

[102] L. Degiorgi, G. Briceno, M. S. Fuhrer, A. Zettl, and P. Wachter. *"Optical measurements of the superconducting gap in single-crystal K_3C_{60} and Rb_3C_{60}"*. In: Nature 369.6481 (6481 1994), pp. 541–543.

[103] A. Potočnik, A. Krajnc, P. Jeglič, Y. Takabayashi, A. Y. Ganin, K. Prassides, M. J. Rosseinsky, and D. Arčon. *"Size and symmetry of the superconducting gap in the f.c.c. Cs_3C_{60} polymorph close to the metal-Mott insulator boundary"*. In: Scientific Reports 4.1 (1 2014), pp. 1–5.

[104] L. Degiorgi, P. Wachter, G. Grüner, S.-M. Huang, J. Wiley, and R. B. Kaner. *"Optical response of the superconducting state of K_3C_{60} and Rb_3C_{60}"*. In: Physical Review Letters 69.20 (1992), pp. 2987–2990.

[105] L. Degiorgi. *"Optical Spectroscopy on Alkali-Metal Doped Fullerene Compounds"*. In: Journal of Low Temperature Physics 105.5-6 (1996), pp. 1671–1680.

[106] R. Hesper, L. H. Tjeng, A. Heeres, and G. A. Sawatzky. *"BCS-like Density of States in Superconducting A_3C_{60} Surfaces"*. In: Physical Review Letters 85.9 (2000), pp. 1970–1973.

[107] L. D. Rotter, Z. Schlesinger, J. P. McCauley, N. Coustel, J. E. Fischer, and A. B. Smith. *"Infrared reflectivity measurements of a superconducting energy scale in Rb_3C_{60}"*. In: Nature 355.6360 (6360 1992), pp. 532–534.

[108] R. Tycko, G. Dabbagh, M. J. Rosseinsky, D. W. Murphy, A. P. Ramirez, and R. M. Fleming. *"Electronic properties of normal and superconducting alkali fullerides probed by ^{13}C nuclear magnetic resonance"*. In: Physical Review Letters 68.12 (1992), pp. 1912–1915.

[109] Z. Zhang, C.-C. Chen, S. P. Kelty, H. Dai, and C. M. Lieber. *"The superconducting energy gap of Rb_3C_{60}"*. In: Nature 353.6342 (6342 1991), pp. 333–335.

[110] V. A. Stenger, C. H. Pennington, D. R. Buffinger, and R. P. Ziebarth. *"Nuclear Magnetic Resonance of A_3C_{60} Superconductors"*. In: Physical Review Letters 74.9 (1995), pp. 1649–1652.

[111] R. A. Jishi and M. S. Dresselhaus. *"Electron-Phonon Coupling Strength and Implications for Superconductivity in Alkali-Metal-Doped Fullerenes"*. In: Physical Review B 45.5 (1992), pp. 2597–2600.

[112] M. Schluter, M. Lannoo, M. Needels, G. A. Baraff, and D. Tománek. *"Electron-phonon coupling and superconductivity in alkali-intercalated C_{60} solid"*. In: Physical Review Letters 68.4 (1992), pp. 526–529.

[113] S. Chakravarty, S. A. Kivelson, M. I. Salkola, and S. Tewari. *"Isotope Effect in Superconducting Fullerenes"*. In: Science 256.5061 (1992), pp. 1306–1308.

[114] Y. Nomura, S. Sakai, M. Capone, and R. Arita. *"Exotic S-Wave Superconductivity in Alkali-Doped Fullerides"*. In: Journal of Physics: Condensed Matter 28.15 (2016), p. 153001.

[115] V. Ginzburg, D. Abramovich Kirzhnits, and J. L. Birdman. *High-Temperature Superconductivity*. Consultant Bureau. A Division of Plenum Publishing Co, 1982.

[116] M. Capone, M. Fabrizio, C. Castellani, and E. Tosatti. *"Strongly Correlated Superconductivity"*. In: Science 296.5577 (2002), pp. 2364–2366.

[117] M. Fabrizio and E. Tosatti. *"Nonmagnetic Molecular Jahn-Teller Mott Insulators"*. In: Physical Review B 55.20 (1997), pp. 13465–13472.

[118] J. E. Han, O. Gunnarsson, and V. H. Crespi. *"Strong Superconductivity with Local Jahn-Teller Phonons in C_{60} Solids"*. In: Physical Review Letters 90.16 (2003), p. 167006.

[119] G. Klupp, P. Matus, K. Kamarás, A. Y. Ganin, A. McLennan, M. J. Rosseinsky, Y. Takabayashi, M. T. McDonald, and K. Prassides. *"Dynamic Jahn-Teller effect in the parent insulating state of the molecular superconductor Cs_3C_{60}"*. In: Nature Communications 3 (2012), p. 912.

[120] G. Klupp, K. Kamarás, N. M. Nemes, C. M. Brown, and J. Leão. *"Static and dynamic Jahn-Teller effect in the alkali metal fulleride salts A_4C_{60} (A = K, Rb, Cs)"*. In: Physical Review B 73.8 (2006), p. 085415.

[121] M. Kim, Y. Nomura, M. Ferrero, P. Seth, O. Parcollet, and A. Georges. *"Enhancing superconductivity in A_3C_{60} fullerides"*. In: Physical Review B 94.15 (2016), p. 155152.

[122] A. Cantaluppi, M. Buzzi, G. Jotzu, D. Nicoletti, M. Mitrano, D. Pontiroli, M. Riccò, A. Perucchi, P. Di Pietro, and A. Cavalleri. *"Pressure tuning of light-induced superconductivity in K_3C_{60}"*. In: Nature Physics 14.8 (2018), pp. 837–841.

[123] M. Mitrano, A. Cantaluppi, D. Nicoletti, S. Kaiser, A. Perucchi, S. Lupi, P. Di Pietro, D. Pontiroli, M. Riccò, S. R. Clark, D. Jaksch, and A. Cavalleri. *"Possible light-induced superconductivity in K_3C_{60} at high temperature"*. In: Nature 530.7591 (2016), pp. 461–464.

[124] M. Dressel and G. Grüner. *Electrodynamics of Solids: Optical Properties of Electrons in Matter*. Cambridge ; New York: Cambridge University Press, 2002.

[125] L. Degiorgi, E. J. Nicol, O. Klein, G. Grüner, P. Wachter, S.-M. Huang, J. Wiley, and R. B. Kaner. *"Optical properties of the alkali-metal-doped superconducting fullerenes: K_3C_{60} and Rb_3C_{60}"*. In: Physical Review B 49.10 (1994), pp. 7012–7025.

[126] J. S. Plaskett and P. N. Schatz. *"On the Robinson and Price (Kramers—Kronig) Method of Interpreting Reflection Data Taken through a Transparent Window"*. In: The Journal of Chemical Physics 38.3 (1963), pp. 612–617.

[127] A. Cantaluppi. *"Tuning light-induced superconductivity in K_3C_{60}"*. Hamburg, 2017.

[128] M. Mitrano. *"Nonequilibrium Emergent Phenomena in Organic Molecular Solids"*. Hamburg, 2015.

[129] S. Kaiser, S. R. Clark, D. Nicoletti, G. Cotugno, R. I. Tobey, N. Dean, S. Lupi, H. Okamoto, T. Hasegawa, D. Jaksch, and A. Cavalleri. *"Optical Properties of a Vibrationally Modulated Solid State Mott Insulator"*. In: Scientific Reports 4.1 (1 2014), pp. 1–6.

[130] M. C. Martin, X. Du, J. Kwon, and L. Mihaly. *"Observation and assignment of silent and higher-order vibrations in the infrared transmission of C_{60} crystals"*. In: Physical Review B 50.1 (1994), pp. 173–183.

[131] J. Menéndez and J. B. Page. *"Vibrational spectroscopy of C_{60}"*. In: Light Scattering in Solids VIII: Fullerenes, Semiconductor Surfaces, Coherent Phonons. Topics in Applied Physics. Berlin, Heidelberg: Springer, 2000, pp. 27–95.

[132] J. Demsar, R. D. Averitt, A. J. Taylor, V. V. Kabanov, W. N. Kang, H. J. Kim, E. M. Choi, and S. I. Lee. *"Pair-Breaking and Superconducting State Recovery Dynamics in MgB_2"*. In: Physical Review Letters 91.26 (2003), p. 267002.

[133] A. Rothwarf and B. N. Taylor. *"Measurement of Recombination Lifetimes in Superconductors"*. In: Physical Review Letters 19.1 (1967), pp. 27–30.

[134] A. Oshiyama and S. Saito. *"Linear dependence of superconducting transition temperature on Fermi-level density-of-states in alkali-doped C_{60}"*. In: Solid State Communications 82.1 (1992), pp. 41–45.

[135] J. Diederichs, A. K. Gangopadhyay, and J. S. Schilling. *"Pressure dependence of the electronic density of states and T_c in superconducting Rb_3C_{60}"*. In: Physical Review B 54.14 (1996), R9662–R9665.

[136] G. Sparn, J. D. Thompson, S.-M. Huang, R. B. Kaner, F. Diederich, R. L. Whetten, G. Grüner, and K. Holczer. *"Pressure Dependence of Superconductivity in Single-Phase K_3C_{60}"*. In: Science 252.5014 (1991), pp. 1829–1831.

[137] M.-Z. Huang, Y.-N. Xu, and W. Y. Ching. *"Electronic structures of K_3C_{60}, RbK_2C_{60}, Rb_3C_{60}, Rb_2CsC_{60}, and Cs_3C_{60} crystals"*. In: Physical Review B 46.10 (1992), pp. 6572–6577.

[138] M.-Z. Huang, Y.-N. Xu, and W. Y. Ching. *"Pressure dependence of the band structure, density of states, Fermi surfaces, and optical properties of*

superconducting K_3C_{60}". In: Physical Review B 47.13 (1993), pp. 8249–8259.

[139] M. J. Weber. *Handbook of Laser Wavelengths*. CRC Press LLC, 1999.

[140] M. Ebrahim-Zadeh, I. T. Sorokina, and S. NATO Advanced Research Workshop on Middle Infrared Coherent Sources (2005 : Barcelona. *Mid-Infrared Coherent Sources and Applications*. Dordrecht: Springer in cooperation with NATO Public Diplomacy Division, 2008.

[141] S. D. Jackson. *"Towards High-Power Mid-Infrared Emission from a Fibre Laser"*. In: Nature Photonics 6.7 (7 2012), pp. 423–431.

[142] A. Schliesser, N. Picqué, and T. W. Hänsch. *"Mid-Infrared Frequency Combs"*. In: Nature Photonics 6.7 (7 2012), pp. 440–449.

[143] I. T. Sorokina and K. L. Vodopayanov. *Solid-State Mid-InfraredLaserSources*. Vol. 89. Topics in Applied Physics. Springer Berlin Heidelberg, 2003.

[144] M. Tacke. *"Lead–Salt Lasers"*. In: Philosophical Transactions of the Royal Society of London. Series A: Mathematical, Physical and Engineering Sciences 359.1780 (2001), pp. 547–566.

[145] J. Faist, F. Capasso, D. L. Sivco, C. Sirtori, A. L. Hutchinson, and A. Y. Cho. *"Quantum Cascade Laser"*. In: Science 264.5158 (1994), pp. 553–556.

[146] R. W. Boyd. *Nonlinear Optics*. Third Edition. Academic Press, 2008.

[147] E. Brown, M. Gundersen, and P. Williams. *"New Infrared Laser Lines in Argon, Krypton, and Xenon"*. In: IEEE Journal of Quantum Electronics 16.6 (1980), pp. 683–684.

[148] D. Haberberger, S. Tochitsky, and C. Joshi. *"Fifteen terawatt picosecond CO_2 laser system"*. In: Optics Express 18.17 (2010), pp. 17865–17875.

[149] A. F. Gibson, M. F. Kimmitt, and A. C. Walker. *"Photon Drag in Germanium"*. In: Applied Physics Letters 17.2 (1970), pp. 75–77.

[150] A. A. Grinberg. *"Theory of the Photoelectric and Photomagnetic Effects Produced by Light Pressure"*. In: JETP 31.3 (1970), p. 531.

[151] A. F. Gibson, M. F. Kimmitt, and B. Norris. *"Generation of bandwidth-limited pulses from a TEA CO_2 laser using p-type germanium"*. In: Applied Physics Letters 24.7 (1974), pp. 306–307.

[152] A. Nurmikko, T. A. DeTemple, and S. E. Schwarz. *"Single-mode operation and mode locking of high-pressure CO_2 lasers by means of saturable absorbers"*. In: Applied Physics Letters 18.4 (1971), pp. 130–132.

[153] O. R. Wood and S. E. Schwarz. *"Passive q-switching of a CO_2 laser"*. In: Applied Physics Letters 11.3 (1967), pp. 88–89.

[154] G. L. Bourdet, R. A. Muller, G. M. Mullot, and J. Y. Vinet. *"Active mode locking of a high pressure CW waveguide CO_2 laser"*. In: Applied Physics B 44.2 (1987), pp. 107–110.

[155] T. J. Bridges and P. K. Cheo. *"Spontaneous self-pulsing and cavity dumping in a CO_2 laser with electro-optic q-switching"*. In: Applied Physics Letters 14.9 (1969), pp. 262–264.

[156] M. Babzien, I. V. Pogorelsky, and M. Polanskiy. *"Solid-State Seeding of a High Power Picosecond Carbon Dioxide Laser"*. In: Advanced Accelerator Concepts 2016: 16th Advanced Accelerator Concepts Workshop. San Jose, CA, USA, 2016, p. 110001.

[157] B. Patel. *"Collision broadening of high pressure CO and CO_2 laser transitions"*. In: Physics Letters A 45.2 (1973), pp. 137–138.

[158] A. J. Alcock and A. C. Walker. *"Generation and detection of 150-psec mode-locked pulses from a multi-atmosphere CO_2 laser"*. In: Applied Physics Letters 25.5 (1974), pp. 299–301.

[159] P. Corkum. *"Amplification of picosecond 10 µm pulses in multiatmosphere CO_2 lasers"*. In: IEEE Journal of Quantum Electronics 21.3 (1985), pp. 216–232.

[160] M. N. Polyanskiy, I. V. Pogorelsky, and V. Yakimenko. *"Picosecond pulse amplification in isotopic CO_2 active medium"*. In: Optics Express 19.8 (2011), pp. 7717–7725.

[161] I. E. Gordon, L. S. Rothman, C. Hill, R. V. Kochanov, Y. Tan, P. F. Bernath, M. Birk, V. Boudon, A. Campargue, K. V. Chance, B. J. Drouin, J. .-M. Flaud, R. R. Gamache, J. T. Hodges, D. Jacquemart, V. I. Perevalov, A. Perrin, K. P. Shine, M. .-A. H. Smith, J. Tennyson, G. C. Toon, H. Tran, V. G. Tyuterev, A. Barbe, A. G. Császár, V. M. Devi, T. Furtenbacher, J. J. Harrison, J. .-M. Hartmann,

A. Jolly, T. J. Johnson, T. Karman, I. Kleiner, A. A. Kyuberis, J. Loos, O. M. Lyulin, S. T. Massie, S. N. Mikhailenko, N. Moazzen-Ahmadi, H. S. P. Müller, O. V. Naumenko, A. V. Nikitin, O. L. Polyansky, M. Rey, M. Rotger, S. W. Sharpe, K. Sung, E. Starikova, S. A. Tashkun, J. V. Auwera, G. Wagner, J. Wilzewski, P. Wcisło, S. Yu, and E. J. Zak. *"The HITRAN2016 Molecular Spectroscopic Database"*. In: Journal of Quantitative Spectroscopy and Radiative Transfer. HITRAN2016 Special Issue 203 (2017), pp. 3–69.

[162] V. N. Bagratashvili, I. N. Knyazev, and V. S. Letokhov. *"On the Tunable Infrared Gas Lasers"*. In: Optics Communications 4.2 (1971), pp. 154–156.

[163] E. Yablonovitch. *"Spectral Broadening in the Light Transmitted through a Rapidly Growing Plasma"*. In: Physical Review Letters 31.14 (1973), pp. 877–879.

[164] E. Yablonovitch and J. Goldhar. *"Short CO_2 laser pulse generation by optical free induction decay"*. In: Applied Physics Letters 25.10 (1974), pp. 580–582.

[165] M. Sheik-bahaei and H. S. Kwok. *"Characterization of a picosecond CO_2 laser system"*. In: Applied Optics 24.5 (1985), p. 666.

[166] A. J. Alcock, P. B. Corkum, and D. J. James. *"A fast scalable switching technique for high-power CO_2 laser radiation"*. In: Applied Physics Letters 27.12 (1975), pp. 680–682.

[167] S. A. Jamison and A. V. Nurmikko. *"Generation of picosecond pulses of variable duration at 10.6 μm"*. In: Applied Physics Letters 33.7 (1978), pp. 598–600.

[168] V. V. Apollonov, P. B. Corkum, and R. S. Taylor. *"Selection of high-power nanosecond pulses from large-aperture CO_2 oscillators"*. In: Applied Physics Letters 35.2 (1979), pp. 147–149.

[169] R. E. M. de Bekker, L. M. Claessen, and P. Wyder. *"Generation of Very Short Far-Infrared Pulses by Cavity Dumping a Molecular Gas Laser"*. In: Journal of Applied Physics 68.7 (1990), pp. 3729–3731.

[170] S. Marchetti, M. Martinelli, R. Simili, M. Giorgi, and R. Fantoni. *"Controlled Dumping of Pulses of Laser Radiation Ranging from MIR to the MM by Means of Optical Semiconductor Switching"*. In: Applied Physics B 72.8 (2001), pp. 927–930.

[171] C. Rolland and P. B. Corkum. *"Generation of 130-Fsec Midinfrared Pulses"*. In: JOSA B 3.12 (1986), pp. 1625–1629.

[172] A. Y. Elezzabi, J. Meyer, M. K. Hughes, and S. R. Johnson. *"Generation of 1-ps infrared pulses at 10.6 μm by use of low-temperature-grown GaAs as an optical semiconductor switch"*. In: Optics Letters 19.12 (1994), pp. 898–900.

[173] A. Y. Elezzabi. *"Ultrafast Switching of CO_2 Laser Pulses by Optically-Induced Plasma Reflection in Semiconductors"*. 1995.

[174] T. Vogel, G. Dodel, E. Holzhauer, H. Salzmann, and A. Theurer. *"High-Speed Switching of Far-Infrared Radiation by Photoionization in a Semiconductor"*. In: Applied Optics 31.3 (1992), pp. 329–337.

[175] A. J. Alcock and P. B. Corkum. *"Ultra-Fast Switching of Infrared Radiation by Laser-Produced Carriers in Semiconductors"*. In: Canadian Journal of Physics 57.9 (1979), pp. 1280–1290.

[176] P. T. Landsberg. *Recombination in Semiconductors*. Cambridge ; New York: Cambridge University Press, 1992.

[177] J. I. Pankove. *Optical Processes in Semiconductors*. 2 ed. Mineola NY: Dover Publications Inc., 2003.

[178] C. A. Hoffman, K. Jarašiūnas, H. J. Gerritsen, and A. V. Nurmikko. *"Measurement of Surface Recombination Velocity in Semiconductors by Diffraction from Picosecond Transient Free-Carrier Gratings"*. In: Applied Physics Letters 33.6 (1978), pp. 536–539.

[179] D. Marvin, S. Beck, J. Wessel, and J. Rollins. *"Picosecond Carrier Dynamics near the Gallium Arsenide Surface"*. In: IEEE Journal of Quantum Electronics 25.5 (1989), pp. 1064–1071.

[180] A. J. Alcock, P. B. Corkum, D. J. Bradley, G. Porter, and M. H. Key. *"Ultra-short pulse generation with CO_2 lasers"*. In: Philosophical Transactions of the Royal Society of London. Series A, Mathematical and Physical Sciences 298.1439 (1980), pp. 365–376.

[181] B. Mayer, C. Schmidt, J. Bühler, D. V. Seletskiy, D. Brida, A. Pashkin, and A. Leitenstorfer. *"Sub-Cycle Slicing of Phase-Locked and Intense Mid-Infrared Transients"*. In: New Journal of Physics 16.6 (2014), p. 063033.

[182] W. B. Zhao, X. D. Zhang, Z. Y. Ye, J. L. Zhang, C. Y. Li, D. L. Yin, Z. N. Gu, X. H. Zhou, and Z. X. Jin. *"Synthesis of K_3C_{60} single crystal thin films with high critical currents"*. In: Solid State Communications 85.11 (1993), pp. 945–947.

[183] G. P. Kochanski, A. F. Hebard, R. C. Haddon, and A. T. Fiory. *"Electrical Resistivity and Stoichiometry of K_xC_{60} Films"*. In: Science 255.5041 (1992), pp. 184–186.

[184] M. Babadi, M. Knap, I. Martin, G. Refael, and E. Demler. *"Theory of Parametrically Amplified Electron-Phonon Superconductivity"*. In: Physical Review B 96.1 (2017), p. 014512.

[185] M. Knap, M. Babadi, G. Refael, I. Martin, and E. Demler. *"Dynamical Cooper Pairing in Nonequilibrium Electron-Phonon Systems"*. In: Physical Review B 94.21 (2016), p. 214504.

[186] J. R. Coulthard, S. R. Clark, S. Al-Assam, A. Cavalleri, and D. Jaksch. *"Enhancement of Superexchange Pairing in the Periodically Driven Hubbard Model"*. In: Physical Review B 96.8 (2017), p. 085104.

[187] D. M. Kennes, E. Y. Wilner, D. R. Reichman, and A. J. Millis. *"Transient Superconductivity from Electronic Squeezing of Optically Pumped Phonons"*. In: Nature Physics 13.5 (2017), pp. 479–483.

[188] G. Mazza and A. Georges. *"Nonequilibrium Superconductivity in Driven Alkali-Doped Fullerides"*. In: Physical Review B 96.6 (2017), p. 064515.

[189] M. Fabrizio. *"Selective Transient Cooling by Impulse Perturbations in a Simple Toy Model"*. In: Physical Review Letters 120.22 (2018), p. 220601.

[190] A. Nava, C. Giannetti, A. Georges, E. Tosatti, and M. Fabrizio. *"Cooling quasiparticles in A_3C_{60} fullerides by excitonic mid-infrared absorption"*. In: Nature Physics 14.2 (2018), pp. 154–159.

[191] Y. Iwasa and T. Kaneyasu. *"Optical study of electronic structures and phonons in alkali-metal-doped* C_{60}*"*. In: Physical Review B 51.6 (1995), pp. 3678–3685.

[192] A. B. Kuzmenko, L. Benfatto, E. Cappelluti, I. Crassee, D. van der Marel, P. Blake, K. S. Novoselov, and A. K. Geim. *"Gate Tunable Infrared Phonon Anomalies in Bilayer Graphene"*. In: Physical Review Letters 103.11 (2009), p. 116804.

[193] S. B. Fleischer, B. Pevzner, D. J. Dougherty, H. J. Zeiger, G. Dresselhaus, M. S. Dresselhaus, E. P. Ippen, and A. F. Hebard. *"Coherent phonons in alkali metal-doped C_{60}"*. In: Applied Physics Letters 71.19 (1997), pp. 2734–2736.

[194] A. Ceulemans and L. F. Chibotaru. *"Icosahedral $T_{1u} + T_{1g}$ Jahn-Teller problem"*. In: Physical Review B 53.5 (1996), pp. 2460–2462.

[195] R. Rai. *"$(T_{1u}+T_{1g}) \otimes (h_g+_{1u})$ vibronic interaction and superconductivity in C_{60}^{n-} fullerides"*. In: Zeitschrift für Physik B Condensed Matter 99.3 (1995), pp. 327–332.

[196] M. J. Rice and H.-Y. Choi. *"Charged-phonon absorption in doped C_{60}"*. In: Physical Review B 45.17 (1992), pp. 10173–10176.

[197] Y. J. Uemura. *"Dynamic Superconductivity Responses in Photoexcited Optical Conductivity and Nernst Effect"*. In: Physical Review Materials 3.10 (2019), p. 104801.

[198] G. Lucas and M. J. Stephen. *"Relaxation of the Superconducting Order Parameter"*. In: Physical Review 154.2 (1967), pp. 349–353.

[199] P. W. Anderson and A. H. Dayem. *"Radio-Frequency Effects in Superconducting Thin Film Bridges"*. In: Physical Review Letters 13.6 (1964), pp. 195–197.

[200] A. F. G. Wyatt, V. M. Dmitriev, W. S. Moore, and F. W. Sheard. *"Microwave-Enhanced Critical Supercurrents in Constricted Tin Films"*. In: Physical Review Letters 16.25 (1966), pp. 1166–1169.

[201] G. Eliashberg. *"Film Superconductivity Stimulated by a High-Frequency Field"*. In: JETP Letters 11.114 (1970).

[202] G. Nieva, E. Osquiguil, J. Guimpel, M. Maenhoudt, B. Wuyts, Y. Bruynseraede, M. B. Maple, and I. K. Schuller. *"Photoinduced Enhancement of Superconductivity"*. In: Applied Physics Letters 60.17 (1992), pp. 2159–2161.

[203] G. Yu, C. H. Lee, A. J. Heeger, N. Herron, E. M. McCarron, L. Cong, G. C. Spalding, C. A. Nordman, and A. M. Goldman. *"Phase separation of photogenerated carriers and photoinduced superconductivity in high-T_c materials"*. In: Physical Review B 45.9 (1992), pp. 4964–4977.

[204] G. Yu, A. J. Heeger, G. Stucky, N. Herron, and E. M. McCarron. *"Transient photoinduced conductivity in semiconducting single crystals of*

$YBa_2Cu_3O_{6.3}$: Search for photoinduced metallic state and for photoinduced superconductivity". In: Solid State Communications 72.4 (1989), pp. 345–349.

[205] S. D. Brorson, J. G. Fujimoto, and E. P. Ippen. *"Femtosecond Electronic Heat-Transport Dynamics in Thin Gold Films"*. In: Physical Review Letters 59.17 (1987), pp. 1962–1965.

[206] S. H. Strogatz. *Sync: The Emerging Science of Spontaneous Order*. 1st ed. New York: Hyperion, 2003.

[207] F. Schlawin, A. Cavalleri, and D. Jaksch. *"Cavity-Mediated Electron-Photon Superconductivity"*. In: Physical Review Letters 122.13 (2019), p. 133602.

[208] A. Thomas, E. Devaux, K. Nagarajan, T. Chervy, M. Seidel, D. Hagenmüller, S. Schütz, J. Schachenmayer, C. Genet, G. Pupillo, and T. W. Ebbesen. *"Exploring Superconductivity under Strong Coupling with the Vacuum Electromagnetic Field"*. In: (2019). arXiv: 1911.01459.

[209] H. Gao, F. Schlawin, A. Cavalleri, and D. Jaksch. *"Photo-Induced Electron Pairing in a Driven Cavity"*. In: (2020). arXiv: 2003.05319.

[210] J. T. Kindt and C. A. Schmuttenmaer. *"Theory for Determination of the Low-Frequency Time-Dependent Response Function in Liquids Using Time-Resolved Terahertz Pulse Spectroscopy"*. In: The Journal of Chemical Physics 110.17 (1999), pp. 8589–8596.

[211] C. A. Schmuttenmaer. *"Exploring Dynamics in the Far-Infrared with Terahertz Spectroscopy"*. In: Chemical Reviews 104.4 (2004), pp. 1759–1780.

[212] *Terahertz Spectroscopy: Principles and Applications*. Optical Science and Engineering 131. Boca Raton: CRC Press, 2008.

[213] C. M. O'Sullivan and J. A. Murphy. *Field Guide to Terahertz Sources, Detectors, and Optics*. SPIE, 2012.

[214] F. D'Angelo, H. Němec, S. H. Parekh, P. Kužel, M. Bonn, and D. Turchinovich. *"Self-Referenced Ultra-Broadband Transient Terahertz Spectroscopy Using Air-Photonics"*. In: Optics Express 24.9 (2016), pp. 10157–10171.

[215] M. Born, E. Wolf, A. B. Bhatia, P. C. Clemmow, D. Gabor, A. R. Stokes, A. M. Taylor, P. A. Wayman, and W. L. Wilcock.

Principles of Optics: Electromagnetic Theory of Propagation, Interference and Diffraction of Light. 7th ed. Cambridge University Press, 1999.

[216] D. Nicoletti, E. Casandruc, Y. Laplace, V. Khanna, C. R. Hunt, S. Kaiser, S. S. Dhesi, G. D. Gu, J. P. Hill, and A. Cavalleri. *"Optically induced superconductivity in striped* $La_{2-x}Ba_xCuO_4$ *by polarization-selective excitation in the near infrared"*. In: Physical Review B 90.10 (2014), p. 100503.

[217] D. M. Pozar. *Microwave Engineering*. 4th ed. Hoboken, NJ: Wiley, 2012.

[218] S. Banerjee, T. V. Ramakrishnan, and C. Dasgupta. *"Phenomenological Ginzburg-Landau-like Theory for Superconductivity in the Cuprates"*. In: Physical Review B 83.2 (2011), p. 024510.

[219] K. Sarkar, S. Banerjee, S. Mukerjee, and T. V. Ramakrishnan. *"The Correlation between the Nernst Effect and Fluctuation Diamagnetism in Strongly Fluctuating Superconductors"*. In: New Journal of Physics 19.7 (2017), p. 073009.

[220] K. Sarkar, S. Banerjee, S. Mukerjee, and T. V. Ramakrishnan. *"Doping Dependence of Fluctuation Diamagnetism in High Tc Superconductors"*. In: Annals of Physics 365 (2016), pp. 7–23.

[221] M. Le Bellac, G. G. Batrouni, and F. Mortessagne. *Equilibrium and Non-Equilibrium Statistical Thermodynamics*. Cambridge: Cambridge Univ. Press, 2009.

[222] R. D. Averitt, G. Rodriguez, A. I. Lobad, J. L. W. Siders, S. A. Trugman, and A. J. Taylor. *"Nonequilibrium superconductivity and quasiparticle dynamics in* $YBa_2Cu_3O_{7-\delta}$*"*. In: Physical Review B 63.14 (2001), p. 140502.

[223] F. Calegari, D. Ayuso, A. Trabattoni, L. Belshaw, S. D. Camillis, S. Anumula, F. Frassetto, L. Poletto, A. Palacios, P. Decleva, J. B. Greenwood, F. Martín, and M. Nisoli. *"Ultrafast Electron Dynamics in Phenylalanine Initiated by Attosecond Pulses"*. In: Science 346.6207 (2014), pp. 336–339.

[224] A. L. Cavalieri, N. Müller, T. Uphues, V. S. Yakovlev, A. Baltuška, B. Horvath, B. Schmidt, L. Blümel, R. Holzwarth, S. Hendel, M. Drescher, U. Kleineberg, P. M. Echenique, R. Kienberger, F. Krausz, and U. Heinzmann. *"Attosecond Spectroscopy in Condensed Matter"*. In: Nature 449.7165 (7165 2007), pp. 1029–1032.

[225] *Electronic Properties of High-Tc Superconductors: The Normal and the Superconducting State of High-Tc Materials*. Red. by M. Cardona, P. Fulde, K. von Klitzing, H.-J. Queisser, and H. K. V. Lotsch. Vol. 113. Springer Series in Solid-State Sciences. Berlin, Heidelberg: Springer Berlin Heidelberg, 1993.

[226] A. Pashkin, M. Porer, M. Beyer, K. W. Kim, A. Dubroka, C. Bernhard, X. Yao, Y. Dagan, R. Hackl, A. Erb, J. Demsar, R. Huber, and A. Leitenstorfer. *"Femtosecond Response of Quasiparticles and Phonons in Superconducting $YBa_2Cu_3O_{7-\delta}$ Studied by Wideband Terahertz Spectroscopy"*. In: Physical Review Letters 105.6 (2010), p. 067001.

[227] J. van den Brink, O. Gunnarsson, and V. Eyert. *"Optical conductivity in A_3C_{60} (A = K, Rb)"*. In: Physical Review B 57.4 (1998), pp. 2163–2167.